

**ՀՀ ԳԱԱ Վ. ՀԱՄԲԱՐՁՈՒՄՅԱՆԻ ԱՆՎԱՆ ԲՅՈՒՐԱԿԱՆԻ  
ԱՍՏՂԱԴԻՏԱՐԱՆ**

**ԻՍՐԱՅԵԼՅԱՆ ԴԱՎԻԹ ՍԱՄՎԵԼԻ  
ԲԼԱՋԱՐՆԵՐԻ ԳԵՐՄԱՆՈՒՇԱԿԱԳՈՒՅՆ և ՌԵՆՏԳԵՆՅԱՆ  
ՀԱՏԿՈՒԹՅՈՒՆՆԵՐԻ ՈՒՍՈՒՄՆԱՍԻՐՈՒԹՅՈՒՆ**

**ԱՏԵՆԱԽՈՍՈՒԹՅՈՒՆ**

**Ա.03.02 - «Աստղաֆիզիկա, ռադիոաստղագիտություն»  
մասնագիտությամբ ֆիզիկամաթեմատիկական  
գիտությունների թեկնածուի գիտական աստիճանի համար**

**Գիտական ղեկավար՝  
Ֆ.մ.գ.թ. Նարեկ Սահակյան**

**ԵՐԵՎԱՆ-2022**

**NAS RA BYURAKAN ASTROPHYSICAL OBSERVATORY AFTER V.  
AMBARTSUMIAN**

**DAVIT ISRAYELIAN**

**INVESTIGATION OF UV AND X-RAY PROPERTIES OF BLAZARS**

**DOCTORAL THESIS**

**A thesis submitted in fulfillment of the requirements for the  
degree of Doctor of philosophy in specialization 01.03.02 –  
“Astrophysics and Radioastronomy”**

**Supervisor:**

**Dr. Narek Sahakyan**

**YEREVAN–2022**

## Table of Contents

INTRODUCTION .....	5
1 MULTIWAVELENGTH OBSERVATIONS OF BLAZARS AND ORIGIN OF THE EMISSION .....	11
1.1 SYNCHROTRON RADIATION .....	11
1.2 INVERSE COMPTON SCATTERING .....	13
1.3 MULTIWAVELENGTH OBSERVATIONS OF BLAZARS .....	15
2 X-RAY SPECTRA, LIGHT CURVES AND SEDS OF BLAZARS FREQUENTLY OBSERVED BY SWIFT .....	28
2.1 INTRODUCTION .....	28
2.2 BLAZARS FREQUENTLY OBSERVED BY SWIFT-XRT .....	28
2.3 DATA PROCESSING .....	29
2.4 RESULTS .....	36
2.5 DISCUSSION .....	44
2.6 CONCLUSION .....	49
3 MULTIWAVELENGTH MONITORING OF BLAZARS PKS 2155-304 AND S5 0716+71 .....	50
3.1 INTRODUCTION .....	50
3.2 MONITORING OF THE SOURCES IN OPTICAL/UV BANDS .....	51
3.3 X-RAY OBSERVATIONS OF PKS 2155-304 AND S5 0716+71 .....	54
3.4 GAMMA-RAY OBSERVATIONS AND DATA ANALYSIS .....	55
3.5 RESULTS AND INTERPRETATION .....	57
3.6 SUMMARY .....	65
4 LONG-TERM MULTIWAVELENGTH STUDY OF BLAZAR CTA 102 .....	66
4.1 INTRODUCTION .....	66
4.2 MULTIWAVELENGTH OBSERVATIONS OF CTA 102 .....	67
4.3 MULTIWAVELENGTH VARIABILITY .....	70
4.4 BROADBAND SED MODELING .....	73
4.5 RESULTS AND DISCUSSION .....	77
4.6 CONCLUSION .....	88
5 A MULTIWAVELENGTH STUDY OF DISTANT BLAZAR PKS 0537-286 .....	90

5.1 INTRODUCTION .....	90
5.2 MULTIWAVELENGTH OBSERVATIONS AND DATA ANALYSIS.....	91
5.3 BROADBAND SEDs .....	96
5.4 DISCUSSION AND CONCLUSION .....	99
CONCLUSION .....	101
REFERENCES.....	102

# INTRODUCTION

The observations early in the 20th century already revealed that there are emission lines in the nuclei of some galaxies. Then, due to the progress in radio observations, the first quasar was discovered. It initiated intense effort in studying these new objects, collectively referred to as Active Galactic Nuclei (AGNs). The AGNs have stronger emission at the compact core which has a much higher luminosity than the rest of the galaxy. It is believed that the activity from the core is due to accretion onto the supermassive black hole, though other scenarios have also been proposed. The main characteristic properties of AGNs include: very high bolometric luminosity (up to  $L_{bol} \approx 10^{48} \text{ erg s}^{-1}$ ), making them among the most powerful extragalactic sources, very compact emitting region inferred from fast variability,

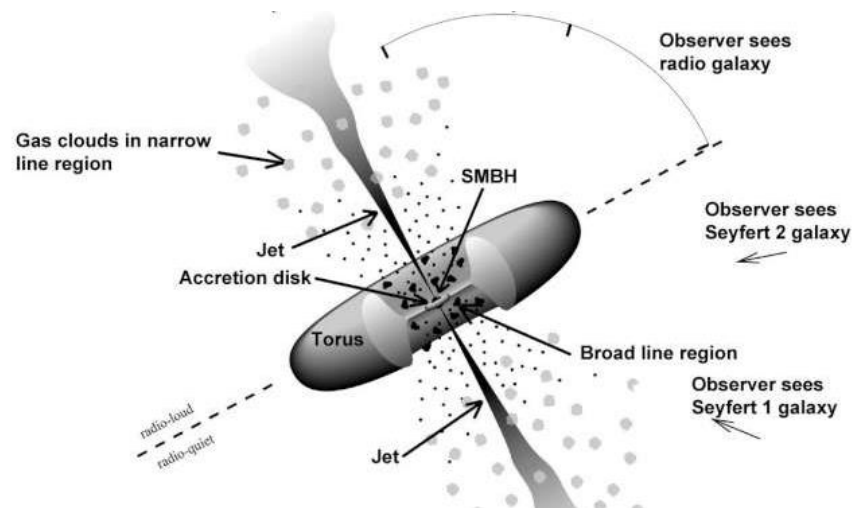


Figure 1.1: Current unification sketch of AGNs [174]

and that their emission covers the whole electromagnetic spectrum.

A wide range of objects are grouped under the name of AGNs which show some common properties (e.g., high emission power) but usually AGNs show different properties. The currently accepted interpretation is that different properties of AGNs depend on their orientation toward the observer's frame. A sketch of the current interpretation of different types of AGNs is shown in Figure 1.1 [1]. Around the central supermassive black hole, an accretion disk is formed which emits in the optical/UV and X-ray bands. Close to the central black hole broad emission lines are observed which can be due to photoionization of the gas surrounding the black hole. Also, the gravitational potential of the black hole drives the gas

to form a toroidal structure (torus) towards the accretion plane. Roughly 10% of radio loud AGNs, i.e., the radio (5 GHz) to optical (B-band) flux ratio is  $> 10$ , show a highly collimated linear structure of plasma, – a jet that continuously extracts energy from the central source. This jet happens to play a crucial role in understanding the physical processes in AGNs and their classifications. First, these jets can extend to several hundreds of kiloparsecs into the space often remaining highly collimated, and they are strong sources of radiation in all the accessible bands of the electromagnetic spectrum. Second, depending on the orientation of the jet, the AGN can have different appearances. According to the unification scheme, an AGN is called a blazar when the jet is closely aligned with the line of sight of the observer. Or when the jet's inclination angle is larger, the AGN appears as a radio galaxy.

Blazars are the extreme sub-class of AGNs characterized by high radio and optical polarization, apparent superluminal motion along with high-amplitude variability in all accessible bands of the electromagnetic spectrum. Usually, this variability is unpredictable; periodic variability is observed only from a few objects (e.g., [2, 3]). Blazars are usually believed to be persistent sources, however recently a blazar showing a transient behaviour was observed. Namely, 4FGL J1544.3-0649 was never detected in the X-ray and  $\gamma$ -ray bands until May 2017 when it rose above the detectability level and for a few months became one of the brightest X-ray blazars [4]. Blazar emission is dominated by non-thermal emission from the jet which is significantly Doppler amplified since the jet with superluminal motion is viewed at small angles. Because of this, blazars even at higher redshifts are observed [5].

The emission from blazars is observed in a wide frequency range, from radio to high energy (HE;  $> 100$  MeV) and very high energy (VHE;  $> 100$  GeV)  $\gamma$ -ray bands displaying a double hump structure in their broadband spectral energy distribution (SED). As an example, the multi wavelength SED of 3C 273 is shown in Figure 1.2, calculated using VOU blazar tool [6]. The first component (low-energy) usually peaks between far infrared and X-rays while the second component (HE) is observed between X-rays and High Energy (HE;  $> 100$  MeV)/ very high energy (VHE)  $\gamma$ -rays. The low-energy component is explained by the synchrotron emission of jet-accelerated electrons under the magnetic field while the origin of the HE component is discussed within leptonic and hadronic models, depending on the type of

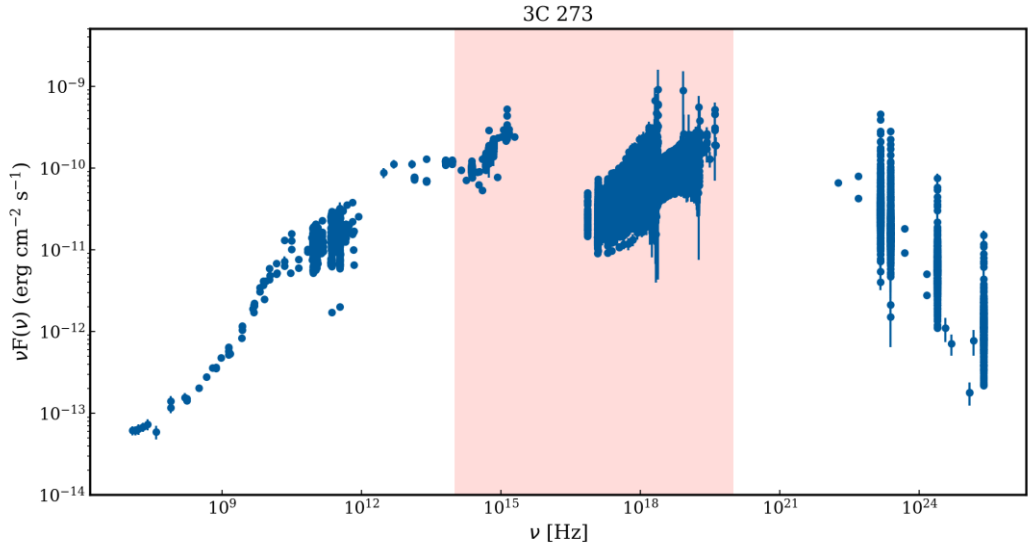


Figure 1.2: Broadband SED of 3C 273 accumulated in different periods.

emission initiating particles,  $e^-e^+$  pairs or hadrons. According to the widely discussed leptonic scenario, the HE component is due to inverse Compton upscattering of photons by energetic electrons. Most common scenarios used in the literature are synchrotron self-Compton (SSC) model and the external Compton (EIC) model. According to the first scenario, the internal synchrotron photons are up-scattered to higher energies [7, 8, 9] whereas the latter model assumes the photons are produced external to the jet [10, 11, 12]. In alternative hadronic or lepto-hadronic scenarios, the protons co-accelerated with the electrons make a non-negligible contribution to the HE component. This contribution can be either directly from proton synchrotron radiation [13] or from secondaries produced in the proton-photon interactions or photo-pair productions [13, 14, 15, 16, 17, 18, 19]. Lately, the hadronic models (especially lepto-hadronic [19]) have become more attractive after the detection of VHE neutrinos spatially coinciding with the direction of known blazars [20, 21, 22]. The initial association between TXS 0506+056 and the IceCube-170922A event provided the first multimessenger picture of the blazar and opened a wider perspective for theoretical studies [19, 22, 23, 24, 25, 26, 27, 28, 29, 30]. The assumption that blazars are neutrino sources was further strengthened by the observation of multiple neutrino events from the direction of PKS 0735+178 when the source was undergoing a major flaring activity in the optical/UV, X-ray and  $\gamma$ -ray bands [31].

Commonly, the blazars are grouped based on their optical spectral properties. Namely, Flat Spectrum Radio Quasars (FSRQs) which show strong optical lines and BL Lacertae type

objects (BL Lacs) which have very faint optical emission lines. Blazars are further classified based on the observed SEDs. Namely, based on the frequency where the synchrotron component peaks ( $\nu_p$ ), blazars are separated into low, intermediate and high-energy peaked sources [32, 33]; low synchrotron peaked sources (LSPs or LBLs) when  $\nu_p < 10^{14}$  Hz, intermediate synchrotron peaked sources (ISPs or IBLs) when  $10^{14} < \nu_p < 10^{15}$  Hz and high synchrotron peaked sources (HSPs or HBLs) when  $\nu_p > 10^{15}$  Hz. However, recently [34] showed that there are strong similarities between the properties of IBLs and HBLs and they show large differences from LBLs, so the classification can be refined into LBLs and intermediate-high-energy-peaked objects (IH- BLs) when  $\nu_p$  is below or above  $10^{13.5}$  Hz.

The fact that blazars can be observed in almost all energy bands of the electromagnetic spectrum, makes them interesting targets for multi wavelength studies. The single-band observations of blazars give a specific local view of the ongoing complex emission processes, and in order to draw a general picture of the nature of blazar emission, it is necessary to combine the results from the observations in different bands. The combined data from radio to VHE  $\gamma$ -ray bands provide a unique chance to understand their physics. In the recent years the accumulation of a significant amount of multiwavelength data and its continuous increase create conditions necessary for further exploration of the physics at work in blazar jets. However, new methods should be adopted to deal with the available data and its interpretation, i.e., more efficient methods should be used to analyse the data as well as more detailed models should be used for theoretical modelling. Frequent observations of blazars in different bands allow to investigate their multiwavelength variability which covers a wide range of timescales; it is also necessary to understand the formation of emission components. In this context, the monitoring of blazars in the optical/UV and X-ray bands (red shaded area in Figure 1.2) as well as investigation of the variability in those bands is of particular importance. These bands are defining synchrotron and inverse Compton components in the SEDs (depending on the type of the blazars) and they can put a constraint on both emission components. The data available from Swift UVOT/XRT observations combined with that from  $\gamma$ -ray data from Fermi-LAT allows to perform extensive investigations in different bands.

In this thesis, the optical/UV and X-ray properties of different blazars is discussed by analysing a large amount of data observed by Swift and Fermi-LAT. The thesis consists of Introduction, four chapters, conclusion and references.

In Introduction the scientific literature related to the topic is reviewed, the novelty of the topic is discussed as well as the aims of the work, the scientific novelty and the main results obtained in each chapter is presented.

In Chapter 1 the main processes of interaction (synchrotron radiation and inverse Compton scattering) of accelerated electrons inside the jet are briefly discussed. Also, the main properties of Fermi Large Area Telescope (Fermi-LAT) and The Neil Gehrels Swift Observatory (Swift) is presented together with main steps to analyse the data obtained by these telescopes.

In Chapter 2 presented an accurate spectral and photometric analysis of the Swift-XRT data of all blazars observed by Swift at least 50 times between December 2004 and the end of 2020, which have been carried out by the use of `swift_xrtproc` tool. As well as is presented a database of X-ray spectra, best-fit parameter values, count-rates and flux estimations in several energy bands of over 31,000 X-ray observations and single snapshots of 65 blazars. The results of the X-ray analysis have been combined with other multi-frequency archival data to assemble the broad-band Spectral Energy Distributions (SEDs) and the long-term lightcurves of all sources in the sample.

In Chapter 3 the emission of PKS 2155-304 ( $z = 0.116$ ) and S5 0716+71 ( $z = 0.31$ ) bright blazars in the optical/UV, X-ray and  $\gamma$ -ray bands is investigated by analysing data from Fermi-LAT, Swift XRT and Swift UVOT telescopes. With the help of Python programming language, have been created multiwavelength light curves of both sources, and using statistical methods were checked the data in different bands for the presence of the correlation. The observed broadband spectral energy distribution of both sources as well as the observed variability and correlations can be accounted for within one-zone synchrotron/synchrotron-self-Compton models.

In Chapter 4 presented long-term multiwavelength observations of blazar CTA 102 ( $z = 1.037$ ). Detailed temporal and spectral analyses of  $\gamma$ -ray, X-ray and UV/optical data observed

by Fermi-LAT, Swift XRT, NuSTAR and Swift-UVOT over a period of 14 years, between August 2008 and March 2022, was performed. Variability and an intraband correlations in the all considered bands were studied. Using the Bayesian Blocks algorithm, we split the adaptively binned  $\gamma$ -ray light curve into groups of quiescent and flaring episodes and for each period built corresponding multiwavelength spectral energy distributions (SEDs), using the available data. Presented modelling results of 117 high-quality (quasi) contemporaneous SEDs using a one-zone leptonic synchrotron and inverse Compton emission scenario assuming the emitting region is within the broad-line-region and considering internal and external seed photons for the inverse Compton up-scattering. Also, derived some constraints on the properties of the jet and emitting particles, perform systematic scan of the model parameters space, compare and contrast them in various states of the source emission.

In chapter 5 has been investigated one of the most distant blazar's PKS 0537-286 ( $z = 3.1$ ) broadband emission using data spanning more than ten years from the Fermi Large Area Telescope together with Swift UVOT/XRT archival data taken between 2005 and 2017. Were derived and modelled spectral energy distributions (SED) within one-zone leptonic models assuming the emission region is within the broad-line region. The observed X-ray and  $\gamma$ -ray data are modelled as inverse Compton scattering of (i) only synchrotron photons and (ii) synchrotron and external photons on the electron population that produces the radio-to-optical emission.

# 1 MULTIWAVELENGTH OBSERVATIONS OF BLAZARS AND ORIGIN OF THE EMISSION

In this subsection the non-thermal emission processes which are taking place in blazar jets will be presented and discussed. Namely, the synchrotron radiation and inverse Compton (IC) scattering of electrons will be discussed. These are two main channels by which the accelerated electrons loss energy during the propagation in the jet, so they are important for understanding the origin of emission from the jets. Also, these two radiation processes will be frequently used in the thesis, so basic principles of these interactions are presented and discussed.

## 1.1 SYNCHROTRON RADIATION

As mentioned in the previous section, the SED of blazars has two broadband two. The first peak, low energy component, usually is described as synchrotron radiation of relativistic electrons. Under the magnetic field the relativistic electron starting to spiral around magnetic field and emit photons (Figure 1.1).

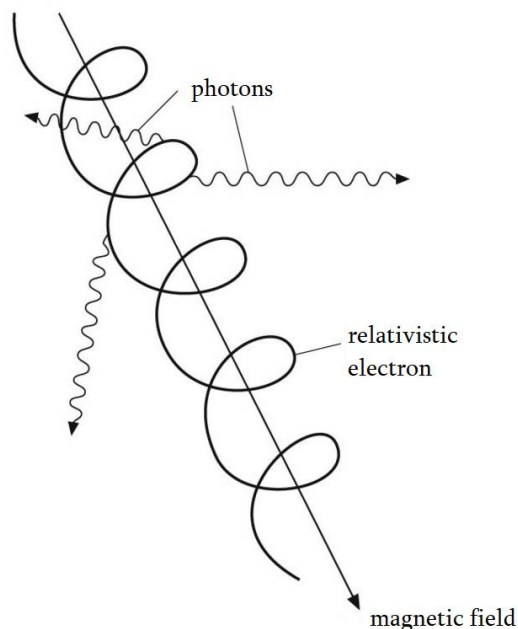


Figure 1.1: A sketch of synchrotron radiation of electrons [35].

The electron will lose some amount of its energy by emitting photons via synchrotron emission. The energy loss can be calculated by the following equation:

$$\frac{dE_e}{dt} = \frac{4}{3} c \sigma_T \gamma^2 U_B \quad (2.1),$$

where  $U_b = \frac{B^2}{8\pi}$  is the magnetic field energy density,  $\sigma_T = \frac{4\pi r_0^2}{3}$  is the Thomson cross-section,  $r_0 = \frac{e^2}{mc^2}$  is the radius of electron,  $e$  is the electron charge,  $m$  is the electron rest mass,  $c$  is the speed of light,  $B$  is the magnetic field. In the Eq. 2.1, for the electron population pitch angles can be averaged assuming that electrons have an isotropic distribution:  $\overline{\sin^2\theta} = \frac{2}{3}$ , where  $\theta$  is the inclination angle of the velocity vector and the magnetic field lines (the pitch angle).

Equation 2.1 shows electron energy loss rate when it emits via synchrotron emission, and the energy will be transferred to produced photons. For a single electron emitting via synchrotron radiation the differential energy spectrum can be computed from

$$\frac{dN_\gamma}{dE_\gamma dt} = \frac{\sqrt{3}}{2\pi} \frac{e^3 B}{mc^2 \hbar E_\gamma} F\left(\frac{E_\gamma}{E_c}\right) \quad (2.2),$$

where,  $F(x)$  is computed by:

$$F(x) = \int_x^{inf} K_{5/3}(x') dx' \quad (2.3),$$

where  $K_{5/3}$  is the 5/3 order Bessel function.

Also, the emitted photons characteristic frequency  $\nu_c$  (the frequency where the emission has the maximum power) can be computed by

$$\nu_c = \frac{3eB}{4\pi mc} \left(\frac{E_e}{mc^2}\right)^2 \quad (2.4).$$

Above the emission from a single electron is discussed, and for the electron population  $N(E_e)$ , the differential synchrotron emission spectrum should be calculated by integrating the distribution of electrons with the single electron spectrum over electron energy:

$$\left(\frac{dN_\gamma}{dE_\gamma dt}\right)_N = \int_{E_{min}}^{E_{max}} \left(\frac{dN_\gamma}{dE_\gamma dt}\right)_1 N(E_e) dE_e \quad (2.5).$$

In Figure 1.2, an example of electron synchrotron emission spectrum is shown, computed assuming  $E_e^{-\alpha} \text{Exp}[-(E_e/E_{cutoff})]$  power law with exponential cut-off energy distributions for the electrons and adopting the parameters  $E_{min} = 100$ ,  $E_{max} = 10^8$ ,  $B = 0.003G$ ,  $\alpha = 2$ ,  $E_{cut} = 5000$  is shown in Figure 1.3.

## 1.2 INVERSE COMPTON SCATTERING

In the Inverse Compton (IC) scattering, the high energy electrons interact with the low energy photons and up-scatters them to high energies (Figure 1.2). Different low energy photons can server as a target for IC scattering. In the case of blazars, the following low energy photons can up-scatter to higher energies:

- Synchrotron photons (SSC)
- Accretion disk photons
- Broad Line Region (BLR) photons
- Torus photons

Depending on the initial energies of interacting electrons and photons the IC scattering can be in two different regimes, namely in Thomson or in Klein-Nishina regimes. If we denote with  $\varepsilon$  photon energy before the interaction, and with  $\varepsilon_1$  energy after the interaction, for a single electron the differential spectrum can be computed by [36]

$$\frac{dN}{dt d\varepsilon_1} = \frac{2\pi r_0^2 mc}{E_e^2} \frac{n(\varepsilon) d\varepsilon}{\varepsilon} F_c(q, \Gamma_e) \quad (2.6),$$

where

$$F_c(q, \Gamma_e) = \left[ 2q \ln q + (1 + 2q)(1 - q) + \frac{1}{2} \frac{(\Gamma_e q)^2}{1 + \Gamma_e q} (1 - q) \right]$$

$$E_1 = \varepsilon_1 (\gamma m_e c^2), \quad q = \frac{E_1}{\Gamma_e (1 - E_1)}, \quad \Gamma_e = \frac{4\gamma\varepsilon}{m_e c^2},$$

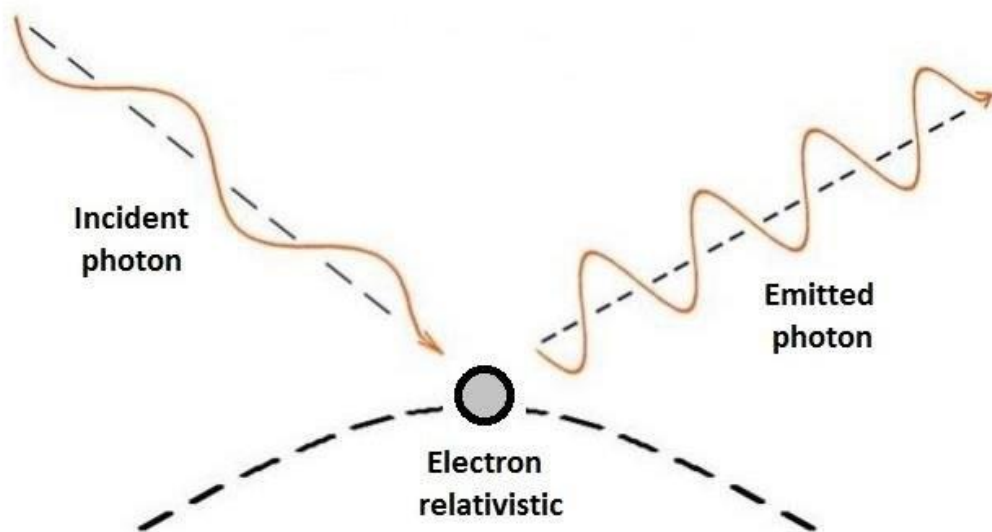


Figure 1.2: Inverse Compton scattering [37]

is the cross-section of the process and  $n(\varepsilon)$  is the target photon field density and  $E_e$  is the energy of the interacting electron. As in the case of synchrotron radiation, when the IC scattering is computed for an electron population, the emission spectrum given by Equation 2.6 should be integrated for the whole electron energy range. For isotropic photon field  $u(\varepsilon) = \varepsilon n(\varepsilon)$  and electrons  $N_e(\gamma)$  the luminosity of IC scattering can be calculated by [38]

$$L_{IC}(\varepsilon_s) = \frac{3}{4} c \sigma_T \varepsilon_s^2 \int_0^{inf} d\varepsilon \frac{u(\varepsilon)}{\varepsilon^2} \int_{\gamma_{min}}^{inf} d\gamma \frac{N_e(E_e)}{E_e^2} F_c(q, \Gamma_e) \quad (2.7),$$

where  $\varepsilon_s$  is the energy of scattered photon.

**SYNCHROTRON SELF-COMPTON SCATTERING:** As a target photon field for the IC scattering can serve the synchrotron photons emitted by the same electrons, which is called Synchrotron self-Compton (SSC) emission. SSC emission spectrum can be computed with the

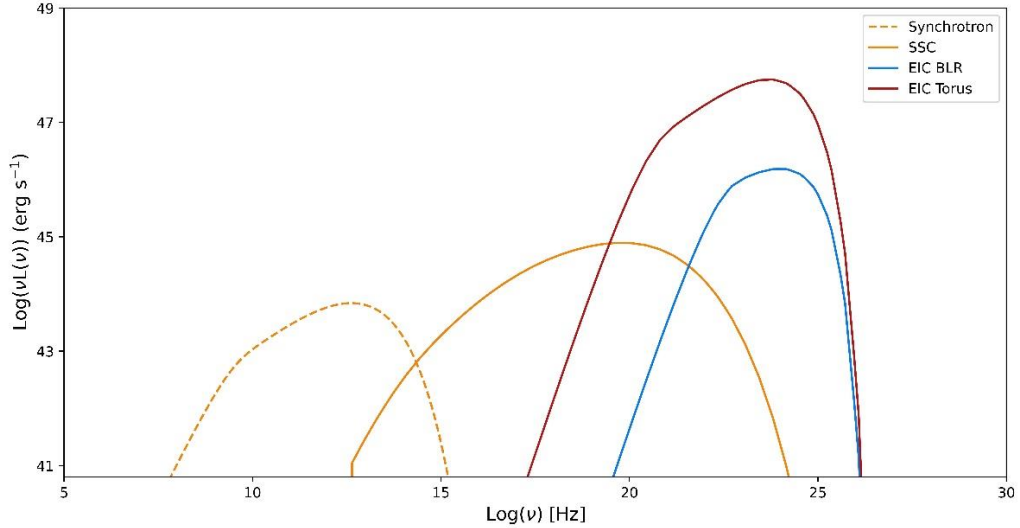


Figure 1.3: Typical SED of a blazar showing synchrotron, SSC and EIC (both for BLR and torus photons) components.

Equation 2.7, assuming that photon and electron distribution are homogeneous and isotropic,

$$u(\varepsilon) = U_{SSC}(\varepsilon) \quad \text{and} \quad \gamma_{min} = \frac{1}{2} \frac{\varepsilon_s(1+z)}{\delta_D} \left( 1 + \sqrt{1 + \frac{1}{\frac{\varepsilon \varepsilon_s(1+z)}{\delta_D}}} \right),$$

and photon energy density can be

$$u_{SSC}(\varepsilon) = \frac{2.24 L_{syn}(\varepsilon)}{4\pi c R_b'^2} \quad (2.8),$$

where  $R_b$  is the radius of the emitting region. An example of SSC spectrum, computed for the same parameters as the synchrotron radiation is shown in Figure 1.3.

**EXTERNAL COMPTON:** The external photons also can serve as target for the IC scattering. For example, as target photons can serve: photons radiated from the accretion disk, the photons reflat from the broad-line region (BLR) at the distance of  $10^{15} - 10^{18}$  cm from the central black hole, or the thermal radiation from the hot dusty torus (very hot with a temperature from several hundred to a few thousands Kelvin toroidal region beyond the BLR emitting) mostly in the infrared range.

The emission from the accretion disk can be computed using the emission from a ring and then integrating it from the inner to the outer radii ( $R_{in} = 3R_s$ ,  $R_{out}$ , where  $R_s$  is the Schwarzschild radius):

$$\nu F_\nu(\nu) = \frac{4\pi h\nu^4}{c^2 d_L^2} \int_{R_{in}}^{R_{out}} \frac{R dR}{\exp\left[\frac{h\nu}{kT(R)}\right] - 1} \quad (2.9),$$

The luminosity for the EIC can be calculated by [38]:

$$L_{ext}(\varepsilon) = \frac{15}{\pi^4} \xi_{ext} L_{disk} \frac{(\varepsilon/kT_{ext})^4}{\text{Exp}[\varepsilon/kT_{ext}] - 1} \quad (2.10),$$

where  $\xi_{ext}$  correspondingly equals  $\xi_{dust} = 0.3$  and  $\xi_{BLR} = 0.6$ , and shows the quantity of the accretion disk reflected emission and  $T_{ext}$  is the temperature.

The energy densities of the external photon fields can be computed as [39, 40]:

$$u_{ext}(\varepsilon, r) = \frac{L_{ext}(\varepsilon)}{4\pi c R_{ext}^2} \frac{1}{1 + (r/R_{ext})^{n_{ext}}} \quad (2.11),$$

where as in previous case “ext” is or dusty torus or BLR, correspondingly  $n_{BLR} = 3$  and  $n_{dust} = 4$ , and  $r$  is the distance of the emission region from the central source, which can be computed with  $R_{BLR} = 10^{17} \left(\frac{L_{disk}}{10^{45}}\right)^{0.5}$  cm and  $R_{dust} = 0.4 \left(\frac{L_{disk}}{10^{45}}\right)^{0.5} (1500K/T_{dust})^{2.6}$  pc [41] correspondingly for the distances of the BLR and Torus from the central source. Example of the spectrum of IC scattering of BLR reflected and torus fields with the parameters  $R = 5 \times 10^{16}$  cm,  $L_{disk} = 10^{43}$  erg s<sup>-1</sup> is shown in Figure 1.3. Again, it is calculated for the electron population having a power law with exponential cut-off distribution, as in case of the synchrotron emission.

### 1.3 MULTIWAVELENGTH OBSERVATIONS OF BLAZARS

In this sub-section the multiwavelength data accusation will be discussed presenting the telescopes, their technical capabilities, working principles, methods of data analysis and the tools used during the analysis.

**SWIFT:** The Neil Gehrels Swift Observatory [42] was launched aboard on Delta II 7320 rocket on November 20, 2004. It is a low orbit Earth telescope, it rotates on orbit of  $585 \times 604$  km altitude, with an inclination of  $20.60^\circ$ . Swift by its kind is a first multi-wavelength observatory, which simultaneously performs observation in different wavebands (namely in optical, ultraviolet (UV), and X-ray bands) and its measurements have significant impact on studying processes taking in different astrophysical objects. Swift has been developed by an international collaboration of Italy, the United Kingdom, and the USA, as a part of NASA's medium explorer program. All the data products after processing are available for the astrophysical community via public archive.

The Swift telescopes main objectives are:

- Perform survey of the sky in the X-ray band
- Determine, study and classify GRBs (Gamma ray bursts)
- Supernova cosmology
- Carry out multi-messenger time domain observations in the sky

Swift carries three instruments, which work together and provide quickly identification and multi wavelength observations of the sources and GRBs.

The three instruments are (Figure 1.4):

- The Burst Alert Telescope (BAT)

The BAT [43] is the largest instrument on the board and it is a wide field coded aperture imaging telescope. It has a high sensitivity, large field of view (BAT's all parameters are listed in the Table 1.1). It performs imaging in the 15-150 keV energy band and provides 1-3 arcminute positions of the sources. The BAT for the detection of a weak burst uses a 2-dimensional coded aperture mask and the SSD's large area. Firstly, the BAT detects some kind of event (e.g., GRB), then it sends an alert to the XRT and the UVOT instruments. Within seconds after alert the spacecraft starts to point to the position computed by the BAT. The aim of the pointing is to obtain the same events' X-ray and ultraviolet/optical positions and spectra.

- The X-ray telescope (XRT)

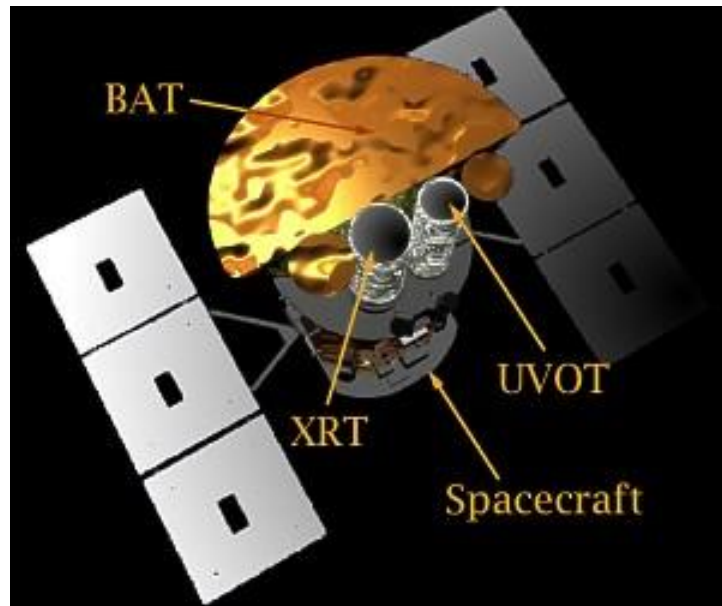


Figure 1.4: The Swift telescope picture<sup>1</sup>.

Table 1.1: The burst alert telescopes' (BAT) parameters.

BAT Parameter	Value
Energy Range	approximately 15-150 keV (imaging)
Energy Resolution	approximately 5 keV at 60 keV
Aperture	Coded mask, random pattern, 50% open
Effective Area	approximately 1400 cm <sup>2</sup> (see caption)
Detection Area	5240 cm <sup>2</sup>
Detector Material	CdZnTe (CZT)
Detector Operation	Photon counting
Field of View	1.4 sr (half-coded)
Detector Elements	256 modules of 128 elements/module
Detector Element Size	4 × 4 × 2 mm
Coded Mask Cell Size	5 × 5 × 1 mm Pb tiles
Telescope PSF	22 arcminutes FWHM
Source Localization	1-3 arcminutes radius
15-150 keV Sensitivity (5 $\sigma$ )	$2 \times 10^{-8} \sqrt{T/1s} \text{ erg cm}^2 \text{ s}^{-1}$
Number of Bursts Detected	approximately 100 localizations per year

<sup>1</sup> <https://www.swift.psu.edu/>.

The XRT is a narrow-field X-ray telescope, which performs imaging and spectroscopy in the 0.2-10 keV energy band. Localization of a GRB with a XRT usually takes 3-5 arcseconds (the XRT's all parameters in the Table 1.2).

- Ultraviolet/Optical telescope (UVOT)

The UVOT is a narrow-field ultraviolet/optical telescopes, which performs broad-band imaging of the sources or GRBs at wavelengths between 1600 – 6000 Å. UVOT is also widely used for taking grim spectra in the narrow range between 1700 – 2900 Å wavelengths.

**SWIFT XRT:** The X-ray telescope (XRT) [44] is a focusing X-ray telescope, which perform observations in the 0.2-10 keV energy range (the XRTs' all parameters are listed in the

Table 1.2). By the help Wolter 1 telescope the XRT focuses X-rays onto a CCD-22 detector, which is a three-phase frame-transfer device. The CCD-22 consists 600 × 602 pixels image area. With this kind of structure, the XRT telescope can measure the fluxes, spectra and light curves of different sources, in the large waveband, with a sensitivity of a few orders of

Table 1.2: The X-ray telescopes (XRT) parameters.

XRT Parameter	Value
Energy Range	0.2-10 keV
Telescope	Wolter 1
Detector	E2V CCD-22
Effective Area	120 cm <sup>2</sup> at 1.5 keV
Detector Operation	Photon-counting, integrated imaging, and
Field of View	23.6 × 23.6 arcminutes
Detector Elements	600 × 602 pixels
Pixel Scale	2.36 arcseconds
Telescope PSF	18 arcseconds HPD at 1.5 keV
	22 arcseconds HPD at 8.1 keV
Sensitivity	8 × 10 <sup>-14</sup> erg cm <sup>2</sup> s <sup>-1</sup> in 10 000 s

magnitude in flux. The XRT resolution has been degraded during the working years, so by the help of the updating software corrections for the charge of the loss. The evolution of the XRT spectral resolution is discussed in [45].

The XRT carries out observation in four modes making possible the triggering of an event with rapid variability and in large range:

- Imaging Mode

In this mode the telescope composes a unified image, by computing the total energy per pixel, but in this method, spectroscopy is not allowed.

- Photodiode Mode

In contrast to imaging mode, in photodiode mode spectroscopy is possible. This mode used to get data from a bright, variable sources. This mode currently is not available.

- Windowed Timing Mode

In this mode spectroscopy also is available, but for limited flux range. This mode is used to deriving one-dimensional position information, with the high resolution timing.

- Photon-Counting Mode

In this mode XRT obtains full spectral and spatial information, which is used for the strong sources, when their fluxes are above than the XRTs sensitivity limit.

**SWIFT UVOT:** The Ultraviolet/Optical telescope (UVOT) [46] is a narrow-field Ritchey-Chrétien telescope, which have operating wavelength range of 1600 – 6000 Å. It has two mirrors made from zerodur, first has 30 cm diameter, the second one is a secondary mirror with 7.2 cm diameter. The UVOT's f-number is a  $f/2.0$ , but after passing secondary it increases to the  $f/12.72$ . All other parameters of UVOT are listed in the

Table 1.4. The light passes through a filter wheel, which contains elements mentioned below: UV grism, UV W2-filter, Optical V-filter, UV M2-filter, Optical grism, UV W1-filter, Optical U-filter, magnifier (4 times increase), Optical B-filter, and white light filter. The parameters of the UVOT filters are listed in the Table 1.3.

It has been found that by the temperature varying the PSF of UVOT is varies too. The effects of this time-dependent variation have been discussed in section 2.2 of [47].

The UVOT carries out observations in three basic modes:

Table 1.3: The Ultraviolet/optical telescopes (UVOT) filters.

Filter	$\lambda_0(\text{\AA})$
v	5402
b	4329
u	3501
uvw1	2634
uvm2	2231
uvw2	2030
white	3471

Table 1.4: The Ultraviolet/Optical telescopes' (UVOT) technical parameters.

UVOT Parameter	Value
Telescope	Modified Ritchey-Chrétien
Aperture	30 cm diameter
f-Number	$f/12.72$
Detector	Intensified CCD
Detector Operation	Photon Counting
Field of View	$17 \times 17$ arcminutes
Detection Elements	$256 \times 256$ pixels
Sampling Elements	$2048 \times 2048$ pixels after centroiding
Telescope PSF	approximately 2.5 arcseconds FWHM
Wavelength Range	1600 – 6000 $\text{\AA}$
Filters	11
Sensitivity	B = 22.3 in white light in 1000 s
Virtual Pixel Scale	0.502 arcseconds
Timing Resolution	11.0329 ms
Gain	1.0 count $\text{ADU}^{-1}$
Readout Noise	0.0 count $\text{s}^{-1} \text{pixel}^{-1}$
Dark Current	$7 \times 10^{-5}$ count $\text{s}^{-1} \text{pixel}^{-1}$

- Event

In this mode UVOT reports the position and the time information of each photon event. Collected data in this mode is very big, so due to limitation of the spacecraft memory capabilities, there are some limitations on duration for collecting data.

- Image

In this mode UVOT provides two-dimensional image of the event over the specified time. In this mode image presented binned (e.g.,  $1 \times 1$ ,  $2 \times 2$  or  $4 \times 4$  binning). In compare of event mode, the data taken in image mode requires much less memory.

- Event & Image

In this mode UVOT provides data collected in both modes.

**FERMI TELESCOPE:** The Fermi  $\gamma$ -ray space telescope (Fermi), formerly called the GLAST (Gamma-ray Large Area Space Telescope), was launched aboard Delta II 7920-H rocket on 11 June 2008. The mission is a joint mission of NASA, the United States Department of Energy, and government agencies in France, Germany, Italy, Japan, and Sweden. Fermi performs observations from low Earth orbit, at an altitude of 550 km, and at an inclination of 28.5 degrees and in sky survey mode observes all sky in  $\approx 3$  hours. Fermi carries two instruments on it: LAT (Large Area Telescope) and GBM (Gamma-ray Burst Monitor). LAT is a pair conversion telescopes, which performs observations in a 20 MeV – 1 TeV energy band. GBM is designed for detection of  $\gamma$ -ray bursts, it consists of 12 sodium iodide (NaI) scintillators with 12.7 cm diameter and 1.27 cm thickness, and two bismuth germanate (BGO) scintillators, with 12.7 cm diameter and 12.7 cm thickness (see [132]). GBM is sensitive from a few keV to  $\approx 30$  MeV.

**FERMI-LAT (Large Area Telescope):** The LAT is the primary instrument on Fermi. Main parameters are listed in the Table 1.5. The  $\gamma$ -ray photons are detected through pair conversation. Pair conversion is a mechanism by which a photon can be converted to an electron-positron pair. For this kind of mechanism photon should have energy at least twice of the rest mass of an electron. When the photons enter into the LAT, electron-positron pairs are generated and by reconstructing their trajectories, it is possible to determine direction of the initial photons. The Fermi-LAT contains three sub-structures: tracker, calorimeter and

anticoincidence detector.

The LAT is made of  $4 \times 4$  array (16) identical tower modules. Each tower has  $40 \times 40 \text{ cm}^2$  size and contains a tracker, calorimeter and data acquisition module. (Figure 1.5)

- Tracker

Pair conversion is taking place in tracker (Figure 1.5). The tracker detector has 18 (x, y) paired silicon strip detectors (SSD), which are interleaved with a tungsten foil, where the pair conversion process is taking place. So,  $\gamma$ -ray photons by passing tungsten foil will be converted to electron/positron pairs, and silicon strip detectors will measure the trajectories of generated charged particles. In order to receive better PSF (point spread function), better effective area, and for minimizing multiple scattering effects the tracker is divided in front and back sections. First 12 layers called “front section” with 0.027 radiation lengths, the next 4 layers are “back section” with 0.18 radiation lengths, and the last two layers are for triggering, and do not contain any tungsten, as

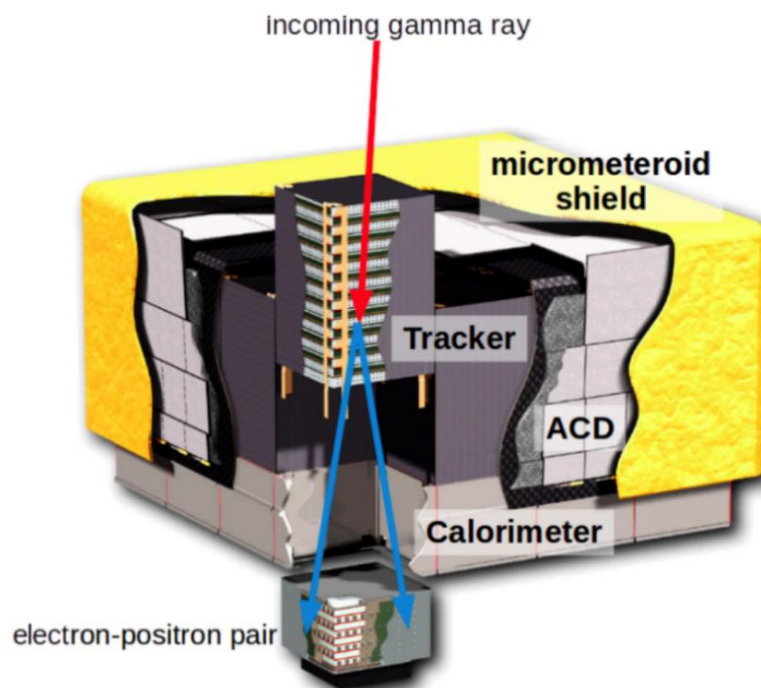


Figure 1.5: The Fermi-LAT subsystems, showing how pair conversion works. [48]

tracker trigger requires at least 3 hits in neighbouring layers to trigger. This kind of technology was chosen, because of effective application in accelerator-based high energy physics. This technology has high detection efficiency, large signal-to-noise ratio, good position resolution, easily triggering and negligible cross-talk.

- Colorimeter

After the trackers layers particles enter colorimeter (Figure 1.5). Calorimeter is made of 96 caesium iodide crystals (Csl) with a size of 2.7 cm × 2.0 cm × 32.6 cm, arranged in optically isolated horizontally 8 layers of 12 crystals each. The calorimeters vertical depth is 8.6 radiation lengths. In the colorimeter the charged particles interact with the caesium iodide crystal, and as a result the total energy of the incoming  $\gamma$ -ray photon can be reconstructed using the deposited energy from caused electromagnetic shower. The colorimeter has two main purposes:

- 1) Measure the energy deposition of the electromagnetic shower of particles resulting from the  $\gamma$ -ray photons pair conversion.
- 2) Perform three-dimensional imaging of the shower, which can serve as a measurement of shower energy outflow.

The three-dimensional imaging of the shower allows increase the LAT's energy range above 300 GeV, by measuring the shower development and estimation that showers,

Table 1.5: Fermi-LATs' technical parameters.

Quantity	LAT (Minimum Spec.)
Energy Range	20 MeV - 300 GeV
Peak Effective Area	> 8000 $cm^2$
Field of View	> 2 sr
Angular Resolution	< 3.5° (100 MeV) < 0.15° (>10 GeV)
Energy Resolution	< 10%
Deadtime per Event	< 100 $\mu s$
Source Location Determination	< 0.5'
Point Source Sensitivity	< 6 × 10 <sup>-9</sup> $cm^2 s^{-1}$

which are not fully contained in the instrument [49].

- Anticoincidence detector

The anticoincidence detector (ACD) surrounds tracker towers (Figure 1.5). The ACD is used for rejection of background charged particles. As except of  $\gamma$ -rays there are a

lot of background, which may come from interaction of other cosmic rays with Earth's atmosphere or in calorimeter can be produced secondary particles, which can hit ACD and bring to creating false “event”. This effect was present in the LAT’s predecessor, in the EGRET (Energetic Gamma-Ray Experiment Telescope) instrument, which had low efficiency of detection  $\gamma$ -ray photons above 10 GeV. For rejection a charged particles in the background and overcoming backplash effects in LAT is used ACD [50], which is made up of 89 segmented plastic scintillator and bundles of scintillation fibres in-between the tiles. With this design a charged particle rejection is over 99.97 %.

**IRFs (Instrument Response Functions):** The LAT’s Instrument Response Functions (IRFs) are parametrization of the LAT’s performance, which are a function of photon energy, incidence angle and other parameters. For better IRF’s, a lot of Monte Carlo (MC) simulations were generated with the aim of covering all possible photon energies and inclination angles with good statistics. The IRFs can be derived by comparison between the properties of the input photons and simulated events. The IRF is factorized into three terms: the LAT’s effective area in term of efficiency, the LAT’s point spread function (PSF) and energy dispersion in term of resolution.

- Point Spread Function  $P(v'; E, v)$ : The LAT’s point spread function (PSF) is a function of an incident photon's energy and inclination angle, and the event class. PSF represents the LAT’s angular resolution. PSF shows the probability density for reconstructed  $\gamma$ -ray photon with position  $v'$ , if for given energy  $E$  true position is  $v$ . PSF has first order dependency with energy.
- Effective Area  $A_{\text{eff}}(E, v)$ : The LAT’s effective area shows the detection efficiency of a  $\gamma$ -ray photon with energy  $E$ , at a given cut  $s$  and direction  $v$ . It equals to the product of the LAT’s geometric cross section and a term, which describes the detecting and reconstruction efficiency of the  $\gamma$ -rays. It is measured in area unit.
- Energy Dispersion  $D(E'; E, v)$ : The LAT’s energy dispersion in terms of definition is a fractional difference between the true energy  $E$  and the reconstructed energy  $E'$  and represents the LAT’s energy resolution. Energy dispersion shows the probability

density for reconstructed  $\gamma$ -ray photon with energy  $E'$ , if for given direction  $\hat{p}$ , true energy is  $E$ . For energies few hundred MeV the impact of energy dispersion on the broadband spectral analyses is relatively small ( $< 5\%$ ), so it can be ignored.

Consideration of all values described above we can compute the expected numbers of events from a given source with this equation:

$$N_{pred} = \int dE d\hat{p} S_i(E, \hat{p}) \epsilon(E, \hat{p}) \quad (2.1)$$

where  $\epsilon(E, \hat{p})$  is the integral of the total response over the ROI, which is:

$$\epsilon(E, \hat{p}) = \int dE' d\hat{p}' dt R(E', \hat{p}'; E, \hat{p}, t) \quad (2.2)$$

where  $E'$  is the measure energy, and  $\hat{p}'$  is the measured directions and  $S_i(E, \hat{p})$  is the  $\gamma$ -ray sources' model (point or extended source, background isotropic and Galactic diffuse emissions models).

All the data used in this work is PASS 8 processed. PASS 8 is the recent LAT event-level reconstruction update [51]. It consists a lot of improvements, such as background rejection, event reconstruction method, and MC simulations, related to the LAT's event selection process.

**LIKELIHOOD:** The main aim of the data cleaning, processing and receiving is to obtain physical results. In order to analyse the LAT's data special tool ("Fermitools") was developed by Fermi-LAT collaboration with the maximum likelihood method included in it. The likelihood  $L$  is the probability of the input model obtaining the data. The input model, in our case, is the distribution of  $\gamma$ -ray sources on the sky in the ROI (Region of interest), which include their spectra and intensity. This model includes spectral parameters values and positions of the sources in the ROI, diffuse emissions model and the functional form of their spectra. The purpose of "Fermitools" is by getting input model file finding the best spectral parameters, which will describe the data with the highest probability. The package varies spectral parameters of the sources in the input model, till the best parameters will be obtained, which can be received by finding the maximum value for the likelihood. It can be used for getting better results, as minimizing the value of  $\chi^2$  we will have maximum value for the likelihood, as  $\chi^2 = -2 \log L$ . For the better results, it is necessary to let vary also the spectral parameters

of the nearby sources, because the data also includes counts from these sources. But as it was mentioned the algorithm will find the best spectral parameters values and it will not fit coordinates for finding location. It is appropriate to use quantity “Test Statistic” (“TS”), which is mapping out maximum likelihood value over a grid of locations. The TS is defined as  $TS = -2 \ln L/L_0$ , where  $L$  is the likelihood value for a model without an additional source (the null hypothesis) and  $L_0$  is the likelihood value for a model with an additional source (more complex hypothesis). Wilks’ theorem states, that in the limit of a large number of counts, the TS for detection of a point source (the null hypothesis) will be asymptotically distributed as a  $\chi_n^2$  distribution, where  $n$  is the number of parameters specify the additional source [52]. Therefore, a bigger TS value indicates that the null hypothesis is incorrect. Also, the square root of the TS value roughly equals to the sources’ detection significance.

As the all parts are described, now we can show how likelihood is calculated. In the case of large data sets, it is more convenient to use binned likelihood method. The data will be binned in both energy and position on the sky. In each bin the number of observed counts can be characterized by a Poisson distribution. Let’s assume  $m_i$  is the expected number of counts of  $i$ -th bin given by the model. The probability of detecting  $n_i$  counts in  $i$ -th bin is:

$$P_i = m_i^{n_i} \times \frac{e^{-m_i}}{n_i!} \quad (2.3)$$

The likelihood in the functional form is the product of all bins’ probability of observing the detected counts. The likelihood  $L$  defines as:

$$L = \prod P_i \quad (2.4).$$

This product can be subdivided to two factors, first factor is  $\prod e^{-m_i}$ , which equals to,  $e^{-\sum m_i}$ , where  $\sum m_i$  is the total number counts  $N_{exp}$ , that model predicts which will be detected. So, we will have:

$$L = e^{-N_{exp}} \times \frac{m_i^{n_i}}{n_i!} \quad (2.5)$$

The basis for the binned likelihood analysis, is the finite size bins and counts number in the bin  $>1$ . If we let bin sizes to get infinitesimally small, we will have  $n_i = 0$  or  $n_i = 1$ , in this case we will have:

$$L = e^{-N_{exp}} \times \prod m_i$$

which is the basis for unbinned likelihood analysis. For a small number of counts this type of likelihood is the more accurate, and can be calculated swiftly, but if the number of counts increasing, the calculation time correspondingly decreases, in this case the binned likelihood is preferable.

## 2 X-RAY SPECTRA, LIGHT CURVES AND SEDS OF BLAZARS FREQUENTLY OBSERVED BY SWIFT

### 2.1 INTRODUCTION

Blazars are the most powerful non-explosive sources in the Universe. They are central to today's extragalactic high-energy astrophysics as they are by far the most common type of  $\gamma$ -ray sources at high Galactic latitudes [53, 54], and are expected to be abundantly detected in the very high-energy ( $E \gtrsim 50$  GeV)  $\gamma$ -ray sky that will soon be surveyed by a new generation of VHE observatories such as CTA [55] and LHAASO [56]<sup>2</sup>.

In this chapter will be presented a detailed X-ray spectral, imaging and timing analysis of all the observations and single snapshots<sup>3</sup> of a sample of 65 blazars that have been observed by Swift more than 50 times over a period of 16 years, from launch to the end of 2020. The resulting science-ready data products are used to compile the SED and X-ray lightcurve of each source in the sample. All the results are available through the Open Universe platform, the ASI SSDC, the Virtual Observatory (VO), and through other data release methods. In particular, all the SED data points and lightcurves are accessible through the VOU-blazars tool [6].

This work is meant to be a contribution to the goal of creating a high-transparency database, dedicated to blazars, based on the most advanced principles of open data access and behavioural insight approaches<sup>4</sup>.

### 2.2 BLAZARS FREQUENTLY OBSERVED BY SWIFT-XRT

Although specifically designed for Gamma Ray Burst science, Swift has proven to be an extremely effective multi-purpose multi-frequency observatory. A large number of bright and highly variable X-ray sources have been observed many times between launch in November

---

<sup>2</sup> <http://english.ihep.cas.cn/lhaaso>

<sup>3</sup> A Swift observation snapshot is the time interval spent continuously observing a target. A complete observation is composed of one or more snapshots sharing the same observation ID

<sup>4</sup> <https://www.oecd.org/gov/regulatory-policy/behavioural-insights.htm>

2004, and the end of 2020. The list of blazars that have been observed at least 50 times in this period with the XRT, [44] is given in Table 2.1, where column 1 is the source common or historical name, column 2 is the name of the object in the BZCAT [57] or the 3HSP catalogues [58], or following the IAU denomination in case the object is not listed in these two catalogues, column 3 gives the SED classification of the blazar (LBL, IBL or HBL), column 4 gives the number of XRT observations with exposure larger than 200 seconds in Photon Counting (PC) or Windowed Timing (WT) mode (see [44], for details of the readout modes), column 5 gives the ratio between the minimum and maximum flux observed at 1 keV. The list includes 65 objects, 24 of which are HBLs, 12 are IBLs and 29 are LBLs. The sky distribution of the subsample of sources observed more than 100 times shown in Figure 2.1 shows that the blazars most pointed by Swift are mostly located in the northern sky.

Although the data presented in this work is probably the largest available set of homogeneous X-ray measurements of blazars, it is far from being a collection of observations carried out at random times on a sample of randomly selected sources that would be needed for an unbiased view of blazars. Any statistical consideration based on the results presented here should therefore take into account of possible significant selection biases.

## 2.3 DATA PROCESSING

Data reduction and scientific analysis was performed using `Swift_xrtproc`, a software tool developed in cooperation between the Open Universe team and the ASI Space Science Data Center (SSDC). This tool uses the XRT Data Analysis Software (XRTDAS<sup>5</sup>), and the spectral and imaging analysis tools XSPEC and XIMAGE, included in the HEASoft package<sup>6</sup>, currently released as version V6.28.

**SWIFT\_XRTPROC:** `Swift_xrtproc` executes a complete data reduction, from XRT raw data to calibrated data products. The spectral and imaging data taken in PC or WT mode are analysed following standard procedures. The main steps that are performed on each Swift-XRT observation are:

- i. Automatic download of raw data and calibration files from one of the official Swift

---

<sup>5</sup> Developed under the responsibility of the ASI SSDC

<sup>6</sup> <https://heasarc.gsfc.nasa.gov/docs/software/heasoft/>

Table 2.1: The sample of blazars observed by Swift XRT in PC or WT mode more than 50 times from launch in November 2004 to November 2020.

Common or discovery name (1)	5BZB or 3HSP IAU denomination (2)	SED type (3)	Obs. With good spectra (4)	$f_{max}/f_{min}$ @ 1keV (5)
1ES0033+595	3HSPJ003552.6+595004	HBL	141	8.3
PKS0208-512	5BZUJ0210-5101	LBL	161	31.7
3C66A	5BZBJ0222+4302	IBL	109	16.2
1ES0229+200	3HSPJ023248.6+201717	HBL	80	3.8
PKS0235+164	5BZBJ0238+1636	LBL	185	172.8
1H0323+342	5BZUJ0324+3410	IBL	147	6.8
1ES0414+009	3HSPJ041652.5+010524	HBL	51	4.3
3C120	5BZUJ0433+0521	LBL	176	4.3
PKS0506-61	5BZQJ0506-6109	LBL	59	4.0
TXS0506+056	5BZBJ0509+0541	IBL	82	13.4
GB6J0521+2113	3HSPJ052146.0+211251	HBL	81	110.4
5BZQJ0525-4557	5BZQJ0525-4557	LBL	51	7.2
PKS0528+134	5BZQJ0530+1331	LBL	134	25.2
RXSJ05439-5532	3HSPJ054357.2-553208	HBL	77	7.9
PKS0548-322	3HSPJ055040.6-321616	HBL	63	3.8
PKS0637-752	5BZQJ0635-7516	LBL	67	3.5
1ES0647+250	3HSPJ065046.5+250360	HBL	60	8.4
5BZBJ0700-6610	5BZBJ0700-6610	IBL	65	7.9
EXO0706.1+5913	3HSPJ071030.1+590821	HBL	64	5.3
S50716+714	5BZBJ0721+7120	IBL	329	69.6
3FGLJ0730.5-6606	3HSPJ073049.5-660219	HBL	64	24.6
GB6J0830+2410	5BZQJ0830+2410	LBL	104	48.9
S50836+71	5BZQJ0841+7053	LBL	77	5.5
GB6J0849+5108	5BZUJ0849+5108	LBL	56	20.9
OJ287	5BZBJ0854+2006	IBL	670	122.5
PKS0921-213	5BZUJ0923-2135	LBL	95	5.0
S40954+658	5BZBJ0958+6533	LBL	58	57.0
1ES1011+496	3HSPJ101504.1+492601	HBL	48	12.5
Mrk421	3HSPJ110427.3+381232	HBL	1163	107.4
PKS1130+009	5BZQJ1133+0040	LBL	58	13.9
GB6J1159+2914	5BZQJ1159+2914	LBL	75	17.3
MS1207.9+3945	3HSPJ121026.6+392908	HBL	411	6.5
1ES1218+304	3HSPJ122122.0+301037	HBL	113	12.5
ON231	5BZBJ1221+2813	IBL	120	82.0
PKS1222+216	5BZQJ1224+2122	IBL	113	10.5
3C273	5BZQJ1229+0203	LBL	326	10.2
3HSP	3HSP J123800+263553	HBL	83	5.5
3C279	5BZQJ1256-0547	LBL	421	11.4
PKS1406-076	5BZQJ1408-0752	LBL	82	8.6
PKS1424+240	5BZBJ1427+2348	LBL	85	16.3
PKS1424-41	5BZQJ1427-4206	LBL	63	7.4
H1426+428	3HSPJ142832.6+424021	HBL	179	3.8
PKS1502+106	5BZQJ1504+1029	LBL	105	8.9
PKS1510-08	5BZQJ1512-0905	IBL	267	6.8

Table 2.1 - continued

1H1515+660	3HSPJ151747.6+652523	HBL	54	5.7
4FGLJ1544.3-0649	J154419.7-064916	HBL	50	34.7
PG1553+113	3HSPJ155543.1+111124	HBL	333	21.6
PKS1622-297	5BZUJ1626-2951	LBL	85	122.7
B31633+382	5BZQJ1635+3808	LBL	144	27.2
Mrk501	3HSPJ165352.2+394537	HBL	738	16.6
IZW187	3HSPJ172818.6+501311	HBL	160	13.1
PKS1730-130	5BZQJ1733-1304	LBL	93	14.0
S41749+701	5BZBJ1748+7005	IBL	57	12.2
S51803+784	5BZBJ1800+7828	LBL	72	6.0
3C371	5BZBJ1806+6949	IBL	62	10.0
EXO1811.7+3143	3HSPJ181335.2+314418	HBL	57	172.0
2E1823.3+5649	5BZBJ1824+5651	LBL	70	7.5
4C+56.27	5BZBJ1824+5651	LBL	66	7.5
PKS1830-211	5BZQJ1833-2103	LBL	72	3.8
1ES1959+650	3HSPJ195959.8+650855	HBL	487	20.0
PKS2155-304	3HSPJ215852.1-301332	HBL	240	57.3
BLLac	5BZBJ2202+4216	IBL	545	206.6
CTA102	5BZQJ2232+1143	LBL	138	20.8
3C454.3	5BZQJ2253+1608	LBL	414	24.4
1ES2344+514	3HSPJ234704.8+514218	HBL	184	10.3

archives.

- ii. Generation of exposure maps and calibrated data products, for each snapshot and for the entire Swift observation, using the XRTPipeline task and adopting standard parameters and filtering criteria.
- iii. Source and background spectral files generation. The source counts are estimated in a circle of 20 pixels radius when no pile-up<sup>7</sup> is present. For the case of PC mode, the background is extracted in an annular region centred around the source with radius sufficiently large to avoid contamination from source photons. For the WT mode the spectrum of the background is estimated from a deep observation taken from the XRT archive.
- iv. Pile-up correction. A verification of the source count-rate is carried out to determine whether the data is affected by pile-up. In case pile-up is present the spectral data is extracted again excluding the central parts of the Point Spread Function, by taking counts in an annular region with inner radius chosen depending on the measured

---

<sup>7</sup> Pile-up occurs when more than one photon hits the same pixel in a period shorter than the XRT-CCD readout time, typically 2.5 seconds in PC mode

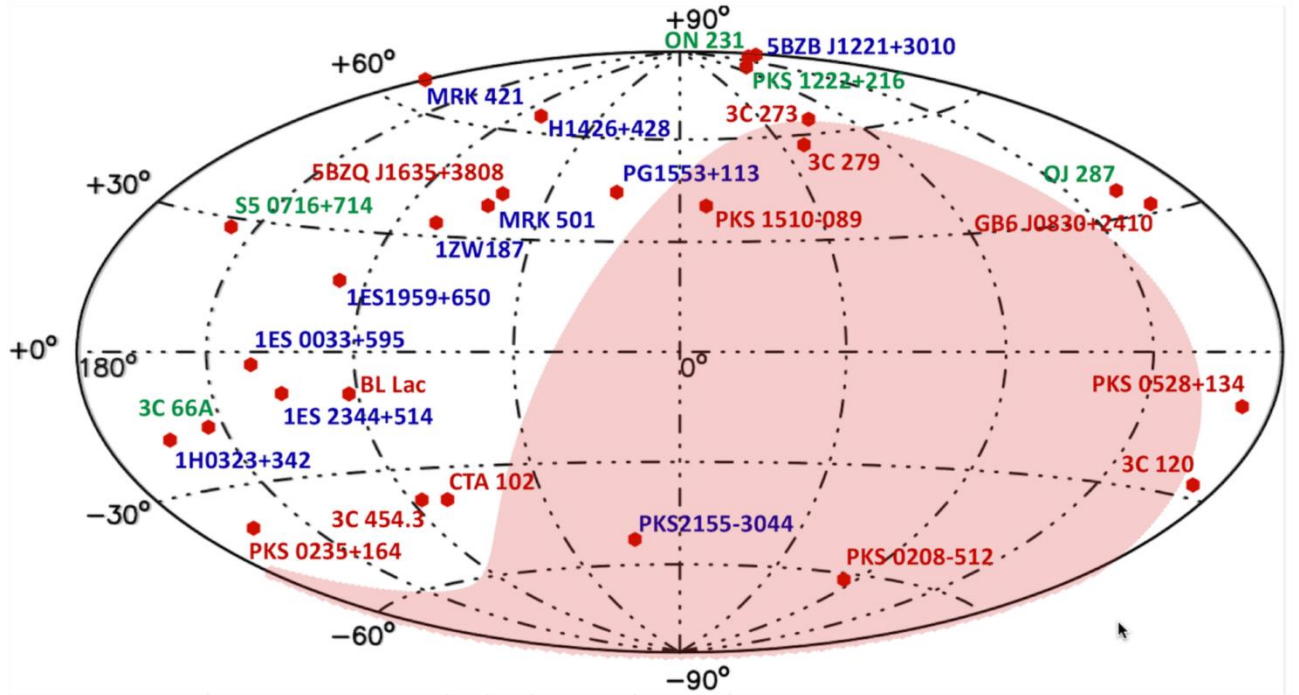


Figure 2.1: Hammer-Aitoff plot in Galactic coordinates showing the position of blazars that have been observed more than 100 times by Swift. The names of HBL sources appear in blue color, while those of IBLs and LBLs are green and red respectively. The light red area highlights the part of the sky south of the equator, illustrating how most of the blazars frequently observed by Swift are in the northern hemisphere.

count-rate [59].

- v. Spectral fitting using the XSPEC package [60] assuming a power-law and a log-parabola model.
- vi. Conversion of best fit spectral data to  $\nu f(\nu)$  units for SED plotting.
- vii. Photometric analysis using XIMAGE to estimate count-rates, or upper limits, in four energy bands: 0.3-1.0, 1.0-2.0, 2-10, and 0.3-10 keV, for data taken in PC readout mode.
- viii. Count-rate to X-ray flux conversion in the 0.5-10 keV and 2-10 keV energy bands and in  $\nu f(\nu)$  units at the energies of 0.5, 1.5 and 4.5 keV
- ix. Flux or upper limit estimation in  $\nu f(\nu)$  units at 1 keV either from the best fit spectrum or from the photometric data (in case the source is too weak for spectral fitting) suitable for light-curve generation and time domain analysis.

**SPECTRAL ANALYSIS:** We used the XSPEC spectral fitting package Version 12.11 to fit the X-ray data generated as described above to a power-law (eq. 3.1) and to a log-parabola (eq. 3.2) model, fixing the amount of absorbing column (NH) to the Galactic value.

Source name	RA (J2000.0) hh mm ss.d	Dec (J2000.0) dd mm ss	Phot index Photon index	Reduced chi2 red chisq pl	Alpha LP alpha_lp_with_err	Beta LP beta_lp_with_err	Reduced chi2 red chisq lp	Flux052 pl Flux 0.5-2	Flux210 pl Flux 2-10	Observation time mjd
3C273	12 29 06.5	+02 03 08	1.66±0.03	1.18	1.77±0.05	-0.23±0.08	1.1	3.3e-11±6.9e-13	6.7e-11±2.9e-12	53417.584
MRK501	16 53 52.2	+39 45 37	2.12±0.04	1.12	2.08±0.04	0.15±0.09	1.09	1e-10±2e-12	1e-10±6.9e-12	53426.042
MRK421	11 04 27.3	+38 12 32	2.7±0.01	1.01	2.69±0.02	0.05±0.04	1	8.8e-11±1.1e-12	3.9e-11±6.7e-13	53430.052
MRK421	11 04 27.3	+38 12 32	2.48±0.25	1.3	2.5±0.2	-1.07±0.8	0.95	2e-10±3.2e-11	1.2e-10±4.7e-11	53454.099
H1426+428	14 28 32.5	+42 40 19	2.01±0.06	1.21	2.04±0.08	-0.09±0.17	1.21	2.8e-11±7.8e-13	3.3e-11±2.6e-12	53460.004
H1426+428	14 28 32.5	+42 40 21	2.01±0.06	1.21	2.04±0.08	-0.09±0.17	1.21	2.8e-11±8.8e-13	3.4e-11±3.9e-12	53460.004
MRK421	11 04 27.3	+38 12 32	2.54±0.01	1.2	2.52±0.01	0.11±0.03	1.13	2.3e-10±1e-12	1.3e-10±1.1e-12	53460.043
1ES0033+595	00 35 52.6	+59 50 04	2.03±0.04	1.37	0.96±0.21	1.3±0.25	1.09	2.4e-11±8.1e-13	6.5e-11±2.1e-12	53461.032
MRK421	11 04 27.3	+38 12 32	2.4±0.01	1.24	2.36±0.01	0.16±0.03	1.05	3.6e-10±2.8e-12	2.5e-10±4.9e-12	53461.182
H1426+428	14 28 32.5	+42 40 19	2.02±0.03	0.93	2.03±0.04	-0.05±0.09	0.93	2.8e-11±5.5e-13	3.2e-11±1.9e-12	53462.952
H1426+428	14 28 32.5	+42 40 21	2.02±0.03	0.94	2.03±0.04	-0.05±0.1	0.94	2.8e-11±6.3e-13	3.3e-11±1.3e-12	53462.952
S50716+714	07 21 53.4	+71 20 35	2.16±0.2	1.31	2.69±0.65	-0.79±0.92	1.3	2.4e-12±2.4e-13	2.4e-12±6.8e-13	53462.979
S50716+714	07 21 53.4	+71 20 35	2.33±0.59	0.29	1.75±1.98	0.84±2.32	0.34	3e-12±1.2e-12	2.3e-12±1.3e-12	53464.715
1ES1959+650	19 59 59.5	+65 08 54	2.24±0.01	1.45	2.07±0.03	0.41±0.05	0.91	1.1e-10±1.4e-12	1.3e-10±1.6e-12	53479.046
1ES2344+514	23 47 04.9	+51 42 16	2.23±0.07	0.88	2.15±0.12	0.2±0.23	0.85	7.9e-12±2.6e-13	1e-11±6.5e-13	53479.052

Figure 2.2: A selection 15 lines from the on-line interactive and Virtual Observatory inter-operable table. The results of the analysis of all the spectral fits of the 65 blazars listed in Table 2.1 are accessible at <https://openuniverse.asi.it/blazars/swift>. A fits file including all the results is available at [https://openuniverse.asi.it/OU4Blazars/oublazars\\_swift\\_spectra\\_v1.0.fits.gz](https://openuniverse.asi.it/OU4Blazars/oublazars_swift_spectra_v1.0.fits.gz).

$$N(E) = k \times E^{-\Gamma} \quad (3.1)$$

where  $\Gamma$  is the photon index.

$$N(E) = k \times E^{-(\alpha+\beta \text{Log}(E))} \quad (3.2)$$

where  $\alpha$  is the photon spectral index at 1 keV and  $\beta$  is the curvature parameter. We chose these spectral shapes because they generally provide a good description of the X-ray spectra of blazars (e.g., [61]) while keeping the number of free parameters to a minimum. Cash statistics [62] was adopted for all spectral fits, grouping the data with the grppha tool to include at least one count in each energy bin [63].

**IMAGE ANALYSIS:** All the XRT observations that were carried out in PC mode were also analysed using the XIMAGE (V4.5.1) X-ray image analysis package<sup>8</sup>. The procedure used is equivalent to that implemented in the Swift\_deepsky tool [64, 65], which performs a photometric flux estimation using X-ray data in four energy bands: 0.3-10 keV (full band), 0.3-1.0 keV (soft band), 1.0-2.0 keV (medium band), and 2.0-10.0 keV (hard band). The

<sup>8</sup> <https://heasarc.gsfc.nasa.gov/xanadu/ximage/>

image background was measured using the XIMAGE/background command, and source counts were obtained using the XIMAGE/sosta tool centering on the target and counting events in boxes whose size includes 80% of the source flux (see [64], for more details). Spectral slopes were also estimated from the hardness ratio, defined as the ratio between the counts in the hard and soft bands. Count-rates (or upper limits) were converted to X-ray fluxes assuming  $N_H$  equal to the Galactic value, and a power-law spectrum with spectral index equal to the value estimated from the XSPEC spectral analysis when available or from the hardness ratio. When no spectral slope estimation was possible the spectral index was assumed to be equal to 1.8. Fluxes in  $\nu f(\nu)$  units, suitable for SED plotting, were calculated at the reference energies of 0.5, 1.5 and 4.5 keV. Finally, a second spectral slope estimation was obtained via a least square linear fit to the 0.5, 1.5 and 4.5 keV  $\nu f(\nu)$  fluxes.

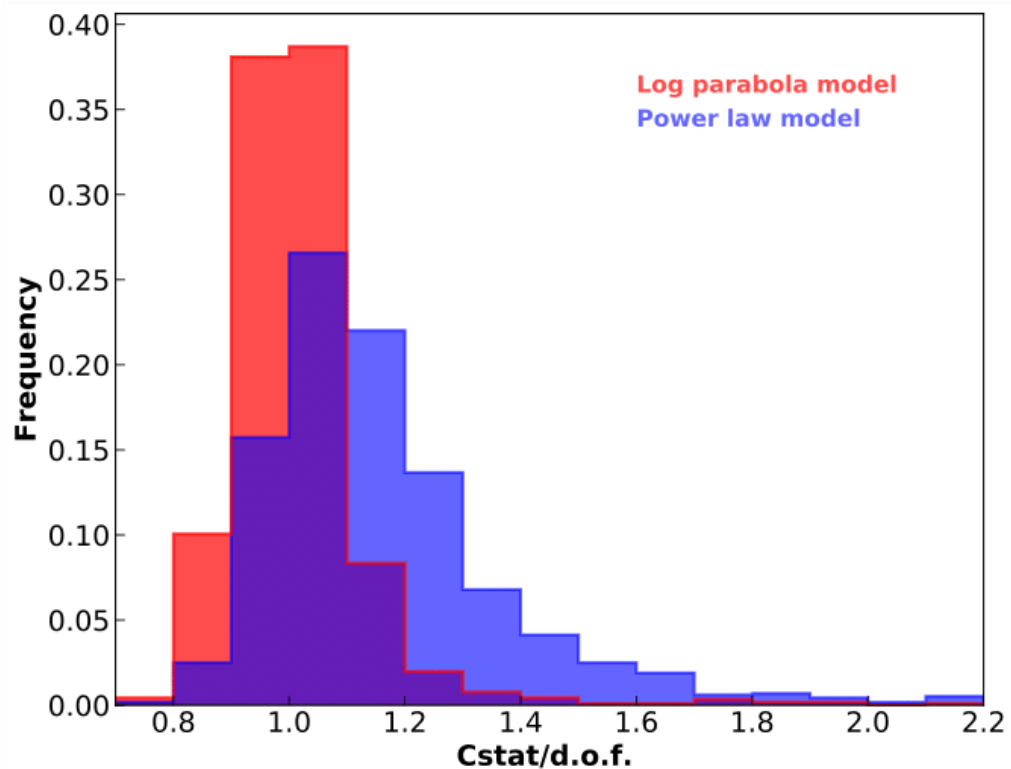


Figure 2.3: The normalised distributions of best-fit Cstat statistics divided by the number of degrees of freedom (Cstat/d.o.f.) for the power-law and log-parabola models for the case of the blazar Mrk 421. The log-parabola model gives systematically lower Cstat/d.o.f. values, implying that this model is clearly a better representation of the data for this blazar.

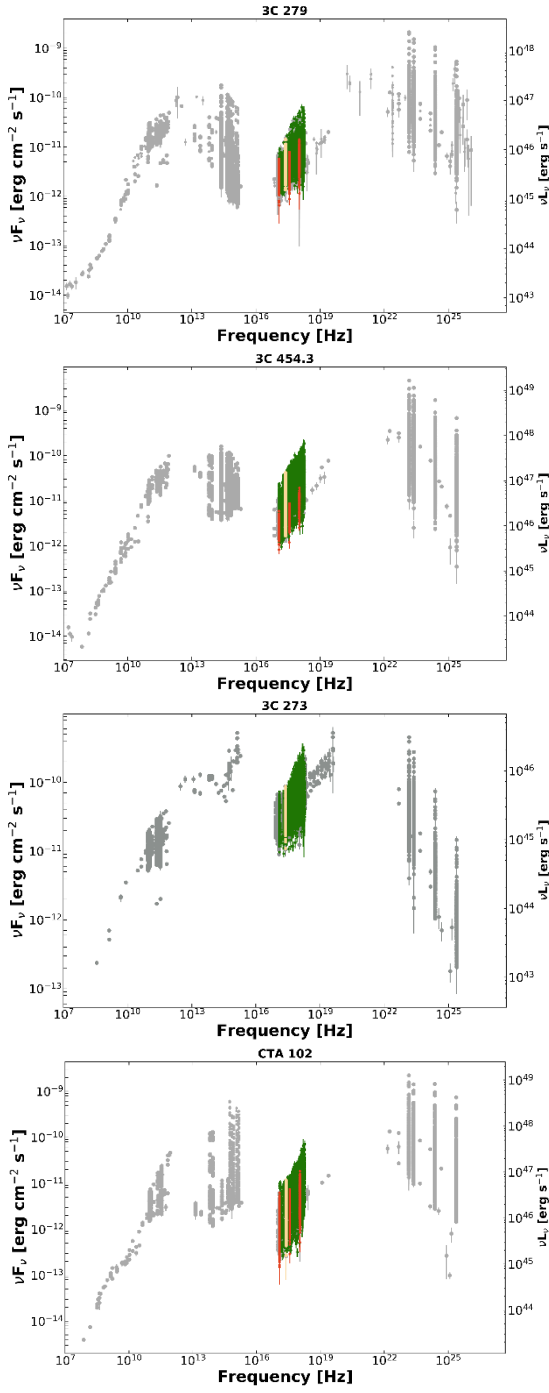


Figure 2.4: SED of representative LBL blazars showing the XSPEC best fit spectra (WT and PC mode, green points), the results of the XIMAGE photometric analysis (only PC mode, red points), the overall 1keV light curve points (light-yellow points) and archival multi-frequency data from VOU-Blazars (grey points).

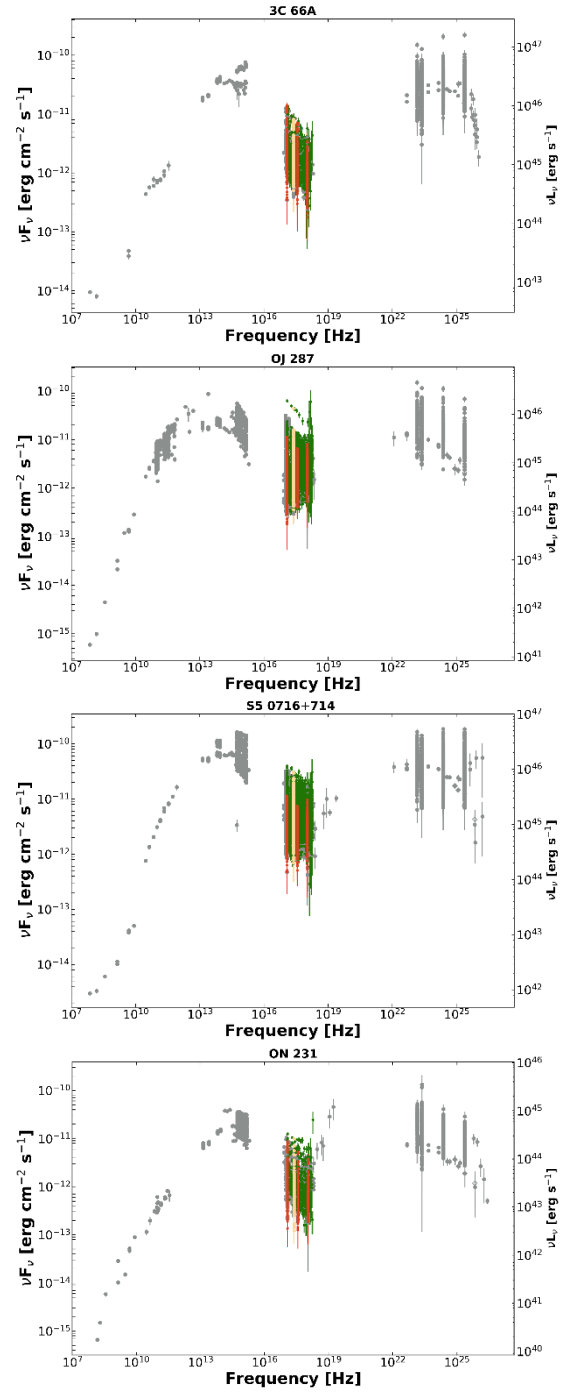


Figure 2.5: SED of representative IBL blazars showing the XSPEC best fit spectra (WT and PC mode, green points), the results of the XIMAGE photometric analysis (only PC mode, red points), the overall 1keV light curve points (light-yellow points) and archival multi-frequency data from VOU-Blazars (grey points).

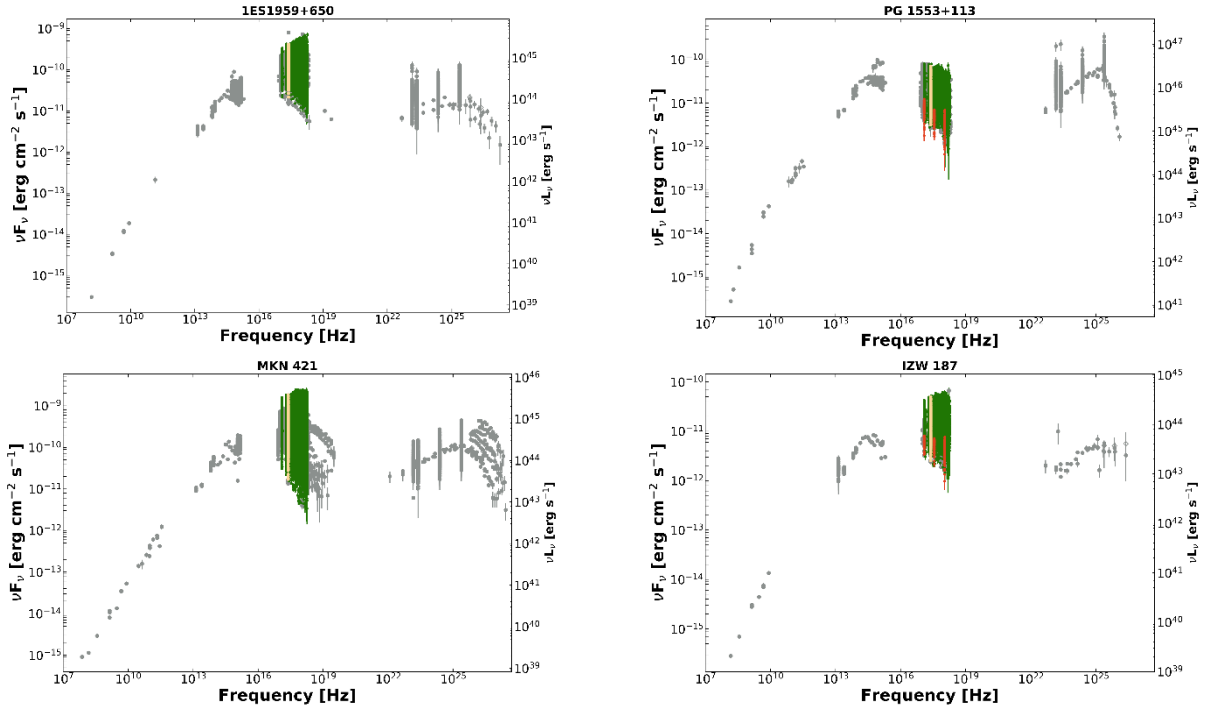


Figure 2.6: SED of representative HBL blazars showing the XSPEC best fit spectra (WT and PC mode, green points), the results of the XIMAGE photometric analysis (only PC mode, red points), the overall 1keV light curve points (light-yellow points) and archival multi-frequency data from VOU-Blazars (grey points).

## 2.4 RESULTS

We processed a total of 31,068 Swift XRT observations or individual snapshots of the 65 blazars listed in Table 2.1. This led to the generation of 29,050 X-ray spectra, 21,141 photometric flux estimations, and 206 upper limits.

**BEST-FIT PARAMETERS AND FLUXES:** The results of the XSPEC spectral fits for every spectrum including at least 20 source counts, are reported in the online interactive table available at webpage<sup>9</sup>, (see Figure 2.2). Column 1 gives the source name, columns 2 and 3 the J2000.0 Right ascension and Declination, columns 4 and 5 give the best-fit photon spectral index with error and the reduced  $\chi^2$ , columns 6, 7 and 8 give the  $\alpha, \beta$  best fit parameter and  $\chi^2$  for the log-parabola model, column 9 and 10 give the observed flux in the 0.5-2.0 keV and 2-10 keV bands, column 11 gives the observation time. The complete set of results are also available as a fits file<sup>10</sup>.

<sup>9</sup> <https://openuniverse.asi.it/blazars/swift>

<sup>10</sup> [https://openuniverse.asi.it/OU4Blazars/oublazars\\_swift\\_spectra\\_v1.0.fits.gz](https://openuniverse.asi.it/OU4Blazars/oublazars_swift_spectra_v1.0.fits.gz) whose structure is described in

Table 3.2

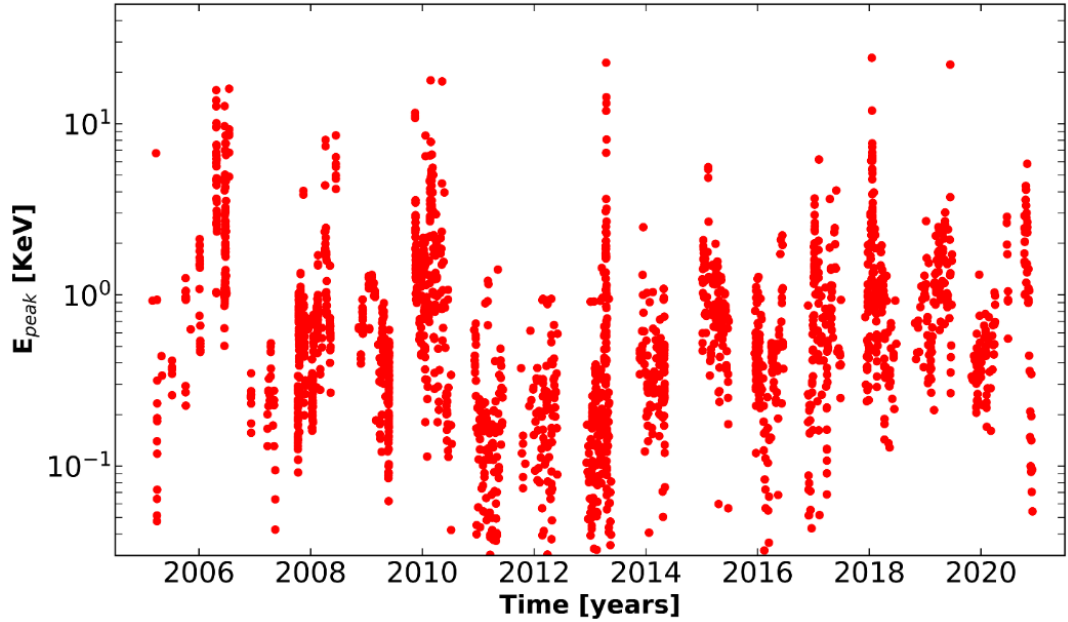


Figure 2.7: The remarkable changes of the synchrotron peak energy in the SED of Mrk 421 over a period of 16 years of Swift monitoring of this object.

**Power-law Vs Log-parabola models:** Our results confirm with large statistics that the log-parabola model generally fits best the X-ray spectral shape of HBL blazars, while LBL sources are usually best fit by a simple power-law. IBL blazars often show more complex spectra, as in these cases the steep end of the synchrotron component merges into the much flatter inverse Compton component in the X-ray band. As a particular example of HBL blazar, Figure 2.3 plots the distribution of the best-fit Cash statistics divided by the number of degrees of freedom ( $C_{\text{stat}}/d.o.f.$ ) values for the power-law and log-parabola fits of Mrk421. The sharper and lower value peaking red histogram for the case of log-parabola demonstrates that this spectral model is a better representation than a simple power-law. Similar results are obtained for most blazars of the HBL type. The X-ray spectra of IBL blazars are mostly characterised by a steep power-law spectrum since the XRT band-pass in these objects covers the end of the synchrotron tail and occasionally show the onset of the second SED hard component. The X-ray spectrum of LBL blazars is well represented by a simple power-law spectrum with a flat slope, with average value of  $\langle \Gamma \rangle = 1.46$ . In some cases, however, (see e.g., the SED of 3C 273 and CTA 102 in Figure 2.4) there is some evidence for a flattening toward the high-energy end of the XRT energy window. The spectral shapes described above can also be noted from a simple visual inspection of the SEDs of Figure 2.4, Figure 2.5 and

Figure 2.6, and those available in the online table at on-line resource<sup>11</sup>.

**IMAGING ANALYSIS:** The results of the imaging analysis, including count-rates, fluxes in the 0.5-10.0 keV and 2-10 keV bands,  $\nu f(\nu)$  fluxes at 0.5, 1.0, 1.5, and 4.5 keV, as well as two estimates of the spectral index, are given in the fits-formatted file mentioned above and described in Table 2.2.

**SPECTRAL ENERGY DISTRIBUTIONS:** The best-fit spectral data and the X-ray fluxes estimated from the imaging analysis have been combined with archival multifrequency data retrieved using the VOUBlazars software [6] to build the radio to  $\gamma$ -ray SED of each object in the sample. The VOUBlazars tool provides access to data from over 70 catalogues and spectral databases covering the entire electromagnetic spectrum. Figure 2.4, Figure 2.5 and Figure 2.6 give examples of SEDs of representative blazars of the LBL, IBL and HBL class. The SED of all the blazars in the sample are available online<sup>12</sup>. Grey points represent archival data, green symbols are the XSPEC best-fit spectral data, red points are from the XIMAGE/SOSTA measurements, and the light-yellow points are the 1 keV  $\nu f(\nu)$  fluxes

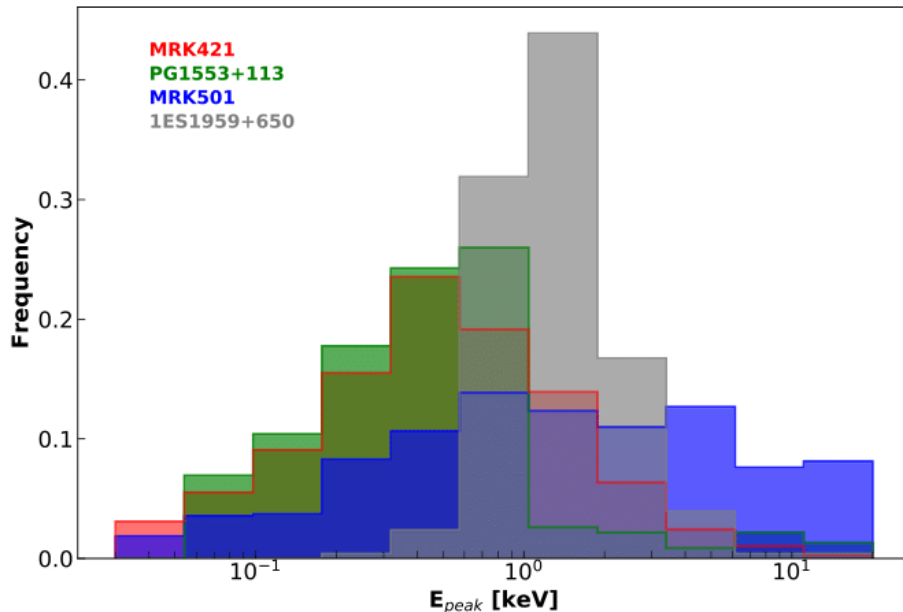


Figure 2.8: The distribution of the synchrotron peak energy observed in bright HBL blazars as examples representing the class. Large  $\nu_{peak}$  variations are commonly observed. Most of the other HBL sources in our sample show similar  $\nu_{peak}$  variations.

<sup>11</sup> <https://openuniverse.asi.it/blazars/swift>

<sup>12</sup> <https://openuniverse.asi.it/blazars/swift>

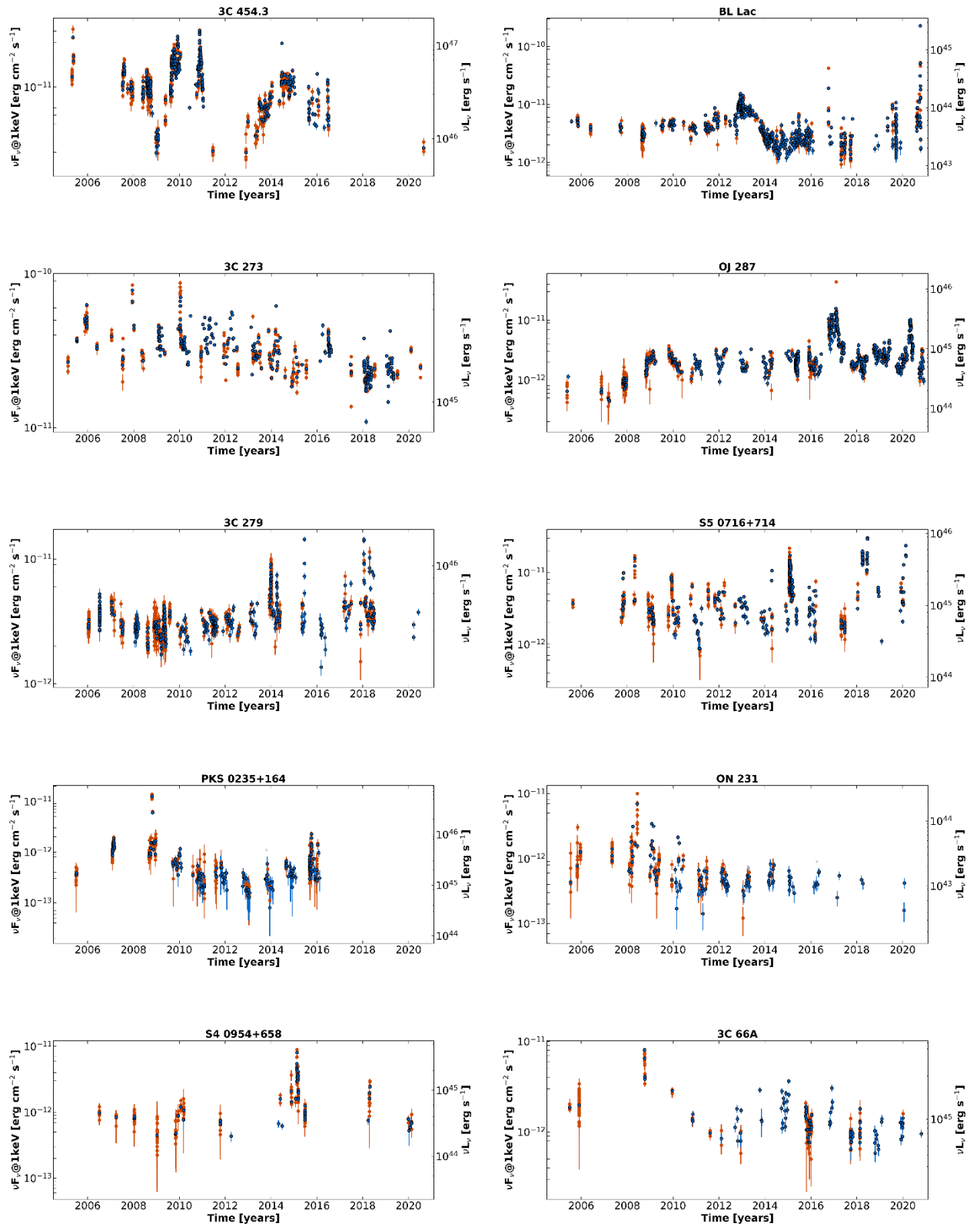


Figure 2.9: The 1 keV light curves of LBL blazars: 3C 453.4, 3C 273, 3C 279, PKS0235+164 and S4 0954+658.

Figure 2.10: The 1 keV light curves of IBL blazars: BL Lacertae, OJ 287, S5 0716+714, ON 231, and 3C 66A.

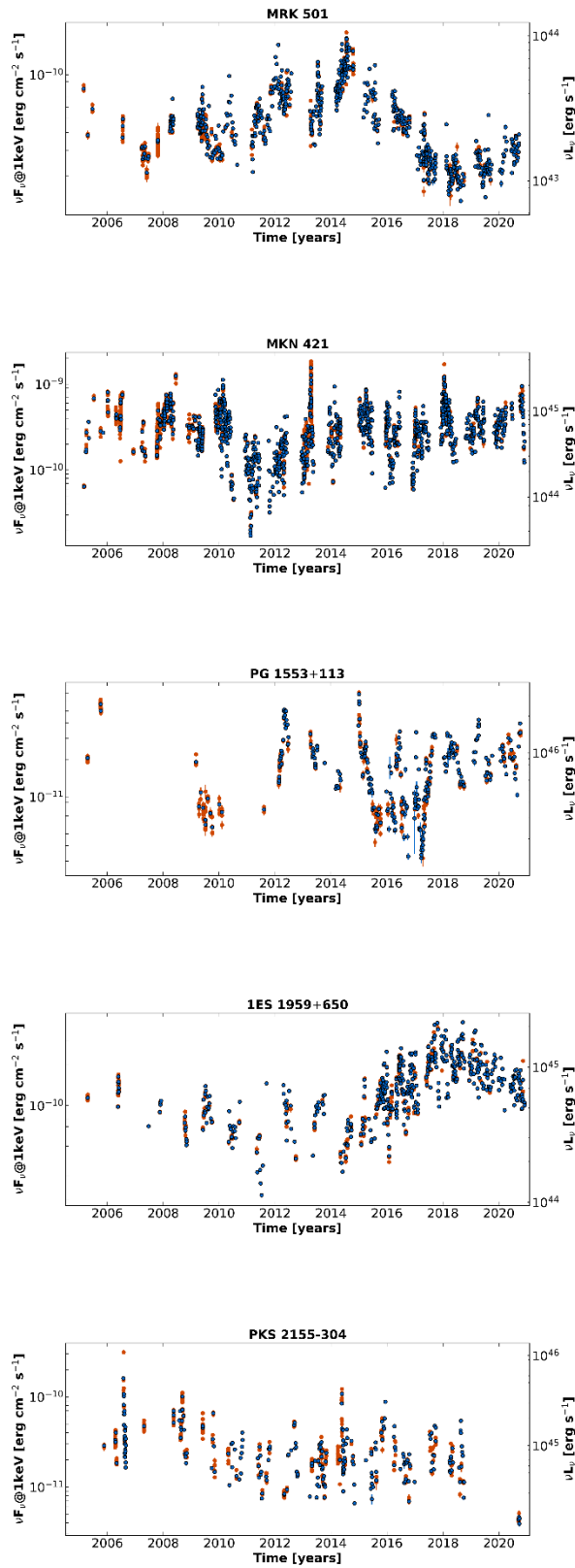


Figure 2.11: The 1 keV light curves of HBL blazars: Mrk 501, Mrk 421, PG1553+113, 1ES1959+650, and PKS2155-304.

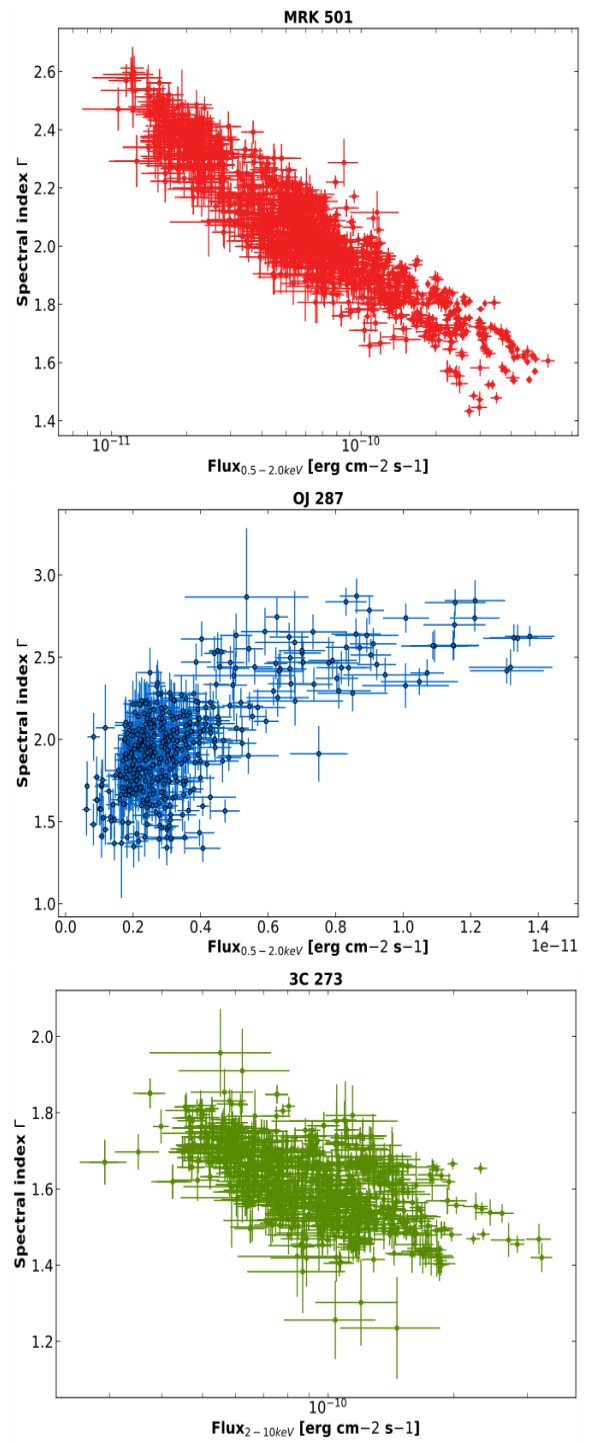


Figure 2.12: Plot of the power-law spectral slope versus X-ray flux for the HBL blazar Mrk501 (upper panel), for the IBL object OJ287 (middle panel), and 3C273 (lower panel) illustrating the various cases of harder-when-brighter, and softer-when-brighter behavior in blazar spectral variability.

calculated as described in section 3.4.4. Note that the red points are not present in a high-intensity states when the WT readout mode was used, reflecting the fact that imaging analysis was only performed when the XRT was operated in PC mode.

**SYNCHROTRON PEAK ENERGY ( $\nu_{peak}$ ):** Reliable values of  $\nu_{peak}$  can be estimated directly from the X-ray spectrum in all sources where the log-parabola model is a good fit to the data and  $\nu_{peak}$  is located inside or close to the XRT band-pass. From [61] we have

$$\nu_{peak} = 10^{(2-\alpha)/2\beta} \quad (3.3)$$

where  $\alpha$  and  $\beta$  are the parameters of eq. 3.2. We have calculated  $\nu_{peak}$  in all cases where well estimated values of  $\alpha$  and  $\beta$  could be obtained and eq. 3.3 gives values that are close or within the Swift-XRT X-ray band. We found that large variations of this parameter are detected in many objects. As an example of this behaviour Figure 2.7 plots  $\nu_{peak}$  as a function of time for the case of Mrk421, the object most frequently observed in the sample, showing frequent large changes spanning over two orders of magnitude, from below 0.1 to over 20 keV. Large  $\nu_{peak}$  changes are common in most HBL blazars, as illustrated in Figure 2.8 which plots the  $\nu_{peak}$  distribution of Mrk421 together with three other representative sources. Values close to the low and high energy ends of Figure 2.8 should be taken with caution (and perhaps treated as limits, see e.g., [66], since they are at the edge of the XRT energy range. However, the frequency of occurrence is low and the impact on the overall shape of the distribution is limited.

**TIME DOMAIN DATA:** In the following work are presented the 1 keV light-curves of all the blazars in the sample and briefly comments on the long-term variability and flux variations between neighbouring snapshot, based on visual inspection of the data. A comprehensive study of blazars temporal behaviour based on the data presented here will be the subject of a future publication.

For the light curves have been used 1 keV ( $\nu f(\nu)$ ) fluxes, calculated as the best-fit value (and statistical error) of the power-law normalisation, multiplied by  $1.6 \times 10^{-9}$ , to convert from XSPEC units to  $\text{erg cm}^{-2} \text{s}^{-1}$ , or converting to 1 keV the XIMAGE count-rate estimation in the soft band, when less than 20 source counts were detected, or  $3\sigma$  upper limits estimated with the XIMAGE/SOSTA command in case of non-detection.

Table 2.2: Content of the FITS file including the results of the spectral fits and of the image analysis

Column	Format	Units	Description
Blazar name	15A		Blazar name
R.A.	D	deg	Right Ascension in degrees (J2000.0 epoch)
Dec.	D	deg	Declination in degrees (J2000.0 epoch)
MJD	D	days	Modified Julian Day of observation start time
Obs_time	D	s	observation start time in units yyyy.ff where ff is the fraction of year
Sequence	A		Swift observation ID
Flux2_10-PL	D	erg cm <sup>-2</sup> s <sup>-1</sup>	2–10 keV flux from best-fit power-law model
Flux2_10-PL_error	D	erg cm <sup>-2</sup> s <sup>-1</sup>	1 sigma error on Flux2_10-PL
Flux05_2-PL	D	erg cm <sup>-2</sup> s <sup>-1</sup>	0.5–2.0 keV flux from best-fit power-law model
Flux05_2-PL_error	D	erg cm <sup>-2</sup> s <sup>-1</sup>	1 sigma error on Flux05_2-PL
Flux03_3-PL	D	erg cm <sup>-2</sup> s <sup>-1</sup>	0.3–3.0 keV flux from best-fit power-law model
Flux03_3-PL_error	D	erg cm <sup>-2</sup> s <sup>-1</sup>	1 sigma error on Flux03_3-PL
$\chi^2_r$ -PL	D		reduced $\chi^2$ for power-law model
Degrees of freedom-PL	D		degrees of freedom for power-law model
$\chi^2_r$ -LP	D		reduced $\chi^2$ for log-parabola model
Degrees of freedom-LP	D		degrees of freedom for log-parabola model
Photon_index	D		best-fit photon index for power-law fit
Photon_index_error	D		error on best-fit photon index for power-law fit
Normalization-PL	D		best-fit power-law normalization
Normalization-PL_error	D		error on best-fit power-law normalization
$\alpha$	D		best-fit $\alpha$ parameter for log-parabola fit
$\alpha$ _error	D		error on $\alpha$ parameter for log-parabola fit
$\beta$	D		best-fit $\beta$ parameter for log-parabola fit
$\beta$ _error	D		error on $\beta$ parameter for log-parabola fit
Normalization-LP	D		best-fit log-parabola normalization
Normalization-LP_error	D		error on best-fit log-parabola normalization
Snapshot	3A		swift snapshot number ‘TOT’ for full observation
$\nu f(\nu)$ @ 1.0 keV	D	erg cm <sup>-2</sup> s <sup>-1</sup>	$\nu f(\nu)$ flux at 1.0 keV
$\nu f(\nu)$ @ 1.0 keV_error	D	erg cm <sup>-2</sup> s <sup>-1</sup>	error $\nu f(\nu)$ flux at 1.0 keV
Datamode	2A		XRT data readout mode: PC or WT
I- $\nu f(\nu)$ @ 0.5 keV	D	erg cm <sup>-2</sup> s <sup>-1</sup>	$\nu f(\nu)$ flux at 0.5 keV from image analysis
I- $\nu f(\nu)$ @ 0.5 keV_error	D	erg cm <sup>-2</sup> s <sup>-1</sup>	error $\nu f(\nu)$ flux at 0.5 keV
I- $\nu f(\nu)$ @ 1 keV	D	erg cm <sup>-2</sup> s <sup>-1</sup>	$\nu f(\nu)$ flux at 1.0 keV from image analysis
I- $\nu f(\nu)$ @ 1 keV_error	D	erg cm <sup>-2</sup> s <sup>-1</sup>	error $\nu f(\nu)$ flux at 1.0 keV
I- $\nu f(\nu)$ @ 1.5 keV	D	erg cm <sup>-2</sup> s <sup>-1</sup>	$\nu f(\nu)$ flux at 1.5 keV from image analysis
I- $\nu f(\nu)$ @ 1.5 keV_error	D	erg cm <sup>-2</sup> s <sup>-1</sup>	error $\nu f(\nu)$ flux at 1.5 keV
I- $\nu f(\nu)$ @ 4.5 keV	D	erg cm <sup>-2</sup> s <sup>-1</sup>	$\nu f(\nu)$ flux at 4.5 keV from image analysis
I- $\nu f(\nu)$ @ 4.5 keV_error	D	erg cm <sup>-2</sup> s <sup>-1</sup>	error $\nu f(\nu)$ flux at 4.5 keV
I-Flux0510	D	erg cm <sup>-2</sup> s <sup>-1</sup>	0.5–10.0 keV flux from image analysis
I-Flux0510_error	D	erg cm <sup>-2</sup> s <sup>-1</sup>	error on 0.5–10.0 keV flux from image analysis
I-Flux210	D	erg cm <sup>-2</sup> s <sup>-1</sup>	2.0–10.0 keV flux from image analysis
I-Flux210_error	D	erg cm <sup>-2</sup> s <sup>-1</sup>	error on 2.0–10.0 keV flux from image analysis
I-Photon_index	D		power law photon index fit from hardness ratio
I-Photon_index_error	D		error on photon index for power-law fit
SED-Photon_index	D		photon index for power-law fit estimated from a fit to I- $\nu f(\nu)$ @ 0.5keV, I- $\nu f(\nu)$ @ 1.5keV and I- $\nu f(\nu)$ @ 4.5keV
SED-Photon_index_error	D		error on photon index
SED-Photon_index_error	D		error on photon index for power-law fit
CR(0.3-10 keV)	D	cts s <sup>-1</sup>	count-rate in 0.3–10.0 keV energy band
CR(0.3-10 keV)_error	D	cts s <sup>-1</sup>	error on count-rate in 0.3–10.0 keV energy band
O- $\nu f(\nu)$ @ 1 keV	D	erg cm <sup>-2</sup> s <sup>-1</sup>	overall $\nu f(\nu)$ flux at 1.0 keV for light curves
O- $\nu f(\nu)$ @ 1 keV_error	D	erg cm <sup>-2</sup> s <sup>-1</sup>	error on overall $\nu f(\nu)$ flux at 1.0 keV
Upper limit flag	2A		flag set to ‘UL’ if the count rate is a 3 $\sigma$ limit, blank otherwise

**LONG-TERM LIGHTCURVES:** 1 KeV  $\nu f(\nu)$  light curves covering the period November 2004 to the end of 2020 of all the sources in the sample can be accessed on-line at webpage<sup>13</sup>. Figure 2.9, Figure 2.10, and Figure 2.11 show examples of light curves of five representative LBL, IBL, and HBL blazars, respectively. Blue points represent fluxes averaged over the entire observation; red points correspond to single snapshots. Large luminosity variability on different amplitudes and timescales, ranging from factor of a few to over a factor 200, is present in all sources. The ratio between the maximum and minimum observed flux in each source is listed in column (5) of Table 2.1.

Light curves based on integrated XRT fluxes in the 0.5-2.0 keV, 0.3-3.0 keV, 0.5-10 keV, and 2-10 keV bands, or  $\nu f(\nu)$  fluxes at the energy of 0.5 keV, 1.5 keV, 4.5 keV, can be produced using the data provided in the fits file described in Table 2.2.

**Harder-when-brighter and softer-when-brighter** behaviour: Spectral changes correlated with intensity variations in blazars were first noticed in early EXOSAT X-ray observations of PKS2155-304 [67] and of Mrk421 [68]. A study conducted on a sample of 36 BL Lacs showed that this behaviour is a common feature of BL Lacs objects [69]. In the following we investigate these correlations in our sample, which includes all types of blazars and a much larger number of observations.

The upper panel of Figure 2.12 plots the best-fit power-law spectral index as a function of X-ray flux for the source Mrk501. A clear trend is present, with steep spectral slopes ( $\Gamma \gtrsim 2.5$ ) being observed during low flux periods and much harder ( $\Gamma \sim 1.5$ ) values during high-intensity states. This harder-when-brighter behaviour is common to the HBL sources in our sample as can also be noticed in the SEDs of Figure 2.6.

A case of the opposite (softer-when-brighter) trend is shown in the middle panel of Figure 2.12 for the case of the IBL blazar OJ287. In this intermediate  $\nu_{peak}$  situation the X-ray flux strongly increases when  $\nu_{peak}$  reaches values larger than  $\approx 10^{14.5}$  Hz and the steep tail of the synchrotron SED component enters the X-ray band. When  $\nu_{peak}$  is instead located at lower frequencies, the synchrotron component does not reach X-ray energies and the flux in the X-ray band is only due to the hard inverse Compton component.

---

<sup>13</sup> <https://openuniverse.asi.it/blazars/swift/>

The lower part of Figure 2.12 illustrates the case of the LBL object 3C 273, which shows an apparent harder-when-brighter behaviour. This is likely not due to an intrinsic hardening of the inverse Compton emission from the jet but rather to a changing mix of different components. This is because during high intensity states the flat radiation from the jet dominates the steeper X-ray emission from the accretion onto the supermassive black hole (e.g., [70]).

**Rapid variability:** Large X-ray luminosity variability on a variety of timescales in blazars is common and amply documented in the literature (e.g., [71, 72, 69, 73, 74, 75, 76, 77] and references therein). We searched for large amplitude ( $\geq 50\%$ ) variability on timescales of the order of one or a few hours by comparing the flux observed during contiguous or neighbouring snapshots, which are typically separated by one Swift orbit, or  $\sim 1.5$  hours. Large luminosity variations on these timescales are rarely observed in our sample. This may reflect the fact that this type of variations are intrinsically rare in blazars, but it could also be due to limited sampling or observing strategy, as in many cases the observations consisted of single snapshot exposures.

The list of the thirteen objects where rapid variability has been noticed is given in Table 2.3 where column 1 gives the blazar name, column 2 gives the Swift Observation ID, column 3 the time in MJD units, column 4 the time difference between the snapshots where the variability was observed, and column 5 gives the ratio between the flux measured in the last snapshot and that of the first snapshot.

## 2.5 DISCUSSION

The analysis presented in the previous sections shows that long-term large amplitude X-ray variability is present in the data of all blazars of the sample on a variety of timescales (see Table 2.1 and the lightcurves of Figure 2.9, Figure 2.10, and Figure 2.11).

No obvious periodicities or regularities can be seen from a visual inspection of the lightcurve of any object. However, these results cannot be considered an unbiased view of the long-term behaviour of blazars since X-ray sources that are frequently observed by Swift are often pointed as Target of Opportunity triggered by flaring activity discovered in other parts of the electromagnetic spectrum. Nevertheless, the results presented here provide a

Table 2.3: Blazars where flux variability was observed between consecutive or neighboring snapshots

Name (1)	ObsID (2)	Date (MJD) (3)	$\Delta T$ (Ks) (4)	$f_{t2}/f_{t1}$ (5)
1H 0323+342	00035372001	53922.8	5	2.4
1H 0323+342	00035630002	53926.6	6	1.7
1ES 0414+009	00081691001	57353.9	6	0.5
TXS 0506+056	00083368006	58031.7	5	0.3
3C 120	00037594042	56934.2	5	1.5
OJ 287	00033756119	57792.3	11	0.3
OJ 231	00031219001	54624.9	15	4.1
PKS 0548-322	00044002081	58370.9	5	0.3
Mrk 421	00030352011	53905.4	5	2.9
PG 1553+113	00031368076	57021.8	5	0.7
EXO 1811.7+3143	00013748001	59125.5	4	1.5
1ES 1959+650	00034588249	59164.9	1	1.7
PKS 2155-304	00030795001	53946.1	75	2.7
BL Lac	00034748002	57668.3	5	0.2

new rich dataset that is very useful to study the observational properties of blazars and constrain physical models in the energy and time domain. In the following we make some initial considerations on blazars properties that are not significantly affected by the selection biases of the sample.

**X-RAY EMISSION IN DIFFERENT TYPES OF BLAZARS: HBLs VS IBLs VS LBLs:** Our sample includes 24 HBL, 12 IBL, and 29 LBL blazars. The X-ray band is particularly important in the energy spectrum blazars of all types, as the X-ray flux of HBL sources is entirely due to synchrotron emission, while in IBL objects the end of the synchrotron tail often merges with the second (inverse Compton or other) high-energy component. In LBL sources the X-ray flux instead maps the beginning of the second SED bump. Different spectral shapes, variability properties, and probably also time lags between the soft and hard X-ray band, are to be expected in blazars of different types.

The location and variability properties of  $\nu_{peak}$  provide crucial information about the physical conditions in blazars jets. Among the important physical parameter that can be constrained are the maximum particles energy, the acceleration, and cooling times, the size of the emitting region, and the distribution of the particles responsible for the non-thermal

radiation that we observe. The results obtained with our large data-set on this important parameter can be summarized as follows:

- The SEDs of the 65 objects in our sample, some of which are shown in Figure 2.4, Figure 2.5, Figure 2.6, confirm with large statistics that  $\nu_{peak}$  in blazars ranges from  $\sim 10^{12}$  Hz, to well over  $10^{18}$  Hz.
- The position of  $\nu_{peak}$  is not constant in time, as noticed over twenty years ago in the BeppoSAX data of Mrk501 and 1ES2344+514 [78, 79], and more recently studied in detail in some objects (e.g., [71, 72]). Our results show that frequent and large variations of  $\nu_{peak}$ , spanning a range of well over a factor 100 in some objects, is a very common, likely ubiquitous, feature of HBLs. As an example, Figure 2.7 illustrates how frequently  $\nu_{peak}$  changes in time and amplitude in Mrk421, the blazar most frequently observed by Swift. The SEDs plotted in Figure 2.6, and those available online show that this phenomenon is present in most HBLs of the sample. Figure 2.8 shows the distribution of  $\nu_{peak}$  in four representative HBL blazars, where we can see that blazars of this type spend a significant fraction of the time with  $\nu_{peak}$  values that are more than a factor 5 away from the average value. Note that these histograms may be a partially distorted representation of the intrinsic probability distributions because of the selection biases of the sample. This is because ToO observations tend to follow large  $\nu_{peak}$  values during flares, rather than quiet periods. In addition, the relatively narrow band-pass of XRT limits the range over which  $\nu_{peak}$  can be safely estimated to  $\sim 0.5$  keV and 8-10 keV.
- Variations of  $\nu_{peak}$  in IBL sources are difficult to detect with XRT data alone since  $\nu_{peak}$  in these objects is located outside the X-ray band. Despite that, [80] combining Swift UVOT and XRT data, found evidence for  $\nu_{peak}$  variations in the IBL blazar S50716+714. Harder-when-brighter trends has been found in the infrared and optical part of the spectrum of the same object by [81] and [82], suggesting that large  $\nu_{peak}$  variations should be present in IBL blazars as well.
- Variations of the SED peak frequency in LBLs are also hard to observe because of the lack of multi-epoch observations in the far infrared, where  $\nu_{peak}$  is located in these

sources. However, at least in the cases of CTA 102, 3C 279 and 3C 454.3 (see Figure 2.4), where large intensity variations in the IR/optical/UV and X-ray band have been detected, no significant spectral changes have been detected, consistently with no evidence for a large increase of  $\nu_{peak}$  in LBLs. An optical-infrared monitoring of  $\gamma$ -ray emitting blazars of different types [83] detected a tendency for FSRQs (all of which are of the LBL type) to become bluer when fainter. This apparent hardening was interpreted as due to the blue accretion disk emission becoming increasingly dominant during faint states of the jet component. When the sources were found in a bright state the spectrum tended to become redder (steeper), implying that  $\nu_{peak}$  in these sources was not moving from the far-IR to energies close to the optical band.

- Most of the X-ray flux enhancements in HBL sources is due to the effects of spectral hardening, rather than to an overall flux increase at all energies. This effect is larger when  $\nu_{peak}$  is located in the very soft X-ray band. In this situation a small increase of this parameter flattens the X-ray spectrum inducing large flux increases. On the other hand, when  $\nu_{peak}$  reaches values that are larger than the energy band where the flux is measured, no significant flux increase is often observed. This behaviour may be due to a  $\nu_{peak}$  increase without an associated increase in the normalisation of the spectrum, or to the onset of a second hard component related to a different emitting region. This second hypothesis was first considered by [78], who interpreted the  $\nu_{peak}$  shift in 1ES2344+514 as the result of a different component emerging at high energies.

Most values of  $\nu_{peak}$  reported in the literature are estimated under one of these circumstances: (a) on the basis of a single X-ray observation, (b) based on the average value of several X-ray measurements, or (c) on sparse archival X-ray data taken at different epochs. In all cases, the value of  $\nu_{peak}$  may be biased for the following reasons: when a blazar has been observed many times, the observations are often the result of monitoring campaigns carried out in response to the announcement of a large flare or of a high state of the object. Since there is a strong correlation between source intensity and  $\nu_{peak}$  (in most cases higher  $\nu_{peak}$  when the source brightens, e.g., [71, 72]) the average flux and the corresponding  $\nu_{peak}$  will be biased towards high values. When instead a blazar has only one X-ray observation

(e.g., objects discovered in the RASS survey, [84], and never observed afterwards), the value of  $\nu_{peak}$  is a random draw from the (intrinsic, perhaps time dependent)  $\nu_{peak}$  distribution similar to those shown in Figure 2.8. If this single draw is a low value that corresponds to a flux below the X-ray sensitivity limit, the blazar is not even discovered. Those above the X-ray limit but close to it, as in many real cases, will have a value of  $\nu_{peak}$  that is biased towards high values.

Some of the so-called extreme blazars [85] might therefore not be really extreme sources, but objects that spend most of their time with moderately high  $\nu_{peak}$  values and happened to have been discovered in a high state.

**UNEXPECTED FINDINGS AND FUTURE SAMPLES:** The existence of transient blazars was not known until the detection of 4FGLJ1544.3-0649 [4], one of the objects in our sample. This object remained hidden in the archives as one of the many anonymous radio sources with no associated high-energy emission, until May 2017 when [86] reported the emergence of a new Fermi-LAT transient source, triggering observations at other frequencies. These new data led to the identification of a new blazar, which for a few months became one of the brightest objects of this type in the X-ray and  $\gamma$ -ray bands.

The unexpected existence of transient blazars could complicate or even modify our perception of this type of sources if 4FGLJ1544.3-0649 does not represent an isolated case but rather the tip of the iceberg of a previously unnoticed phenomenon. It is likely that similar sources are present in the existing archival data or will be found in future sensitive observations.

The SRG/eROSITA ([87, 88]) X-ray telescope is conducting an all-sky X-ray survey with good sensitivity, repeated at different epochs. This survey will have a deep impact on blazar science with the discovery of a few thousand new objects with multiple detections, especially of those located near the ecliptic poles, thus mitigating or largely removing the biases described above. This extremely valuable data-set, alongside the science archives of the forthcoming and previous space missions and ground based observatories, constitute a colossal, ever growing, reservoir of information. It is clear that it is not possible to efficiently convert this enormous potential into knowledge following a traditional approach based on the

analysis of low or intermediate level data from every instrument, each requiring specific expertise. Only the easily-accessible/transparent availability of science-ready data products will enable us to fully exploit the great potential of open archives, giving us, in this particular case, a much more complete view of blazars. The work performed during my PhD research aims at being a step in this direction.

## **2.6 CONCLUSION**

We have analysed the Swift XRT data taken in PC and WT modes of 65 blazars observed at least 50 times from launch in late 2004 to the end of 2020. We have processed a total of 31,068 Swift XRT observations and individual snapshots using a software pipeline called `Swift_xrtproc` that automatically retrieves the data, performs a spectral and photometric analysis, and writes the results to an archive database. This work complements and extends the results presented in [64] based on an X-ray imaging analysis of the blazars observed by Swift in PC mode. It represents another step towards the development of a multi-messenger multi-temporal high-transparency archive of blazars data products and results. We have used this unprecedented dataset to describe the general temporal and spectral behaviour of blazars of different types [69].

# 3 MULTIWAVELENGTH MONITORING OF BLAZARS PKS 2155-304 AND S5 0716+71

## 3.1 INTRODUCTION

Blazars are the dominant population of extragalactic sources in the  $\gamma$ -ray sky. The multiwavelength variability study of blazars has recently entered a new era. There is a large amount of  $\gamma$ -ray data available from continuous observations of blazars in the HE band by Fermi-LAT. Also, Neil Gehrels Swift Observatory [42] performed a large number of observations of single objects. The combination of the data from Swift observations with data from Fermi-LAT in the  $\gamma$ -ray band, will provide a unique possibility to investigate both emission components in the broadband SED of the blazars.

Now, the accumulated amount of data permits a detailed variability study in almost all the bands. Variability studies in each band are crucial to identify the timescale of flux variability which in its turns allows to constrain the size and location of the emitting region. At the same time intra-band variability studies allow to identify correlated or anti-correlated variabilities in different bands which can shed light on the physical processes responsible for multiwavelength emission from blazars. For example, the MAGIC observation of BL Lac blazar on 15 June 2015 showed a flare with a maximum flux of  $(1.5 \pm 0.3) \cdot 10^{-10}$  photon  $\text{cm}^{-2} \text{s}^{-1}$  and a halving time as short as  $26 \pm 8$  min [89]. Or in the high energy (HE  $> 100$  MeV) band, the Fermi Large Area Telescope (Fermi-LAT) observations of 3C 279 on 16 June 2015 showed a high-amplitude variability (the  $\gamma$ -ray flux was as high as  $3.6 \cdot 10^{-5}$  photon  $\text{cm}^{-2} \text{s}^{-1}$ ) when the source flux variability was resolved down to 2-minute binned timescales, with flux doubling times of less than 5 minutes [90]. Similarly, the long-term variability has been extensively investigated also in the radio-optical bands where the data collected over decades are available [91, 92].

Considering the large number of blazars observed more than 100 times by Swift (see Figure 2.1), a tool that automatically downloads and analyses data from Swift UVOT observations of blazars was developed. This allows to process a large amount of optical/UV data accumulated after the launch of Swift satellite. As an application of the tool, the data from observations of two well-known blazars, PKS 2155-304 and S5 0716+71, was reduced. Also,

the X-ray and  $\gamma$ -ray data were analysed and compared with optical/UV data allowing to investigate variability in different bands and investigate the origin of broad band emission from these sources.

### 3.2 MONITORING OF THE SOURCES IN OPTICAL/UV BANDS

The Swift satellite launched in 2004 is primarily designed for observations of  $\gamma$ -ray bursts. With the three instruments on board (UVOT, XRT and BAT) and a wide energy coverage, Swift is suitable for blazar research. The range observed by Swift defines either the low-energy component or the transition region between the two components or the rising part of the inverse Compton component (depending on the type of blazar), so that these data are particularly important for theoretical modelling.

The Swift UVOT telescope can produce images in each of six filters, namely in V (500-600 nm), B (380-500 nm), U (300-400 nm), W1 (220-400 nm), M2 (200-280 nm) and W2 (180-260 nm). In order to process UVOT data from any blazar observation, a special tool was developed. Providing the name and the coordinates of the source under interest, it accesses the Swift archive, downloads all the existing observations and processes them with the standard procedure. After cleaning and filtering the data, all single observations are reduced by selecting source counts from a circular region of 5" around the source, while selecting the background counts from a 20" region away from the source. Then with the help of `uvotsource` tool it derives the magnitudes which are converted to fluxes using the conversion factors provided by Poole et al. [93] and then corrected for extinction, using the reddening coefficient  $E(B - V)$  from the Infrared Science Archive<sup>14</sup>. The tool produces the flux measured in each filter in each period for the light curve computation as well as the flux for each frequency for SED calculations. The tool was extensively tested by analysing the data from different blazar observations and comparing with the published results. The developed tool was used to analyse all the Swift UVOT observations of PKS 2155-304 and S5 0716+71. Between 2004 - 2022, PKS 2155-304 were observed 300 times and S5 0716+71 - 352 times.

The light curve of PKS 2155-304 is shown in Figure 3.1 d and Figure 3.1 e, separating the

---

<sup>14</sup> <http://irsa.ipac.caltech.edu/applications/DUST/>

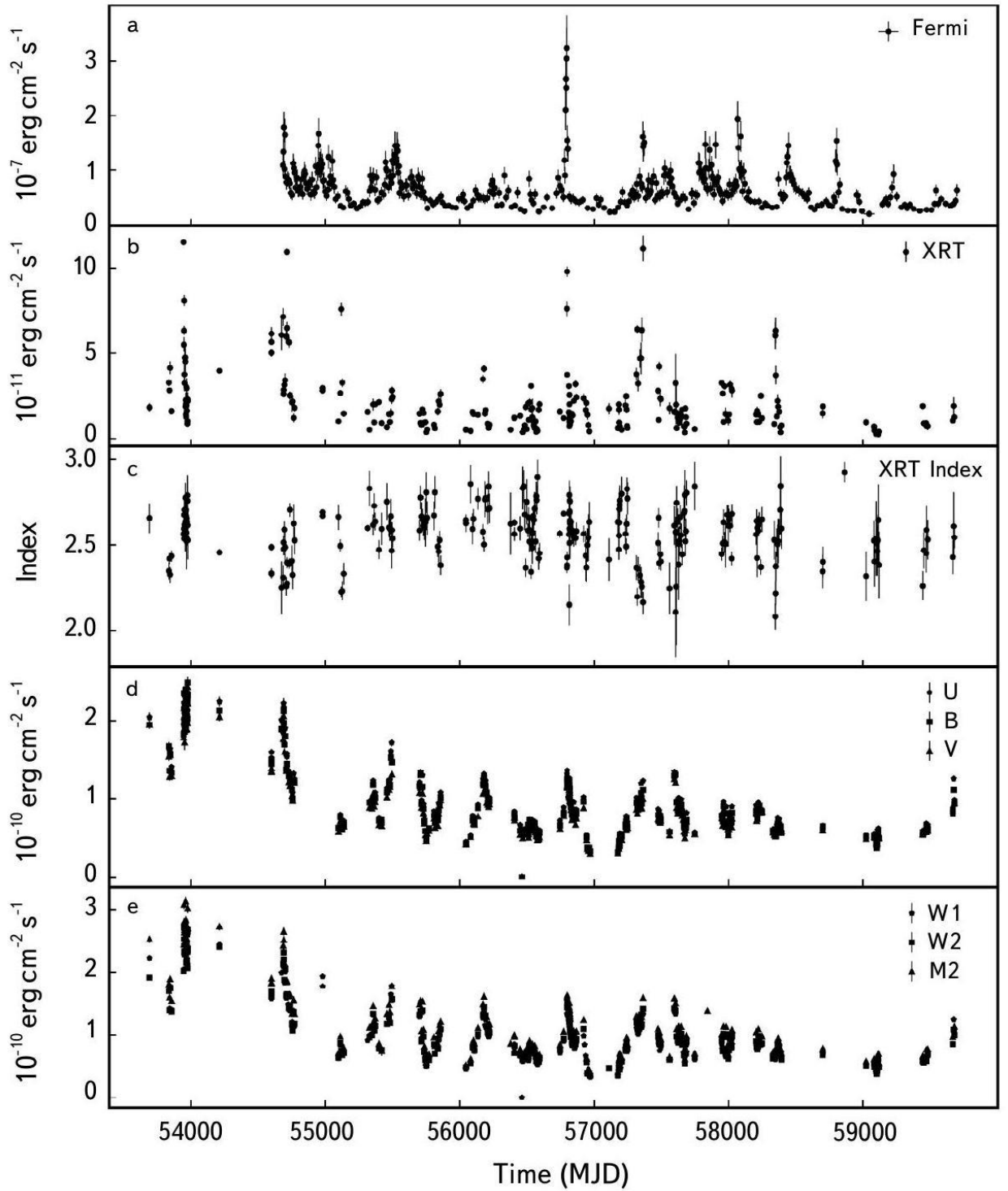


Figure 3.1: Multiwavelength light curve of PKS 2155-304. a) Adaptively binned  $\gamma$ -ray light curve above MeV. b) X-ray flux estimated in 2.0-10 keV band. c) X-ray photon index. d) Flux in U, B and V bands. e) Flux in W1, W2, and M2 bands.

flux in V, B, U and W1, M2 and W2 filters. It shows that during the initial observations (e.g., until MJD 55000) the source was in an evaluated emission state in all the considered bands.

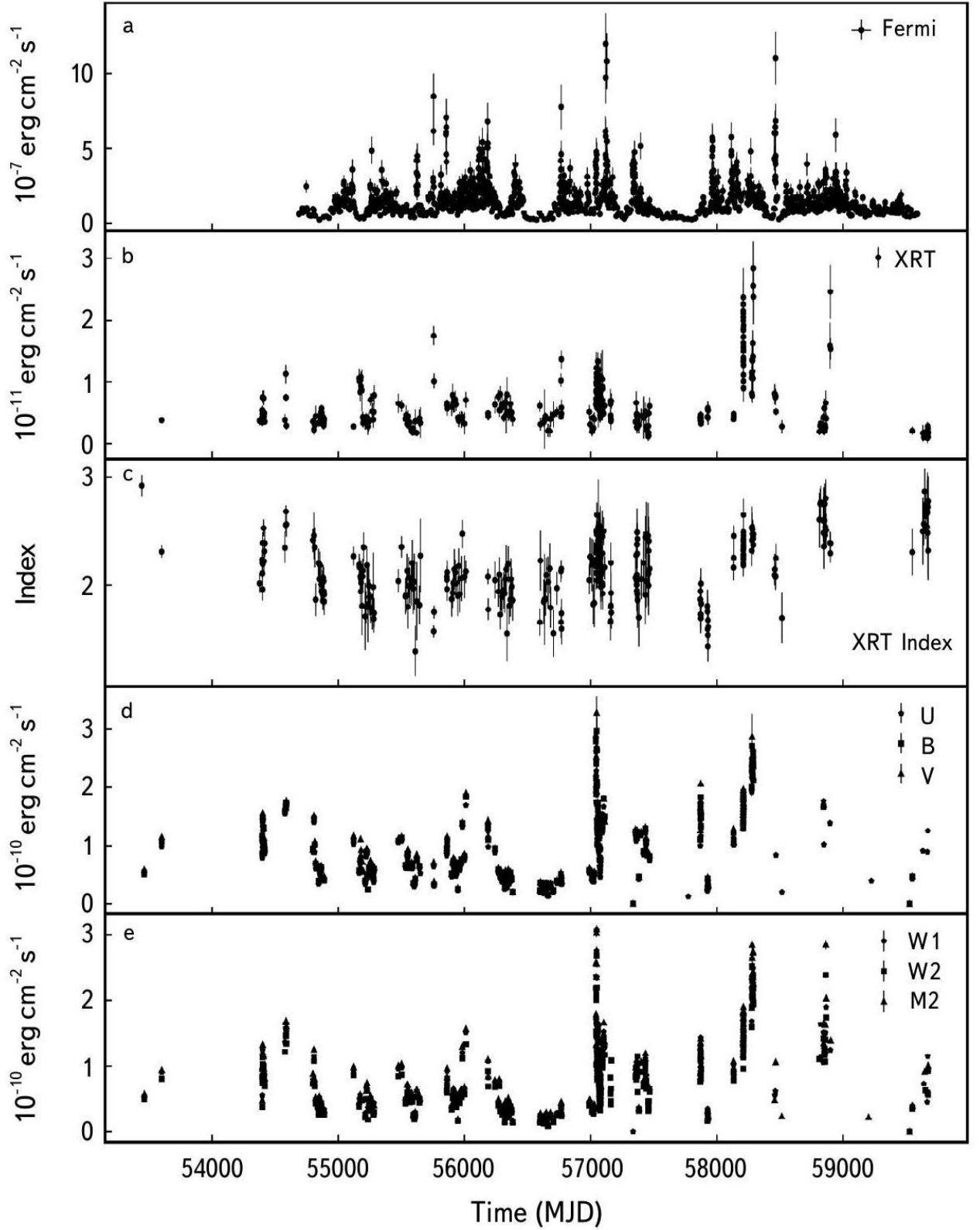


Figure 3.2: The multiwavelength light curve of S5 0716+71 between 04/08/2008-04/05/2022. From top to bottom: adaptively binned  $\gamma$ -ray light curve ( $> 202.65$  MeV), 2.0-10 keV X-ray flux, 0.3-10 keV X-ray photon index, flux in V, B, and U filters and in W1, M2 and W2 filters.

For example, in this period the highest flux of the source was  $(3.12 \pm 0.07) \times 10^{-10}$  erg

$\text{cm}^{-2} \text{s}^{-1}$  observed on MJD 53960.85 in filter M2. Then the averaged level of source emission in optical/UV bands decreases, but a few times flux variations in all the considered filters are still evident. For example, the flux in M2 band on MJD 56046.13 was  $(5.1 \pm 0.11) \times 10^{-11} \text{ erg cm}^{-2} \text{ s}^{-1}$  which increased to  $(1.60 \pm 0.03) \times 10^{-10} \text{ erg cm}^{-2} \text{ s}^{-1}$  on MJD 56180.67. Such changes in consecutive UVOT observations can be identified during all the considered periods, which show that this source has a strongly variable optical/UV emission.

In Figure 3.2 d and Figure 3.2 e, S5 0716+71 light curve in V, B, U and W1, M2 and W2 filters is shown. Two large flaring activities in optical and UV bands are evident. The first active period was observed between MJD 57030-57060 when the flux in almost all filters increased from  $\sim 5 \times 10^{-11} \text{ erg cm}^{-2} \text{ s}^{-1}$  to above  $\sim 2 \times 10^{-10} \text{ erg cm}^{-2} \text{ s}^{-1}$ . In this period, the highest flux of  $(3.28 \pm 0.09) \times 10^{-10} \text{ erg cm}^{-2} \text{ s}^{-1}$  was observed in filter V on MJD 57047.31. The next major flaring activity was observed between MJD 58200-58300 when the flux again increased above  $\sim 2 \times 10^{-10} \text{ erg cm}^{-2} \text{ s}^{-1}$ . This source is characterized by variable optical/UV emission, i.e., the flux changes in different Swift observations. Only between MJD 56600-56800 the source was in a relatively quiescent state in the optical/UV bands: during this period, in 14 *Swift* observations the flux was relatively constant with a value of  $\sim 2 \times 10^{-11} \text{ erg cm}^{-2} \text{ s}^{-1}$ .

### 3.3 X-RAY OBSERVATIONS OF PKS 2155-304 AND S5 0716+71

Simultaneously with the optical/UV observations, the sources were observed also in the X-ray band with the Swift XRT instrument. For both sources all the data were downloaded from SSDC archive<sup>15</sup> and processed using `Swift_xrtproc` automatic tool for XRT data analysis [94]. The raw data (Level1) were downloaded, reduced, calibrated and cleaned via the `XRTPIPELINE` script by applying the standard filtering criteria and the latest calibration files of CALDB. The counts were extracted from a circular region of a radius of  $\sim 20$  pixels (47") centered on the source's position, while the background counts are taken from an annular ring centered at the sources. The tool automatically applies also pile-up correction when the sources' count rate was above  $0.5 \text{ count s}^{-1}$ . Then it loads the ungrouped data in XSPEC

---

<sup>15</sup> <https://www.ssdsc.asi.it>

(version 12.11) for spectral fitting using Cash statistics [62], modelling the source spectrum as a power-law and a log-parabola model taking the Galactic absorption column density from  $N_H$  HEASARC tool<sup>16</sup> [95, 96, 97].

The X-ray flux and photon index variation of PKS 2155-304 are shown in Fig. 4.1b and 4.1c. In the X-ray band, there are several observations when the flux in the 2.0-10 keV band substantially increased. In the low (average) state the flux is around  $(0.2 - 1.0) \times 10^{-11} \text{ erg cm}^{-2} \text{ s}^{-1}$  while in the flaring state it increases to  $> 10^{-10} \text{ erg cm}^{-2} \text{ s}^{-1}$  (e.g., in observations on MJD 53945.04, 54714.16, 57363.93). The X-ray photon index varies in time as well, on average the source is characterized with a soft photon index ( $\Gamma_X \approx 2.5$ ) but from time to time it hardens ( $\Gamma_X < 2.5$ ). It is interesting to note that around the flares on MJD 57363.93 and MJD 58350.03 when the X-ray flux increased correspondingly to  $(1.11 \pm 0.07) \times 10^{-11} \text{ erg cm}^{-2} \text{ s}^{-1}$  and  $(6.32 \pm 0.74) \times 10^{-11} \text{ erg cm}^{-2} \text{ s}^{-1}$ , the X-ray photon index was  $\Gamma_X = 2.16 \pm 0.06$  and  $\Gamma_X = 2.21 \pm 0.07$ , respectively. This is unusual for PKS 2155-304 and it most likely corresponds to the transition region between the synchrotron and inverse Compton components.

In the X-ray band, S5 0716+71 shows several flaring periods as well. There can be identified at least three large flaring activities in Figure 3.2 b: the first two between MJD 58140-58460 and the third one around MJD 58900 (in several other periods the X-ray flux increases as well but with smaller amplitudes). The highest flux of the source  $(2.84 \pm 0.45) \times 10^{-11} \text{ erg cm}^{-2} \text{ s}^{-1}$  was observed on MJD 58288.68 which 11.36 times exceeds the X-ray flux in the average/low state ( $\sim 2.5 \cdot 10^{-12} \text{ erg cm}^{-2} \text{ s}^{-1}$ ). The photon index variation is evident from Figure 3.2, it varies around  $\Gamma_X = 2.0$ , sometimes showing harder spectra ( $\Gamma_X < 2.0$ ) but sometimes also soft spectra were observed ( $\Gamma_X > 2.2$ ). The softest index of  $\Gamma_X = 2.86 \pm 0.2$  was observed on MJD 59646.43 while the hardest one was  $\Gamma_X = 0.96 \pm 0.66$  observed on MJD 55608.93.

### 3.4 GAMMA-RAY OBSERVATIONS AND DATA ANALYSIS

Fermi-LAT on board the Fermi Gamma-ray Space Telescope is a pair-conversion telescope

---

<sup>16</sup> <https://heasarc.gsfc.nasa.gov/cgi-bin/Tools/w3nh/w3nh.pl>

sensitive to  $\gamma$ -rays in the energy band from 20 MeV to 500 GeV. By default, being in the scanning mode, it observes the entire sky every  $\sim 3$  hours, providing a continuous view of the  $\gamma$ -ray emission from Galactic and extragalactic sources. The details on the Fermi-LAT instrument are given in [98].

For the study of  $\gamma$ -ray properties of PKS 2155-304 and S5 0716+71 the Fermi-LAT data accumulated during 2008-2022 (MET 239557417-673371821) from the observations of these sources are considered. The data were processed with the standard Fermi ScienceTools version 1.2.1. The Pass 8 (P8R3) Fermi-LAT events with a higher probability of being photons (evclass = 128, evtype = 3) were analysed using the P8R3\_SOURCE\_V3 instrument response function. The events in the energy range from 100 MeV to 500 GeV were downloaded from a  $12^\circ$  region centered on the  $\gamma$ -ray position of PKS 2155-304 (RA=329.71 and Dec=-30.22) and S5 0716+71 (RA=110.49 and Dec=71.34). With gtselect tool A zenith angle cut smaller than  $90^\circ$  is applied to reduce contamination by photons from Earth's atmosphere while the good time intervals are selected with gtmktime tool using the filter expression (DATA\_QUAL > 0) and (LAT\_CONFIG == 1). With gtbin tool the photons are binned into  $16.9^\circ \times 16.9^\circ$  square region into pixels of  $0.1^\circ \times 0.1^\circ$  and into 37 equal logarithmically spaced energy bins. Then, with the help of gtlike tool, a standard binned maximum likelihood analysis is performed. The fitting model includes diffuse and isotropic backgrounds, which were modelled with standard gll\_iem\_v07 and iso\_P8R3\_SOURCE\_V3\_v1 models and  $\gamma$ -ray sources within the region of interest. The model was created using the Fermi-LAT fourth source catalog Data Release 3 (4FGL-DR3) [99] where all sources within  $17^\circ$  around the target are included. The spectral parameters of the background sources which are between  $12^\circ$  and  $12^\circ + 5^\circ$  were fixed to their catalog values, while the normalization and spectral parameters of the other sources were left free.

After optimizing the free parameters in the model, the source variability is investigated by estimating the flux (light curve) in shorter intervals by applying unbinned likelihood analysis. The light curve was calculated with the help of an adaptive binning method. When calculating the light curve with fixed time bins (e.g., a day or several days), the long bins will smooth out the fast variation, whereas the short bins might instead result in many upper limits, preventing

the variability studies. In the adaptive binning method, the bin width is adjusted by requiring a constant relative flux uncertainty, which produces longer time intervals during lower flux levels and narrower bins when the source is in a high state. This method has been proven to be very efficient in identifying flaring activities [100, 101, 102, 103, 104, 105].

The light curve of PKS 2155-304 computed above the optimal energy of 274.38 MeV is shown in Figure 3.1 a. It shows that in several occasions the source flux increased several times (3-5 times), but the major  $\gamma$ -ray flare was observed between MJD 56770-56800 when within 37 days the flux increased from  $(5.08 \pm 0.9) \cdot 10^{-8} \text{ photon cm}^{-2} \text{ s}^{-1}$  to  $(3.24 \pm 0.59) \cdot 10^{-7} \text{ photon cm}^{-2} \text{ s}^{-1}$ . The highest flux of  $(3.24 \pm 0.59) \cdot 10^{-7} \text{ photon cm}^{-2} \text{ s}^{-1}$  above 274.38 MeV was observed on MJD 56795 within 15.86 minutes which is the highest  $\gamma$ -ray flux of PKS 2155-304 since the launch of Fermi-LAT. It is interesting that during this flaring event also the photon index hardened, namely when the high fluxes of  $(3.24 \pm 0.59) \cdot 10^{-7} \text{ photon cm}^{-2} \text{ s}^{-1}$  and  $(3.04 \pm 0.56) \cdot 10^{-7} \text{ photon cm}^{-2} \text{ s}^{-1}$  were observed on MJD 56795 and 56794, respectively, the  $\gamma$ -ray photon index was  $1.64 \pm 0.12$  and  $1.53 \pm 0.11$ , respectively. It shows that during this flare the  $\gamma$ -ray spectrum hardens, shifting the peak to higher energies.

A similar adaptive light curve of S5 0716+71 computed above 202.65 MeV is shown in Figure 3.2 a. As compared with PKS 2155-304, this source shows several prolonged  $\gamma$ -ray flaring periods. The  $\gamma$ -ray flux of sources in the low states (e.g., between MJD 57570-57840) is around  $\sim 3 \cdot 10^{-8} \text{ photon cm}^{-2} \text{ s}^{-1}$ . The maximum  $\gamma$ -ray flux of  $(2.0 \pm 0.2) \cdot 10^{-6} \text{ photon cm}^{-2} \text{ s}^{-1}$  was observed on MJD 57118.61 which exceeds the flux at low states by nearly 66 times. The mean photon index in the  $\gamma$ -ray band is  $\Gamma_{mean} = 2.05$  which corresponds to a flat spectrum in  $\nu F_\nu$  representation, but a hard index of  $\Gamma_\gamma = 1.59 \pm 0.10$  was occasionally observed on MJD 56079 and a soft index of  $\Gamma_\gamma = 2.63 \pm 0.23$  was observed on MJD 59356.1. In total, during nearly fourteen years of observations of S5 0716+71, there are 16 periods when the  $\gamma$ -ray photon index was  $\Gamma_\gamma < 1.7$ .

### 3.5 RESULTS AND INTERPRETATION

The multiwavelength data collected from blazar observations is the key to the understanding of the origin of the complex processes taking place in relativistic jets. For this

aim, the multiwavelength emission from two blazars, PKS 2155-304 and S5 0716+71, was comprehensively investigated by analysing the Swift UVOT, Swift XRT and Fermi-LAT data accumulated in the past fourteen years. PKS 2155-304 at a redshift of  $z = 0.116$  is one of the brightest HBL type objects in the Southern Hemisphere. It is an object very luminous in the UV to VHE  $\gamma$ -ray bands and has an almost featureless continuum from radio to X-ray energies as in most of the other BL Lac objects. Its multiwavelength emission observed for already more than 40 years is strongly variable in almost all bands. In radio bands, this source was discovered as part of the Parkes survey [106] and was discovered as an X-ray source by the HEAO 1 X-ray satellite [107]. In the  $\gamma$ -ray band, the source was initially observed by EGRET [108] and it was one of the first blazars observed in the VHE  $\gamma$ -ray band [109]. S5 0716+71 with a redshift of  $z = 0.31 \pm 0.08$  [110] is another well-studied BL lac bright in all bands. It shows extreme variability (e.g., in the X-ray band) and a prominent jet component, and it is a strong  $\gamma$ -ray source. The long-term monitoring of S5 0716+71 in the radio and optical bands reveals the presence of quasi-periods. The optical data accumulated during 1994-2001 indicated a period of about 3.3 years. Instead, the radio data at frequencies from 4.8 to 36.8 GHz indicate the presence of a period of 8 years [111]. The MAGIC observations in the VHE  $\gamma$ -ray band show that this source underwent an impressive outburst in January 2015 (Phase A), followed by minor activity in February (Phase B) [112]. During this flaring period the source flux increased from  $(4.1 \pm 1.1) \cdot 10^{-11} \text{ cm}^{-2} \text{ s}^{-1}$  to  $(8.9 \pm 1.1) \cdot 10^{-11} \text{ cm}^{-2} \text{ s}^{-1}$  above 150 GeV.

**PHOTON INDEX VERSUS FLUX VARIATION:** The data available in the X-ray and  $\gamma$ -ray bands allow to investigate the variation of the flux as compared with the photon index. The spectral evolution observed in the photon-index-flux plane contains important information about the dynamics of the source and provides an insight into the processes responsible for the particle acceleration and cooling. As it has been shown in Kirk et al. [113], depending on the relation between the variability, acceleration and cooling timescales, a harder-when-brighter or softer-when-brighter trend will be observed in the photon index versus the flux plane. The  $\gamma$ -ray photon index of PKS 2155-304 versus the photon index is shown in Figure 3.3 a, b, considering the entire period of Fermi-LAT observations and selecting only the

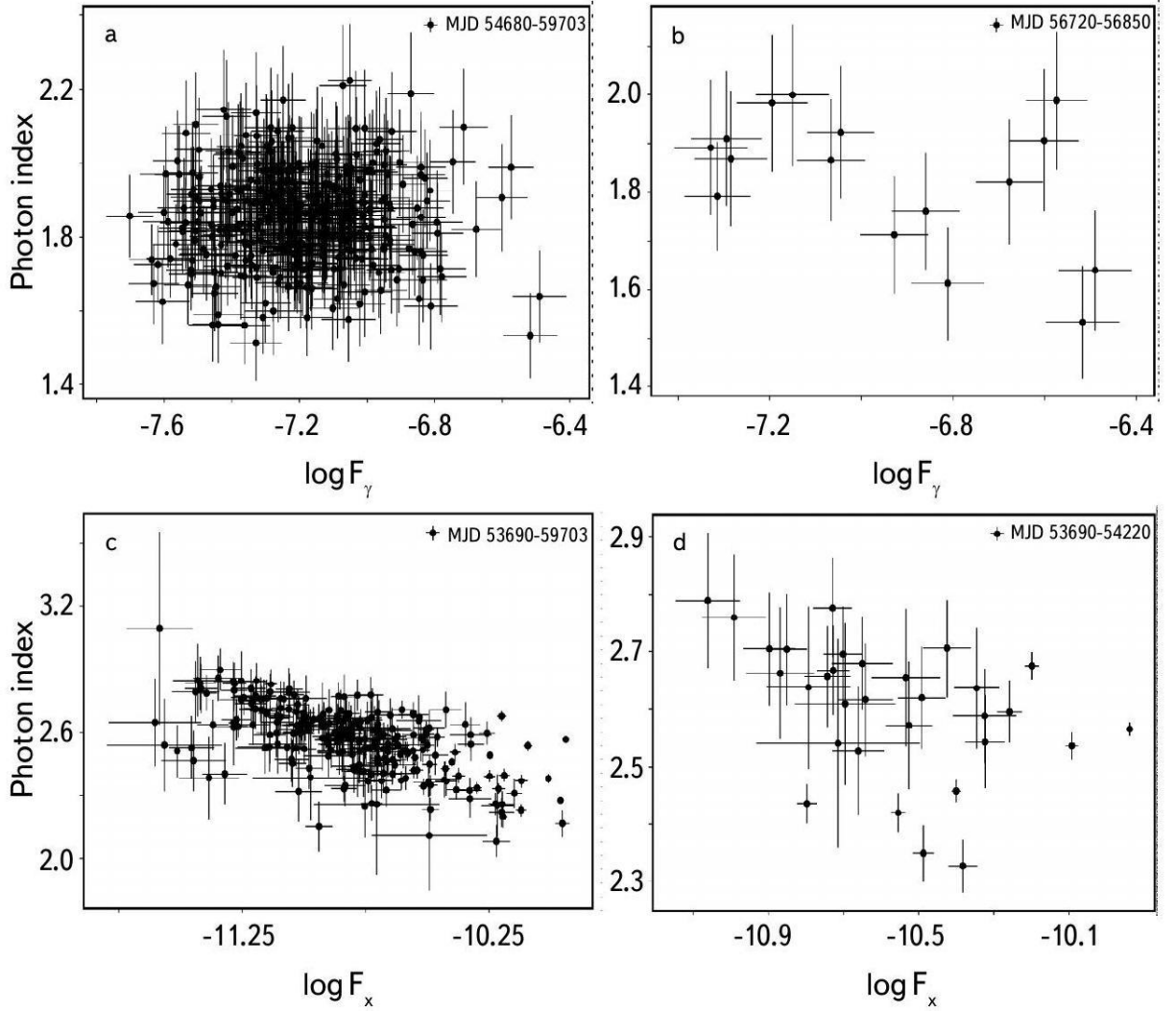


Figure 3.3: PKS 2155-304  $\gamma$ -ray flux versus photon index variation during the whole considered period (a) and during the flare between MJD 56720-56850 (b). PKS 2155-304 X-ray flux and photon index variation for all Swift XRT observations (c) and during the flare between MJD 53690-54220 (d).

period around the large flare (between MJD 56720-56850). When the entire observational period is considered with diverse properties (Figure 3.3 b), it is hard to see any trend. In fact, applying linear-Pearson correlation test yields  $r_p = 0.02$  and  $p = 0.71$ . Similar values estimated for the flaring period yields  $r_p = 0.35$  and  $p = 0.36$ . This shows that there is no correlation between the flux and photon index, i.e., the flux and photon index are independent. On the contrary, when considering all Swift XRT observations (Figure 3.3 c), there is a clear indication of the harder when brighter trend. The linear-Pearson correlation test results in  $r_p = -0.55$  and  $p \ll 10^{-5}$  which shows a negative correlation between the flux and photon index, i.e., as the flux increases, the photon index decreases (hardens). Such a relation between the flux and photon index is expected when the accelerated HE electrons

are cooling down, Kirk et al. [113]. When considering only the flaring period (Figure 3.3 d), although there is a hint of a harder-when-brighter trend, the data are not enough for a statistically significant claim ( $r_p = -0.28$  and  $p = 0.12$ ).

The blazar S5 0716+71 shows different flaring activities as compared with PKS 2155-304. Although there are large flaring activities in the X-ray band (MJD 58130-58460), no significant correlation between the flux and photon index is observed (Figure 3.4 c, d). There is a hint of harder-when-brighter trend during the X-ray flaring period (Figure 3.4 d) but the linear-Pearson correlation test yields  $r_p = -0.22$  and  $p = 0.13$ . Instead, in the  $\gamma$ -ray band, for the entire and flaring periods,  $r_p = 0.25$  and  $p \ll 10^{-5}$  and  $r_p = 0.27$  and  $p = 7.4 \cdot 10^{-5}$ ,

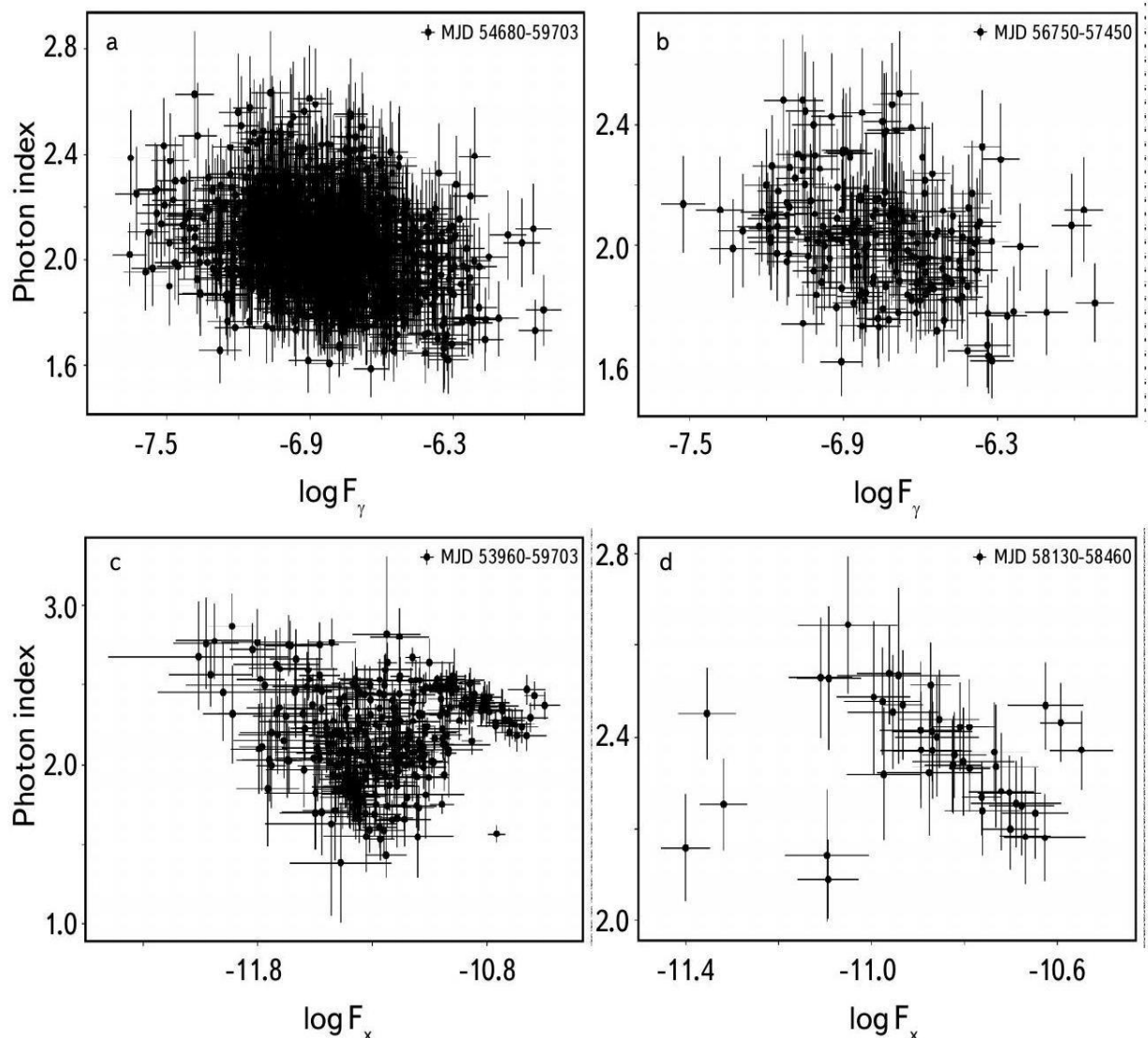


Figure 3.4: The variation of S5 0716+71  $\gamma$ -ray flux versus photon index for the entire period (a) and flaring period during MJD 56750-57450 (b). Swift XRT measured photon index flux variation for all Swift XRT observations (c) and during the flare between MJD 58130-58460 (d).

Table 3.1: Results of the correlation study between the emission in different bands.

Band-1	Band-2	PKS 2155-304		S5 0716+71	
		Spearman coeff.	$p$ -value	Spearman coeff.	$p$ -value
Optical	X-ray	0.6	$1.3e - 22$	0.7	$3e - 44$
UV	X-ray	0.6	$3.5e - 30$	0.7	$1.3e - 46$
Optical	$\gamma$ -ray	0.7	$5.4e - 18$	0.6	$4.8e - 18$
UV	$\gamma$ -ray	0.8	$3.6e - 19$	0.7	$1.3e - 18$
X-ray	$\gamma$ -ray	0.5	$6.1e - 8$	0.5	$2.4e - 12$

respectively, which show moderate softer-when-brighter trend. This shows that when the flux increases, the photon index softens. Such photon index variation is not very common for blazars but has been occasionally observed (e.g., [94, 114, 115, 116]). This shows that the PKS 2155-304 and S5 0716+71 flares observed in the X-ray and  $\gamma$ -ray bands are different by their nature and are caused by different processes.

**CORRELATION STUDIES:** As the multiwavelength light curves in Figure 3.1 and Figure 3.2 shows, there seem to be contemporaneous changes in the flux in different bands. In order to test whether or not the emission in different bands is varying contemporaneously, i.e., whether the emission in different bands is related, a Spearman correlation test was applied. The possible correlation was investigated by computing the correlation rank between the emission in different bands, i.e., computing Spearman correlation coefficient  $\rho$ . In order to perform an as general as possible test, the correlation between the emission in the X-ray and  $\gamma$ -ray bands, X-ray and optical/UV bands,  $\gamma$ -ray and optical/UV bands was investigated. When comparing the  $\gamma$ -ray flux with the other bands, the  $\gamma$ -ray periods computed by the adaptive binning method can contain several Swift observations. In this case, the mean of all observations is considered, but a check that the mean value does not significantly differ from the individual estimates in that bin was performed.

The results from the Spearman correlation analysis are given in Table 3.1 for each two bands providing the coefficient and probability. The results reported in Table 3.1 show that the null hypothesis that there is no correlation can be rejected in all cases. However, there is no strong correlation between the emissions in different bands. The correlation between the

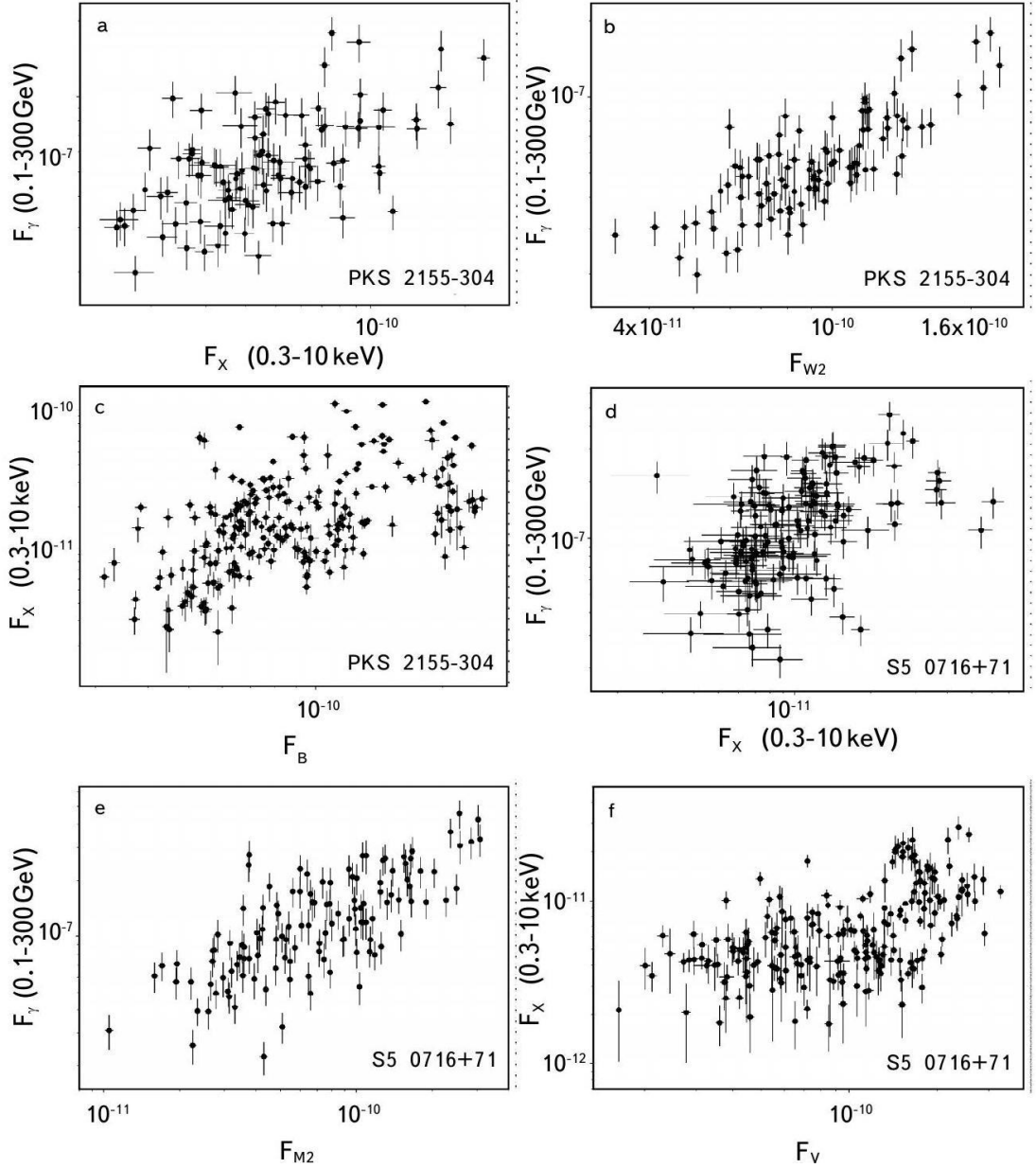


Figure 3.5: The scatter plot of the flux in different bands.

X-ray and  $\gamma$ -ray fluxes of PKS 2155-304 is shown in Figure 3.5 a. There is a weak correlation in these two bands with  $\rho = 0.5$ . For example, when the highest X-ray flux of  $(2.29 \pm 0.1) \times 10^{-10} \text{ erg cm}^{-2} \text{ s}^{-1}$  was observed, the source was bright in the  $\gamma$ -ray band with a flux of  $(1.43 \pm 0.27) \times 10^{-7} \text{ photon cm}^{-2} \text{ s}^{-1}$ . For PKS 2155-304, the strongest correlation is found for UV and  $\gamma$ -ray bands,  $\rho = 0.8$  (Figure 3.5 b). There is also a milder correlation between the source emission in X-ray and optical bands with  $\rho = 0.6$  (Figure 3.5 c).

For S5 0716+71, there is again a weak correlation between the emission in the X-ray and  $\gamma$ -ray bands with  $\rho = 0.5$  (Figure 3.5 d). This is because the emission in the X-ray band corresponds to the highest tail of the synchrotron emission, while the emission in the  $\gamma$ -ray

band corresponds to the peak of the inverse Compton component. Since the emission comes from electrons of different energy, it is natural to expect a time lag between the emission in these two bands. For this source, the correlation is almost at the same level for the optical/UV vs X-ray and optical/UV vs  $\gamma$ -ray bands (Figure 3.5 e and f)).

**MULTIWAVELENGTH SEDS:** The available data allows to investigate the broadband spectrum of both sources from radio to VHE  $\gamma$ -ray bands. The variability observed in different bands allows to build the SEDs in different periods and thus to investigate the variability in the energy domain as well. The archival data for both sources were downloaded from SSCDC science data archive<sup>17</sup> and are plotted together with the analysed data of PKS 2155-304 and S5 0716+71 (optical/UV, X-ray and  $\gamma$ -ray bands).

The multiwavelength SED of PKS 2155-304 is shown in Figure 3.6 a. The archival data are shown in grey and the optical/UV, X-ray and  $\gamma$ -ray data observed during the multiwavelength flare of the source during MJD 56714-56903 are in black color. On the average state the peak of the synchrotron component is at  $\sim 10^{16}$  Hz which does not change during the optical/UV flare of the source. It is interesting that the optical/UV flux has increased by a factor of nearly 10, but the peak of the synchrotron component is unchanged. The variability in the X-ray band is even at higher amplitudes, and the historical X-ray flux changes by a factor of 100. The same high amplitude variability can be seen also in the HE  $\gamma$ -ray band. When comparing the flux in the HE and VHE  $\gamma$ -ray bands it is necessary to take into account the strong absorption of GeV/TeV photons through interaction with extragalactic background light (EBL) photons. This means that the rising shape in the MeV/GeV band, which implies that the peak of the inverse Compton component is around  $\sim 10^{26} - 10^{27}$  Hz, will exponentially decrease at higher energies, being in agreement with the observed GeV/TeV data.

In the optical/UV band, the variability of S5 0716+71 (Figure 3.6 b) is even more extreme when the lowest and highest fluxes differ almost by a factor of 100. In this case, the optical/UV data with a decreasing shape are defining the decay of the synchrotron component, while for PKS 2155-304 these data correspond to the rising part of the synchrotron component. For

---

<sup>17</sup> <https://www.ssdsc.asi.it>

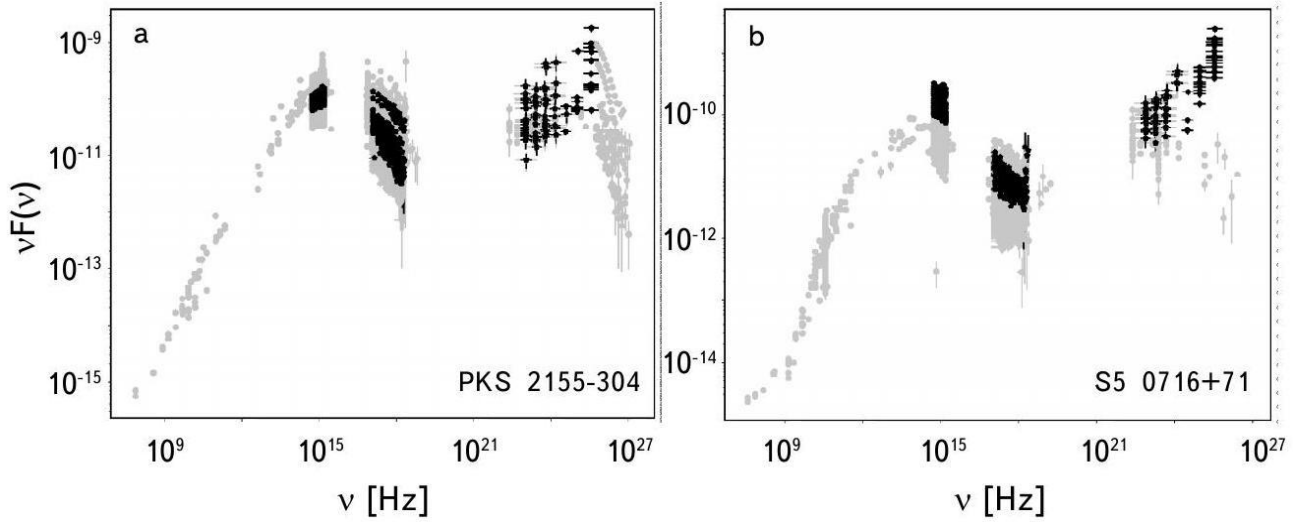


Figure 3.6: The multiwavelength SEDs of PKS 2155-304 (a) and S5 0716+71 (b) during the considered period. S5 0716+71, also a high amplitude variability is observed in the X-ray and  $\gamma$ -ray bands. Given the large red shift of S5 0716+71, the EBL absorption is even stronger for this source, which can explain the large difference between the Fermi spectrum (although not contemporaneous) and MAGIC measurements (three VHE  $\gamma$ -ray points).

The SEDs of PKS 2155-304 and S5 0716+71 can be modelled by synchrotron/synchrotron self-Compton (SSC) model [8, 7]. In this scenario, the energetic electrons confined in a compact emitting region in a randomly oriented magnetic field emit via synchrotron radiation which explains the first peak in the SED while the second peak is due to inverse Compton scattering of the same synchrotron photons. The observed flux increase in the optical/UV bands can be either due to variations in the injected plasma (particles) or due to the change of the magnetic field, as the synchrotron luminosity depends on the product of  $N_e$  (distribution of electrons) and  $B^2$ . If there is an injection of new electrons in the emitting region (e.g., due to re-acceleration) or the magnetic field increases in the emitting region (e.g., due to the change of particle density), the synchrotron luminosity will increase, appearing as a flare in the radio-optical/UV-X-ray bands. Moreover, in this interpretation the available X-ray data can be used to limit the maximum energy of accelerated particles.

The difference in the variability in the optical/UV and X-ray bands can be naturally explained by a simple consideration of particle acceleration and cooling. The X-ray emission is produced from highest energy electrons which have shorter cooling time (the electron cooling time is inverse proportional to the electron energy,  $t_{cool} \sim 1/E_e$ ), while in the same

magnetic field the optical/UV emission is from electrons that have lower energy and thus a longer cooling time. So, when there are new electrons injected in the emitting region, the emission in the X-ray band will vary with an amplitude higher than is seen in Figure 3.6.

### 3.6 SUMMARY

The results of the PKS 2155-304 and S5 0716+71 observations in the UV/optical, X-ray and  $\gamma$ -ray bands are reported. The multiwavelength monitoring of blazars is a unique tool to infer the physical processes dominating in the relativistic jets. These two blazars show prominent flares in the optical/UV bands, but it is shown that the flux substantially varies also in other bands. With the increase of the X-ray flux of PKS 2155-304, the photon index hardens, showing a harder-when-brighter trend. Instead, a moderate softer-when-brighter trend is observed in the  $\gamma$ -ray band for S5 0716+71. Generally, both sources show high-amplitude flares in the  $\gamma$ -ray band; the maximum  $\gamma$ -ray luminosity of PKS 2155-304 is  $L_\gamma = 1.35 \times 10^{47} \text{ erg s}^{-1}$  while it is  $L_\gamma = 2.13 \times 10^{48} \text{ erg s}^{-1}$  for S5 0716+71.

The correlation analysis shows that there is a strong correlation for PKS 2155-304 emission in the UV and  $\gamma$ -ray bands with Spearman coefficient of  $\rho = 0.8$ . This suggests a common origin of the emission in these bands, i.e., the emission in these bands is produced by the same electrons. In particular, most likely the UV emission comes from the synchrotron emission from the same electrons that are emitting also in the  $\gamma$ -ray band. This interpretation is even stronger when considering that UV emission defines the rising part of the synchrotron spectrum, as the  $\gamma$ -ray band corresponds to the rising part of the SSC component. In the case of S5 0716+71, as the synchrotron component peaks at lower frequencies, the optical/UV and X-ray bands are defining the high-energy tail of the synchrotron component, so these bands are not correlated with the  $\gamma$ -ray band which again corresponds to the rising part of the SSC component. Instead, as expected, the correlation between the optical/UV and X-ray bands is stronger with  $\rho = 0.8$ .

The data analysed by the tool for all the sources are available on the website<sup>18</sup> for public use.

---

<sup>18</sup> <https://github.com/DavidIsrayelyan/Swift-UVOT-Database>

# 4 LONG-TERM MULTIWAVELENGTH STUDY OF BLAZAR CTA 102

## 4.1 INTRODUCTION

CTA 102 is a FSRQ with a redshift of  $z = 1.037$  [117]. Harboursing a black hole with a mass of  $8.5 \times 10^8 M_{\odot}$  [118], CTA 102 is one of the brightest FSRQs observed in the HE  $\gamma$ -ray band. It was initially observed by the Compton Gamma Ray Observatory mission having estimated a  $\gamma$  ray flux of  $(2.4 \pm 0.5) \times 10^{-7}$  photon  $\text{cm}^{-2} \text{s}^{-1}$  [119]. Then, CTA 102 was scanned continuously by the Fermi Large Area Telescope (Fermi-LAT) since mid-2008, initially showing that the source is relatively weak in the  $\gamma$ -ray band. However, from 2016 to 2017 it underwent an unprecedented outburst in all the wavebands [86, 120, 121, 122, 123, 124, 125, 126, 127, 128]. For example, in the  $\gamma$ -ray band its flux was as high as  $(3.55 \pm 0.55) \times 10^{-5}$  photon  $\text{cm}^{-2} \text{s}^{-1}$  [100] and in some active  $\gamma$ -ray periods its spectrum also deviated from simple power-law model [5]. During the  $\gamma$ -ray flares, the source was so bright that variability was investigated down to minute scales [129]. In December 2016, the source was also in an extreme optical and near-IR out-bursting state when the brightness increased up to six magnitudes with respect to the faint state of the source [130]. Various theoretical models were used to explain the flaring behaviour of CTA 102 which includes an inhomogeneous curved jet with different jet regions changing their orientation and consequently the Doppler factors [130], or a superluminal component crossing a recollimation shock [131], or lepto-hadronic processes when the gas cloud penetrates the jet [132, 133] or the activities were interpreted as change of the location of the emission region (e.g., [100, 5, 134]), etc.

Due to the long-lasting and peculiar multiwavelength flaring activity, CTA 102 was frequently observed in different bands and became one of the most-studied blazars [135, 136, 137, 138, 139, 140, 141, 142, 143]. Although many studies have been conducted which lead to a better understanding of the CTA 102 jet, it is up to now not clear the origin of the multiwavelength flares of CTA 102, especially the changes in the jet that have led to prolonged flaring activities.

The monitoring of CTA 102 during its unprecedented outburst with various instruments resulted in accumulation of an extensive data set. In addition, before and after the outburst the source was also monitored in the  $\gamma$ -ray band with Fermi-LAT and observed in the

optical/UV and X-ray bands by Neil Gehrels Swift Observatory [42], (hereafter Swift). This can be combined with other available data to build the broadband SEDs of CTA 102 in various (flaring or quiescent) periods with (quasi) contemporaneous data. These SEDs with various spectral properties represent an ample variety of source emission in different states and their modelling is crucial for understanding of the physical processes and their changes in time. In the broadband SEDs of blazars the changes are expected to be due to the variation of the parameters of the emitting electrons or the physical parameters of the emission region. Therefore, the modelling of the SEDs in different periods allows to connect the observational properties with the physical processes at work in jets. For example, in [144] and [114] the modelling of a large number of contemporaneous SEDs of 3C 454.3 and BL Lac allowed to estimate the main parameters describing the emitting electrons and the emission region and investigate their evolution in time which was crucial for understanding of the observed spectral changes in them.

Motivated by the availability of multiwavelength data from CTA 102 observations before, during and after the large outburst, for furthering our knowledge of the emission processes dominating in the jet of CTA 102 we performed an intense broadband study of CTA 102 using the data accumulated during 2008-2022. We have systematically investigated the spectral and variability properties of the source emission in the optical/UV, X-ray and  $\gamma$ -ray bands. We performed a deep investigation of the origin of the source emission in various periods by generating as many SEDs of CTA 102 as possible that can be constructed with contemporaneous data and modelling them within the leptonic scenario.

## 4.2 MULTIWAVELENGTH OBSERVATIONS OF CTA 102

Exhibiting interesting multiwavelength properties, CTA 102 was frequently observed in different bands. Below we report the results of the analysed data or the data, which have been extracted from public archives which was used in the current study.

**FERMI LAT OBSERVATIONS OF CTA 102:** Operating since 2008, Fermi-LAT provides an exceptional view of the  $\gamma$ -ray sky, imaging the entire sky every three hours [98]. For the detailed study of  $\gamma$ -ray emission from CTA 102 the Fermi-LAT data accumulated between 04 August 2008 and 04 March 2022 in the 100 MeV - 300 GeV range were downloaded and

analysed using the Fermi ScienceTools version 2.0.8 and P8R3\_SOURCE\_V3 instrument response function. Events were extracted from a region of interest (ROI) with a  $12^\circ$  radius centered on the source position (RA: 338.15, DEC: 11.73). As recommended by the Fermi-LAT team, the cut `evclass=128` and `evtype=3` was applied to select events with higher probability of being photons. Whereas, the filter `(DATA_QUAL > 0) && (LAT_CONFIG == 1)` was applied to update the good time interval based on spacecraft specifications. A maximum zenith angle cut of  $> 90^\circ$  is applied to reduce the contamination from Earth limb  $\gamma$ -rays. The model file was generated based on Fermi-LAT fourth source catalog Data Release 3 (4FGL-DR3; [99, 145]) which includes point sources within the ROI and standard Galactic (`gll_iem_v07`) and the isotropic (`iso_P8R3_SOURCE_V3_v1`) diffuse emission components. The spectral parameters of the background sources falling between  $12^\circ$  and  $12^\circ + 5^\circ$  were fixed to the values published in the 4FGL-DR3 catalogue, while the parameters of the other sources (within  $12^\circ$ ) and background models were left free. The best match between the source parameters and the data was obtained by applying standard binned likelihood analysis with `gtlike` tool.

After analysing the data accumulated in the whole time interval, light curves were computed with different time bins to investigate the variability in the  $\gamma$ -ray band. Initially, the entire period was divided into three-day intervals (1653 in total) and for each single period the flux, photon index (CTA 102 spectrum was modelled with power-law distribution) and the Test Statistics (TS, defined as twice the difference between the log-likelihoods of the model computed with and without including the source; [52]) were estimated.

Next, for a deeper investigation of the  $\gamma$ -ray flux variability, the light curve was generated with the help of the adaptive binning method [146]. As distinct from the fixed time interval light curve where the longer bins will smooth out the fast variation and in short time intervals the flux can be estimated only in the bright state of the source, in the adaptively binned light curve the bin width is defined by requiring a constant relative flux uncertainty above an optimal energy, so the time bins are longer during low flux levels and narrower when the source is in flaring state. This allows to track the evolution of the  $\gamma$ -ray flux in time, extract

maximum possible information and identify flaring periods (e.g., see [100, 101, 102, 103, 104, 105, 147]).

The spectral changes in the  $\gamma$ -ray band were further investigated by producing the source spectrum in different periods. For this purpose, the adaptively binned light curve is divided into piece-wise constant blocks (Bayesian blocks [148]) representing optimal segmentation of the data into time intervals during which the flux is constant. By this approach, the considered period is divided into 347 intervals with the same flux level, whether flaring or quiescent. The spectrum of CTA 102 in each of the selected period is computed by applying unbinned likelihood analysis and running `gtlike` separately for 5 (when the source is in average or quiescent state) or 7 energy bins (when the source is in flaring state) of equal width in log scale.

**SWIFT OBSERVATIONS OF CTA 102:** In the optical/UV and X-ray bands there are available a total of 146 observations of CTA 102 with Swift XRT/UVOT instruments. All the XRT observations were individually downloaded and analysed using `Swift_xrtproc` pipeline [94]. This tool developed within the Open Universe Initiative downloads the raw data and calibration files from one of the official Swift archives, processes it using the `XRTPIPELINE` task for each snapshot and for the entire Swift observation, applies pile-up correction when the source count rate is above  $0.5 \text{ counts s}^{-1}$  and generates source (from a circle with a radius of 20 pixels centred at the position of the source) and background (an annular ring centred at the source) spectral files. It performs a spectral fitting with `XSPEC` (version 12.12.0) on the ungrouped data using Cash statistics [62], modelling CTA 102 spectrum as a power-law and a log-parabola. As a result, the tool generates SED data and estimates the flux and photon index in various bands. More details on `Swift_xrtproc` are given in [94].

The Swift-UVOT data in three optical filters (V, B, and U) and three UV filters (W1, M2, and W2) were downloaded and reduced using `HEASoft` version 6.29 with the latest release of `HEASARC CALDB`. The source counts were extracted from a region of 5 arcsec radius centred at the source and the background counts from a region of 20 arcsec centred away from the source. `uvotsource` tool was used to obtain the magnitude which was corrected for reddening

and galactic extinction using the reddening coefficient  $E(B - V)$  from the Infrared Science Archive<sup>19</sup>.

**NUSTAR OBSERVATION OF CTA 102:** NuSTAR with two focal plane modules [149], FPMA and FPMB, observed CTA 102 in the hard X-ray (3-79 keV) band on December 30, 2016 for a total exposure of 26.2 ksec. The NuStar data was processed with NuSTAR\_Spectra script which is a shell script based on the NuSTAR Data Analysis Software (NuSTARDAS) that automatically downloads calibrated and filtered event files from the SSDC repository, generates scientific products and carries out a complete spectral analysis. It uses nuproducts to generate the spectra from source counts extracted from a circular region whose radius is set to a value that is optimised depending on the source count rate (30" in this case), while the background counts are from an annulus centred on the source. With the XSPEC, the spectral analysis is performed adopting Cash statistics for the energy range from 3 keV up to the maximum energy where the signal is still present, typically between 20 and 79 keV. NuSTAR\_Spectra script is presented and described in [150].

**ARCHIVAL OPTICAL DATA:** In order to monitor the flux changes in the optical band, the light curves from several public archives were used. Namely, the optical data (V- and R- band) from Steward Observatory [151], V-band data from the All-Sky Automated Survey for Supernovae (ASAS-SN)<sup>20</sup> [152] and the V-band data from the Catalina Sky Survey (CSS) [153] were downloaded from the public archives.

### 4.3 MULTIWAVELENGTH VARIABILITY

The multiwavelength light curve of CTA 102 is shown in Figure 4.1. The adaptively binned light curve above 166.3 MeV in the  $\gamma$ -ray band and reveals the complex flux changes. During the considered periods several outbursts are observed. Until April 2011 the source flux was constant, not exceeding  $10^{-7}$  photon  $\text{cm}^{-2}$   $\text{s}^{-1}$ . The first flare (when  $F_\gamma > 15 \times F_{\gamma, \text{min}}$ ) occurred in April-June 2011 (MJD 55680-55730), when the flux increased up to  $(2.55 \pm 0.62) \times 10^{-6}$  photon  $\text{cm}^{-2}$   $\text{s}^{-1}$ . Other enhancements were observed between September-October 2012 (MJD 56180-56230) and between March-April 2013 (MJD 56380-56400). Yet,

---

<sup>19</sup> <http://irsa.ipac.caltech.edu/applications/DUST/>

<sup>20</sup> <https://asas-sn.osu.edu/>

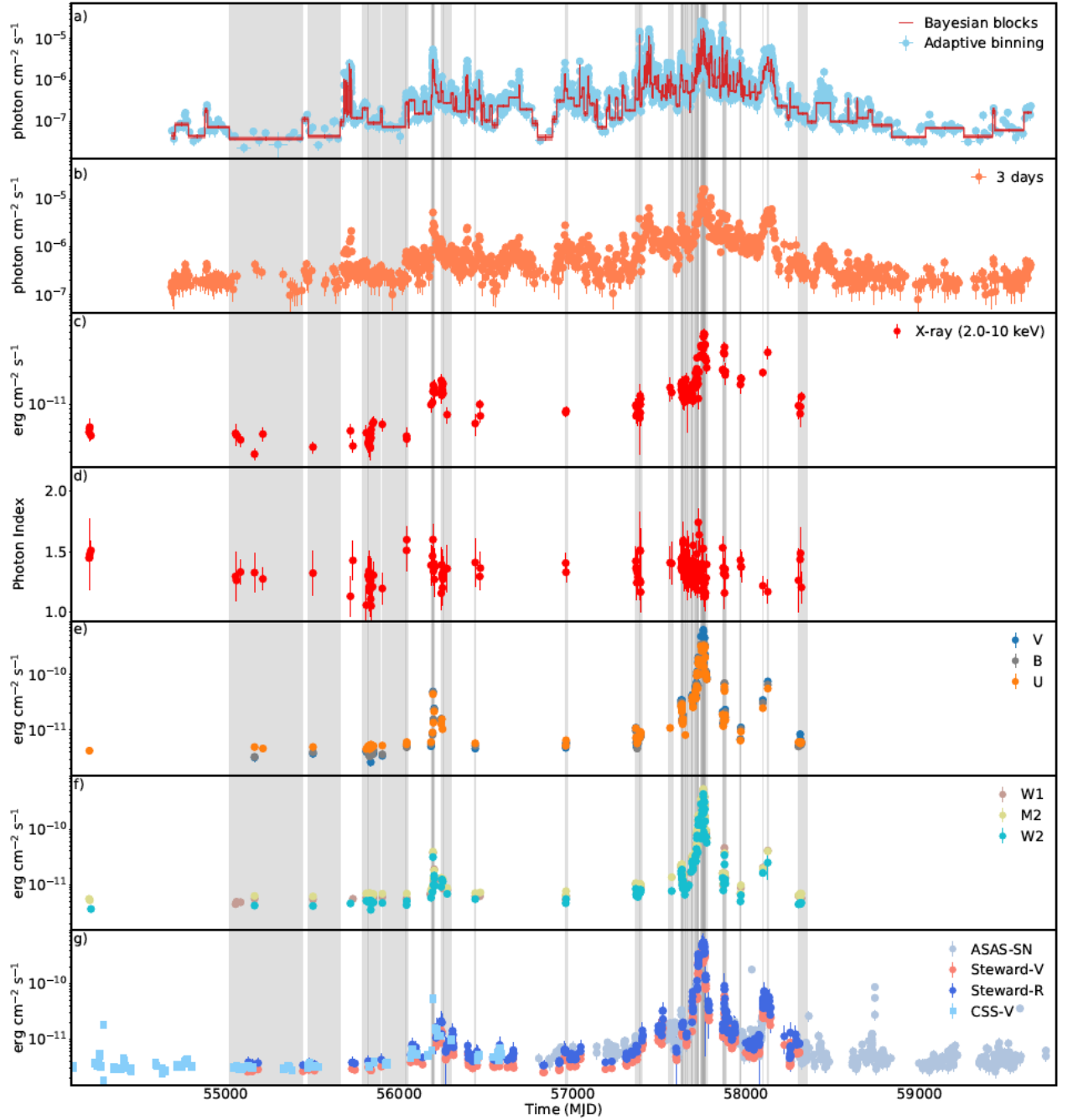


Figure 4.1: The multiwavelength light curve of CTA 102 between 2007 and 2022. a) Adaptively binned  $\gamma$ -ray light curve ( $> 166.3$  MeV) with the Bayesian blocks, b) 3-day binned  $\gamma$ -ray light curve, c) 2.0-10 keV X-ray flux, d) 0.3-10.0 keV X-ray photon index, e) flux in V, B, and U filters, f) flux in W1, M2 and W2 filters and g) V-band and R-band fluxes.

a major flaring activity, when the source flux increased above  $10^{-5}$  photon  $\text{cm}^{-2} \text{s}^{-1}$ , was observed between December 2015- March 2016 (MJD 57370-57470). Then, the source entered a prolonged out-bursting state between November 2016- June 2017 (MJD 57710-57910) when the highest flux of  $(2.64 \pm 0.60) \times 10^{-5}$  photon  $\text{cm}^{-2} \text{s}^{-1}$  above 166.3 MeV was observed on MJD 57738.5. Another brightening of the source (although with lower amplitude)

was observed between November 2017-March 2018 (MJD 58080-58180). During the considered period, the  $\gamma$ -ray flux of CTA 102 was above  $10^{-5}$  photon  $\text{cm}^{-2} \text{s}^{-1}$  for 121.1 hours in total. The ratio between the highest and lowest fluxes is  $\simeq 1137$  which again shows the high-amplitude variation of the  $\gamma$ -ray flux. The overall trends revealed in the  $\gamma$ -ray light curve generated by the adaptive binning method are also visible in the 3-day light curve (Figure 4.1 panel b)).

Together with the  $\gamma$ -ray flux, the photon index varies as well. The hardest photon index is  $\Gamma_{\gamma} = 1.52 \pm 0.12$  observed on MJD 57752.5 when the source was in bright  $\gamma$ -ray state with a flux of  $(1.02 \pm 0.20) \times 10^{-5}$  photon  $\text{cm}^{-2} \text{s}^{-1}$ . The distribution of photon index estimated in all adaptively binned intervals is shown in Figure 4.2 (light magenta). The mean of the photon index distribution 2.31 is the same as the timeaveraged photon index of the source in 4FGL DR3 ( $\sim 2.3$ ). However, there are 353 periods when the photon index was significantly hard ( $< 1.9$ ) which means that the peak of the HE component moved to HEs. In Figure 4.2, the blue area corresponds to photon index distribution only when the  $\gamma$ -ray flux was  $10^{-5}$  photon  $\text{cm}^{-2} \text{s}^{-1}$  which shows that in some of the bright states the photon index of the source was also hard.

The X-ray flux (2-10 keV) variation in time is shown in Figure 4.1 panel c). There is significant variability of the X-ray flux in different XRT observations. During the prolonged flaring in the  $\gamma$ -ray band, the source was also in an active X-ray emission state, when the X-ray flux reached  $F_{X\text{-ray}}[2 - 10\text{keV}] = (5.77 \pm 0.63) \times 10^{-11}$  erg  $\text{cm}^{-2} \text{s}^{-1}$ . The NuSTAR observation shows that the source flux in the 3-10 keV band is  $(4.46 \pm 0.02) \times 10^{-11}$  erg  $\text{cm}^{-2} \text{s}^{-1}$  in agreement with the X-ray flux observed by Swift XRT on the same day  $F_{X\text{-ray}}[2 - 10\text{keV}] = (5.30 \pm 0.47) \times 10^{-11}$  erg  $\text{cm}^{-2} \text{s}^{-1}$ . As the X-ray band corresponds to the rising part of the HE component, the flux in the 10-30 keV band increases being  $(9.04 \pm 0.05) \times 10^{-11}$  erg  $\text{cm}^{-2} \text{s}^{-1}$ . Also, the Swift XRT and NuSTAR observations reveal similar photon indexes in the 0.3-10 keV and 3-30 keV bands,  $1.25 \pm 0.08$  and  $1.30 \pm 0.01$ , respectively.

In Figure 4.1 panels e), f) and g), the flux variation in the optical/UV band is shown. In the optical band, the source's emission follows the same trend as in the  $\gamma$ -ray and X-ray bands.

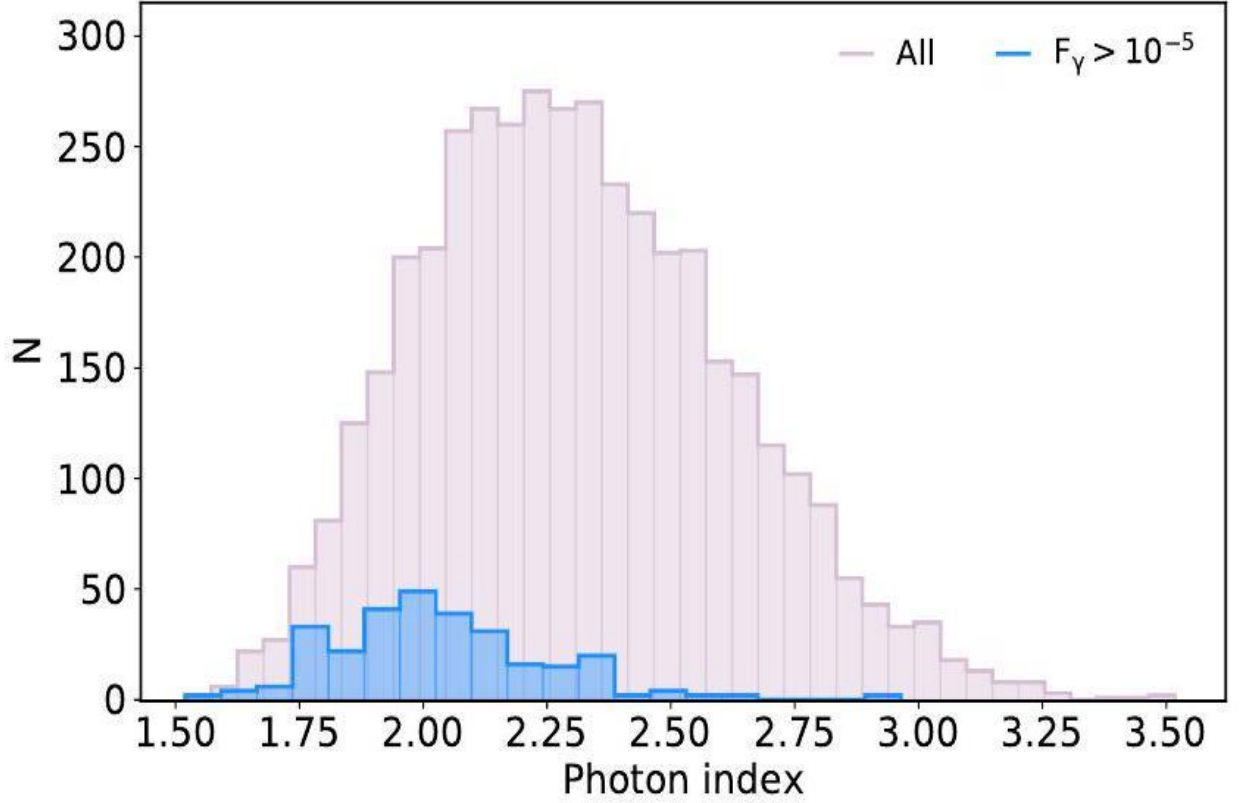


Figure 4.2: The distribution of the  $\gamma$ -ray photon index estimated in the adaptively binned intervals. The red area shows the total distribution, while the blue is only when the  $\gamma$ -ray flux was above  $10^{-5}$  photon  $\text{cm}^{-2} \text{s}^{-1}$ .

Namely, Swift UVOT, ASAS-SN, Steward (V and R band) and CSS observations show that the flux was relatively constant up to MJD 56000 and then increased several times around MJD 56200. However, long-lasting flaring activity was observed between MJD 57400-58000 when the flux in the optical band, as observed with all the considered instruments, was above  $10^{-11}$  erg  $\text{cm}^{-2} \text{s}^{-1}$ . The highest flux of  $(6.38 \pm 0.19) \times 10^{-10}$  erg  $\text{cm}^{-2} \text{s}^{-1}$  was observed in the V-band on MJD 57751.84 by Swift UVOT. The Swift UVOT observations show that between MJD 57718-57768 (November 2016-January 2017), the source was in an extreme bright state in the optical/UV band when the flux was above  $10^{-10}$  erg  $\text{cm}^{-2} \text{s}^{-1}$ . This is in agreement with the results obtained from CTA 102 monitoring by the Whole Earth Blazar Telescope (WEBT) [130]. The ASAS-SN monitoring of the source shows that another flaring activity was observed on MJD 58741 and then the source's emission in the optical band was on its regular level.

#### 4.4 BROADBAND SED MODELING

One of the ways for investigation of the underlying physical processes in the jet is through broadband SED modelling. The SEDs constrained with contemporaneous or quasi-

contemporaneous data contain valuable information on the emitting particle spectrum and on the condition of the plasma inside the jet. The evolution of the CTA 102 SEDs in time is shown here<sup>21</sup>. These SEDs were generated by plotting the  $\gamma$ -ray spectra for each of the Bayesian blocks shown in Figure 4.1 together with the data available in all other energy bands. In a visually effective way, the temporal changes in the CTA 102 spectra can be seen by going from one to another interval. This animation shows the high-amplitude and spectral changes in different periods, demonstrating dramatic changes of the CTA 102 during the prolonged outbursting period.

In FSRQs, such as CTA 102, a one-zone synchrotron/synchrotron-self Compton (SSC) with an external radiation component is expected to produce the broadband emission. The origin of the external photons depends on the location of the emitting region [39] and photons directly emitted from the disc [154, 155], reflected from the BLR [12] or emitted from the dusty torus [10] can inverse Compton up-scatter and explain the second component in the broadband SED. In the current study we assume that the emitting region is at  $10^{17}$  cm distance from the black hole within the BLR and the external photons are the disc-emitted photons reflected from the BLR clouds. The SED modelling when different locations of the emitting region are considered is presented in [100] and [5].

Here, we consider a one-zone leptonic model of jet emission, assuming the accelerated electrons (protons) are injected in the spherical region of radius  $R$ . This magnetized region with a field strength of  $B$  moves along the jet with a bulk Lorentz factor of  $\Gamma_{jet}$  at an angle of  $\theta$  relative to the observer's line of sight. As the jet is almost aligned to the observer (small  $\theta$ ), the emission is Doppler boosting by a beaming factor of  $\Gamma_{jet} = \delta$ . It is assumed that the spectrum of the injected electrons is described by a power-law with an exponential cutoff energy distribution defined as

$$N(\gamma_e) = N_0 \gamma_e^{-p} \text{Exp}(-\gamma_e/\gamma_{cut}), \gamma_e > \gamma_{min} \quad (5.1)$$

where  $\gamma_{cut}$  and  $\gamma_{min}$  are the cut-off and minimum energy of the electrons, respectively, and  $p$  is the power-law index of the electron energy distribution. The normalization constant  $N_0$  defines the energy density of the electrons:  $U_e = m_e c \int \gamma_e N(\gamma_e) d\gamma_e$ .

---

<sup>21</sup> [https://youtu.be/jFNkl\\_psAjo](https://youtu.be/jFNkl_psAjo)

In this scenario, the first peak in the SED is described by synchrotron radiation as a consequence of the interaction of relativistic electrons inside the emitting region with the magnetic field. Instead, the second peak (from X-ray to HE  $\gamma$ -rays) is formed by the contribution of inverse Compton scattering of synchrotron (SSC) and BLR reflected (EIC) photons. The BLR radius and luminosity of CTA 102 are  $R_{\text{BLR}} = 6.73 \times 10^{17}$  cm and  $L_{\text{BLR}} = 4.14 \times 10^{45}$  erg s $^{-1}$  [156], respectively, and the BLR is modelled as a spherical shell with a lower boundary of  $R_{\text{in,BLR}} = 0.9 \times R_{\text{BLR}} = 6.06 \times 10^{17}$  cm and an outer boundary of  $R_{\text{out,BLR}} = 1.2 \times R_{\text{BLR}} = 8.08 \times 10^{17}$  cm. Assuming that the 10% of the disc luminosity is reprocessed into BLR radiation, the disc luminosity would be  $L_{\text{disc}} = 4.14 \times 10^{46}$  erg s $^{-1}$ . To model the broadband SED, a publicly available code, JetSet was used [61, 157, 158, 159]. JetSet fits the numerical models to observed data and is able to find the optimal values of parameters best describing the data. The multiwavelength SED of CTA 102 constrained with contemporaneous data observed during MJD 56196.7-56202.3 and modelled with JetSet is shown in Figure 4.3. The dashed violet line shows the disc thermal emission approximated as a black body. The power-law index of the emitting electrons is  $p = 1.61$  while the minimum and cut-off energies are  $\gamma_{\text{min}} = 51.3$  and  $\gamma_{\text{cut}} = 685.6$ , respectively. The synchrotron emission of these electrons in the magnetic field of  $B = 4.43$  G extends up to  $10^{16}$  Hz explaining the observed data in the optical/UV bands. Then, the SSC component takes into account the X-ray data (orange dashed curve in Figure 4.3) dominating only up to  $10^{22}$  Hz, failing to explain the  $\gamma$ -ray data. Instead, the inverse Compton upscattering of the BLR photons that have higher mean energy and number density in the jet frame can explain the  $\gamma$ -ray data (purple dot-dashed curve in Figure 4.3). The modelling allows to estimate the jet parameters such as size of the emission region,  $R = 2.03 \times 10^{15}$  cm and the Doppler factor  $\delta = 29.8$ . The size of the emission region corresponds to the flux variability of the order of 1.3 hours, consistent with the rapid multi-band variability of CTA 102.

The modelling of the single snapshot SED shown in Figure 4.3 permits to identify the parameters of the emitting region and the jet for a given period. However, in order to deeply investigate the multiwavelength emission processes in CTA 102 something beyond the single-epoch SED modelling is required. In [144] and [114] the multiwavelength emission from 3C

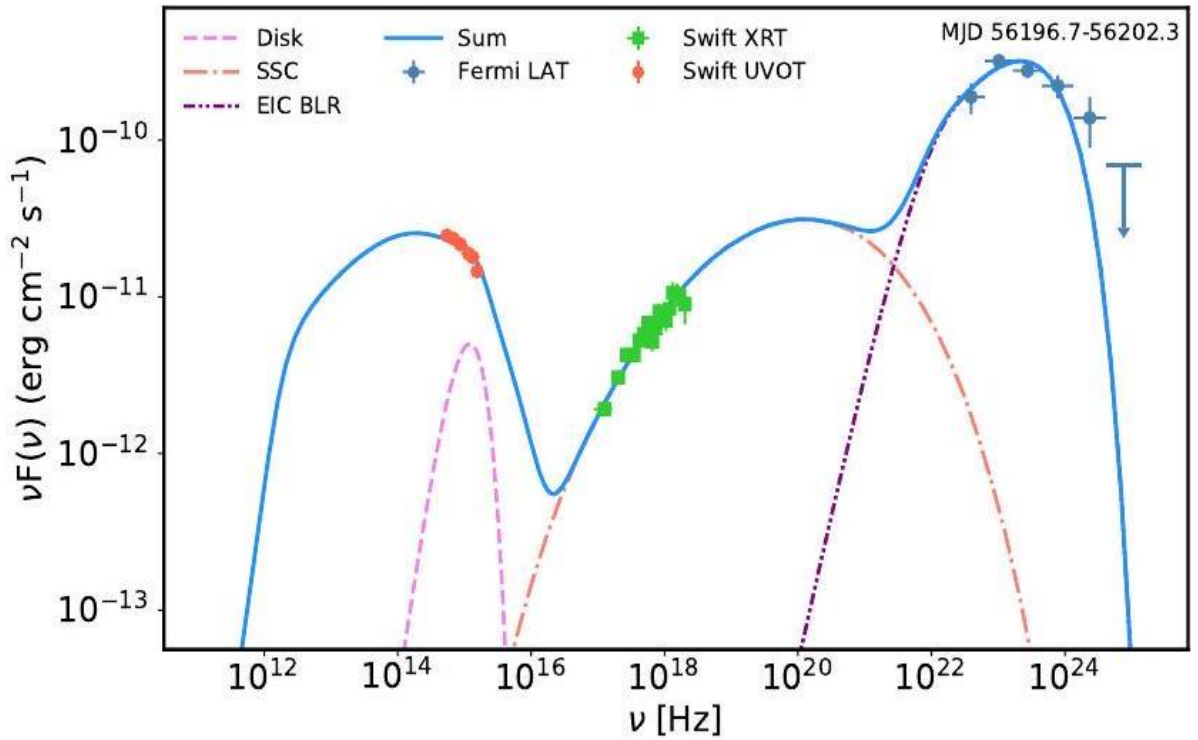


Figure 4.3: The multiwavelength SED of CTA 102 during MJD 56196.7-56202.3 constructed with the data from Swift UVOT, XRT and Fermi-LAT. The light blue line is the sum of all components; SSC component is in orange and EIC in purple.

454.3 and BL Lac was investigated by modelling as many contemporaneous SEDs as possible constrained during the considered periods. As compared with the single snapshot SED modelling, the advantage of such an approach is that it allows to follow the changes also in the parameters over time, thus get a clue on the evolution of the processes that have lead to the emission in different states (e.g., flares). In addition, such modelling has diagnostic applications, i.e., by fitting many SEDs it is possible to identify periods when the source was characterized with peculiar emission properties that are not possible to explain within the considered model. In order to model the SEDs of CTA 102 in different periods, from the SED/light curve animation there were selected all the periods with sufficient multiwavelength data, i.e., when the data in the optical/UV, X-ray and  $\gamma$ -ray bands were available. This resulted in assembling 117 high-quality SEDs which represent various emitting states of CTA 102 including periods when it was in a prolonged flaring state in the  $\gamma$ -rays. Therefore, this allows to understand the physical processes dominating in the jet of the source in its quiescent and flaring states. All the selected SEDs are modelled within the same one-zone scenario described

above.

## 4.5 RESULTS AND DISCUSSION

In this section, the implications of the data analysis are discussed, and the results from the broadband spectral fitting are presented.

**MULTI-BAND FLUX CHANGES:** In the optical/UV, X-ray and  $\gamma$ -ray bands, CTA 102 exhibits complex flux changes showing multiple flaring periods. The highest amplitude changes are observed in the HE  $\gamma$ -ray band where the  $\gamma$ -ray luminosity of the source varies from  $8.50 \times 10^{46} \text{ erg s}^{-1}$  to  $7.55 \times 10^{50} \text{ erg s}^{-1}$  (assuming a distance of 7.1 Gpc) which makes CTA 102 one of the brightest sources in the extragalactic  $\gamma$ -ray sky.

The visual inspection of the multiwavelength light curves in Figure 4.1 shows that fluxes in different bands change almost simultaneously. Possible correlation or anticorrelation between the fluxes in different bands shows whether or not the emission is produced by the same population of the particles and related mechanisms. In the case of one-zone leptonic scenario considered here, the same electron population is responsible for the emission. So, one expects correlation between the photons at different frequencies. The interband correlation was tested considering the time window between MJD 57000-59310, since most of the Swift observations were carried out in this period and moreover the source was flaring in all the bands.

The emission in different bands is compared using the Spearman rank-order correlation test which is a measure of the correlation between two samples. The results of the correlation analyses are shown in Figure 4.4 comparing the emission in the  $\gamma$ -ray band with that in the X-ray (panel a) and V band (panel b) as well as comparing the emission in the X-ray and V bands. When comparing the emission in the  $\gamma$ -ray and X-ray bands, the analysis yielded a Spearman coefficient of 0.80, implying positive correlation: when the  $\gamma$ -ray flux increases, the source was in high X-ray state (see Figure 4.4 panel a). Similarly, the test between the  $\gamma$ -ray and V-band as well as X-ray and V band results in correlation coefficients of 0.84 and 0.82, respectively, implying positive correlation. A strong correlation with no time lag between R and  $\gamma$ -ray bands was reported in [137]. It should be noted that the test comparing all the bands shown in Figure 4.1 shows positive correlation with correlation coefficients of  $> 0.79$ .

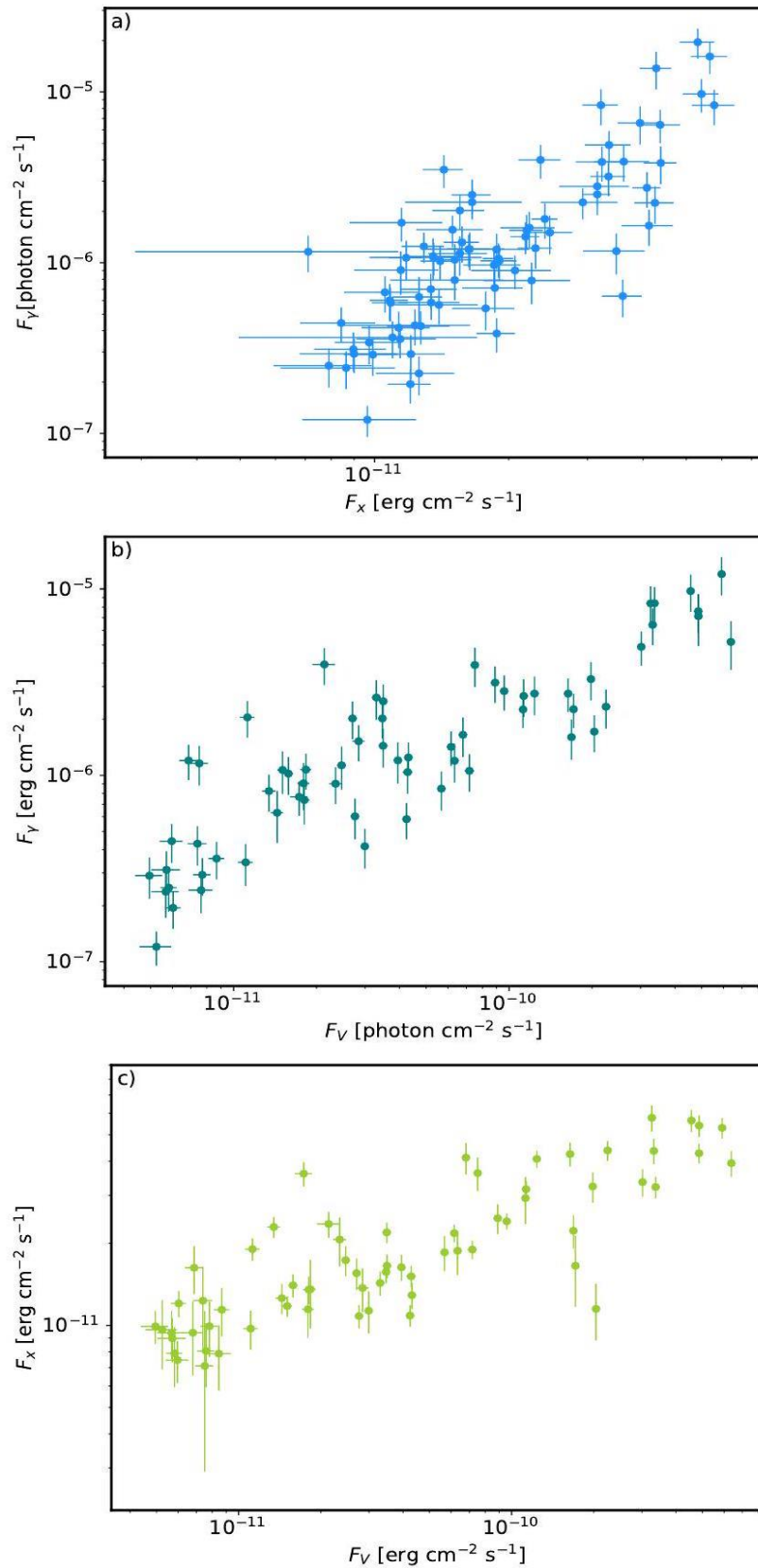


Figure 4.4: Interband correlation study. Panels a), b) and c) show the correlation between the emission in  $\gamma$ -ray versus X-ray,  $\gamma$ -ray versus V and X-ray versus V bands, respectively.

The results from the Spearman correlation analysis suggest a common origin of the emission in these bands. The optical/UV photons are from synchrotron emission of the electrons while the emission in the X-ray and  $\gamma$ -ray bands is from the inverse Compton scattering of internal and external photon fields by the electrons in the same emitting region.

**LONG-TERM BROADBAND SED MODELING:** The one-zone leptonic model adopted here can adequately reproduce the observed data in almost all the considered periods. The datasets considered here, namely optical/UV, X-ray and  $\gamma$ -ray data, contain relevant information on the source emission in each band, but together they put a constraint on the shape of the emitting particle distribution. Except for the cases when the source is in a very low emission state and the optical/UV emission is (partly) dominated by the thermal emission from the disc, the decaying shape of the optical/UV data directly constrains the HE tail of the synchrotron component which controls the cut-off energy of the emitting electrons ( $\gamma_{cut}$ ). Instead, the X-ray spectrum exhibiting rising shape allows to constrain  $p$ . Additional constraints on the  $\gamma_{cut}$  and  $p$  are provided from  $\gamma$ -ray observations: depending on the shape of the  $\gamma$ -ray spectrum, rising, steepening or flat, it defines either the distribution of the particles or their cut-off energy.

The time evolution of the selected SEDs modelling is available here<sup>22</sup>. In Figure 4.5 the SED modelling results are shown for each case separating synchrotron (light blue), SSC (orange) and EIC (purple) components. The models are shown by separating the periods when CTA 102 was in the active states in all the bands (panel a) and in all the other periods (panel b). The low-energy component peaks, as typical for FSRQs, is around  $\sim 10^{14}$  Hz and is mostly defined by the synchrotron emission of the jet electrons. Although the flux of the synchrotron component varies largely, i.e., in the low state the peak flux can be as low as  $10^{-12}$  erg cm<sup>-2</sup> s<sup>-1</sup> but it can increase up to  $\sim 10^{-10}$  erg cm<sup>-2</sup> s<sup>-1</sup> during the flares, the synchrotron peak frequency remains relatively unchanged. However, in several occasions (e.g., between MJD 55228- 56190 and MJD 58297-58353) the disc thermal emission with a flux of  $\sim 6.86 \times 10^{-11}$  erg cm<sup>-2</sup> s<sup>-1</sup> exceeds the synchrotron emission from the jet (violet dashed line in Figure 4.5 panel b). As one can see from Figure 4.1, in the mentioned periods

---

<sup>22</sup> <https://youtu.be/OH1lyNN9PSM>.

the accretion disc of CTA 102 overshines the synchrotron component. The relatively constant peak frequency of the synchrotron component limits also the highest energy of the synchrotron photons, and their inverse-Compton scattering steepens in the hard X-ray/soft  $\gamma$ -ray bands, unable to explain the observed  $\gamma$ -ray data (SSC; orange dot dashed lines in Figure 4.5). Instead, the Compton dominance (the ratio of the high-to-low components luminosity) and the  $\gamma$ -ray spectra are naturally explained by inverse Compton scattering of BLR photons (EIC; purple dot-dashed lines in Figure 4.5).

The models shown in panels a) and b) of Figure 4.5 demonstrate different behaviour of the CTA 102 emission in active and other states. The brightening of the source substantially modifies different components affecting their flux and spectrum. For example, when modelling the SED in the bright X-ray state characterized by a hard X-ray photon index, the intensity of the SSC component increases and its spectrum hardens extending the peak of this component to higher energies (panel a) Figure 4.5). However, for a harder photon index (hence a lower  $p$ ),  $\gamma_{cut}$  should be lower not to violate the optical/UV data. So, even in those bright and hard X-ray states the SSC component has a decreasing shape in the GeV band, and again the Fermi-LAT observed data are interpreted as inverse-Compton up-scattering of BLR reflected photons. Similarly, the spectral variability in the MeV/GeV band affects the EIC component.

As an example, the SED of CTA 102 during MJD 57872.9-57875.6 is shown in Figure 4.6. During this period, the MeV/GeV spectrum is characterized by a nearly flat spectrum extending up to 58 GeV. The modelling shows that the distribution of the emitting electrons is described by  $p = 1.87$  power-law index and the cut-off energy of  $\gamma_{cut} = 306.4$ . So, the inverse Compton scattering of BLR photons can reach only 2 GeV unable to explain the observed data in tens of GeV. The limit imposed by the emitting electron distribution prohibits the interpretation of GeV data within one-zone scenarios; the observed data can be account for only when the photons with higher mean energy are inverse Compton up-scattered on the same electrons. In the emitting region, except for BLR, the electron can interact with disc photon or the photons emitted from the dusty torus. The inverse Compton scattering of the disc photons will produce a peak comparable to that shown in Figure 4.6 whereas in the case

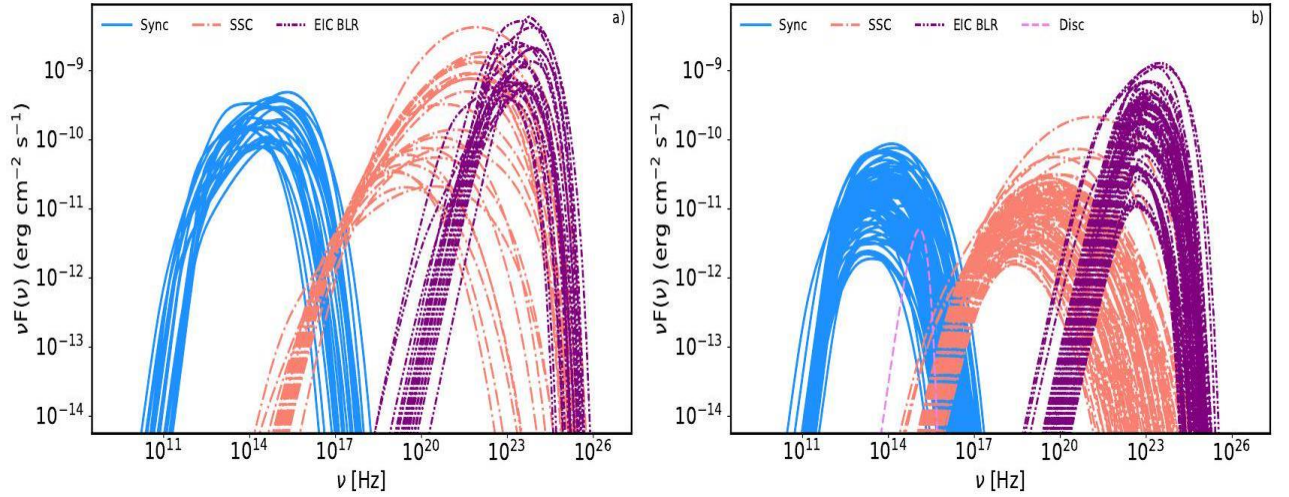


Figure 4.5: The Multiwavelength SED modeling in different periods. Panel a: Synchrotron, SSC and EIC BLR components when the source was in an active state in all the considered bands. Panel b: The same components in all other periods.

of the dusty torus photons with a lower mean energy will produce a peak at lower frequencies. The emission in the  $> 2$  GeV band is most likely produced from the second emission region containing more energetic electrons. As an example, in Figure 4.6 the GeV data are modelled as emission from the second region which is assumed to be outside the BLR. As the data are not sufficient to constrain the parameters, it is assumed that this region:

- i) Has the same Doppler boosting factor ( $\delta = 29.4$ ) as the one inside the BLR (constrained from the fit),
- ii) Is characterized by a significantly lower magnetic field (0.2 G as compared to 12.3 G estimated for the other region) not to overproduce the X-ray data which are from the region within the BLR,
- iii) Contains more energetic electrons with  $p = 1.80$  and  $\gamma_{cut} = 1.10 \times 10^4$ .

As the emitting region is BLR outside the BLR, the dominant photon field is IR photons from the dusty torus; the inverse Compton up-scattering of these photons is shown with a light red dashed line in Figure 4.6 which extends up to GeV bands and accounts for the observed data. In principle, the second emission region can be a local structure in the jet where the particles are re-accelerated (e.g., a local reconnection outflow in the "jet in a jet" scenario ([160, 161]) or there occurs an injection of fresh electrons. The modelling presented above is to show that the observed data in some cases (e.g., when the  $\gamma$ -ray spectrum is flat and extends to tens of

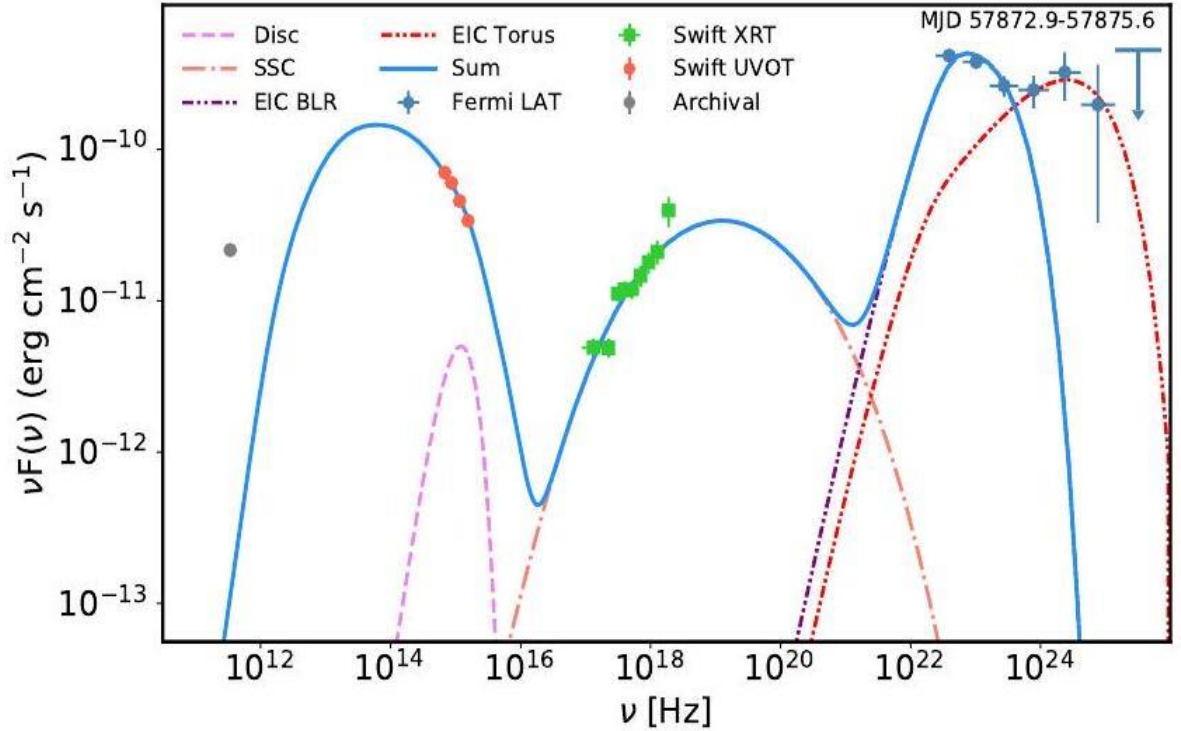


Figure 4.6: The multiwavelength SED of CTA 102 during MJD 57872.9-57875.6 when the  $\gamma$ -ray spectrum was flat, extending up to 58 GeV.

GeV, two among the selected SEDs) cannot be reproduced in one zone scenarios, so that more complex (e.g., two-zone) scenarios are required.

**ENERGY DISTRIBUTION OF THE EMITTING ELECTRONS:** The modelling of 117 high-quality SEDs of CTA 102 with diverse features allows to investigate the properties of the jet and emitting particles over time. In Figure 4.7 the distribution of  $p, \gamma_{\min}, \gamma_{\text{cut}}, B, L_e$  and  $L_B$  obtained from the modeling are shown. The wide distribution of the considered parameters once more shows the complex changes having taken place in the jet of CTA 102. The power-law index of the emitting electron distribution varies between  $p = 1.17 - 3.25$  with a mean of  $p_{\text{mean}} = 2.08$  (Figure 4.7 panel a). This power-law index constrained by the X-ray and  $\gamma$ -ray data varies following the spectral changes in the X-ray and  $\gamma$ -ray bands; when a steep falling spectrum is observed in the  $\gamma$ -ray band, the emitting electron should also have a steep spectrum, while  $p < 2.0$  are expected in bright active states that are characterized by a hard photon index. The distribution of  $\gamma_{\min}$  and  $\gamma_{\text{cut}}$  is shown in Figure 4.7 panel b). Both parameters have a narrow distribution peaking around  $\gamma_{\min, \text{mean}} = 104.6$  and  $\gamma_{\text{cut, mean}} = 905.1$ , respectively. The narrow distribution of  $\gamma_{\text{cut}}$  (between  $(1.60 - 48.16) \times 10^2$ ) is

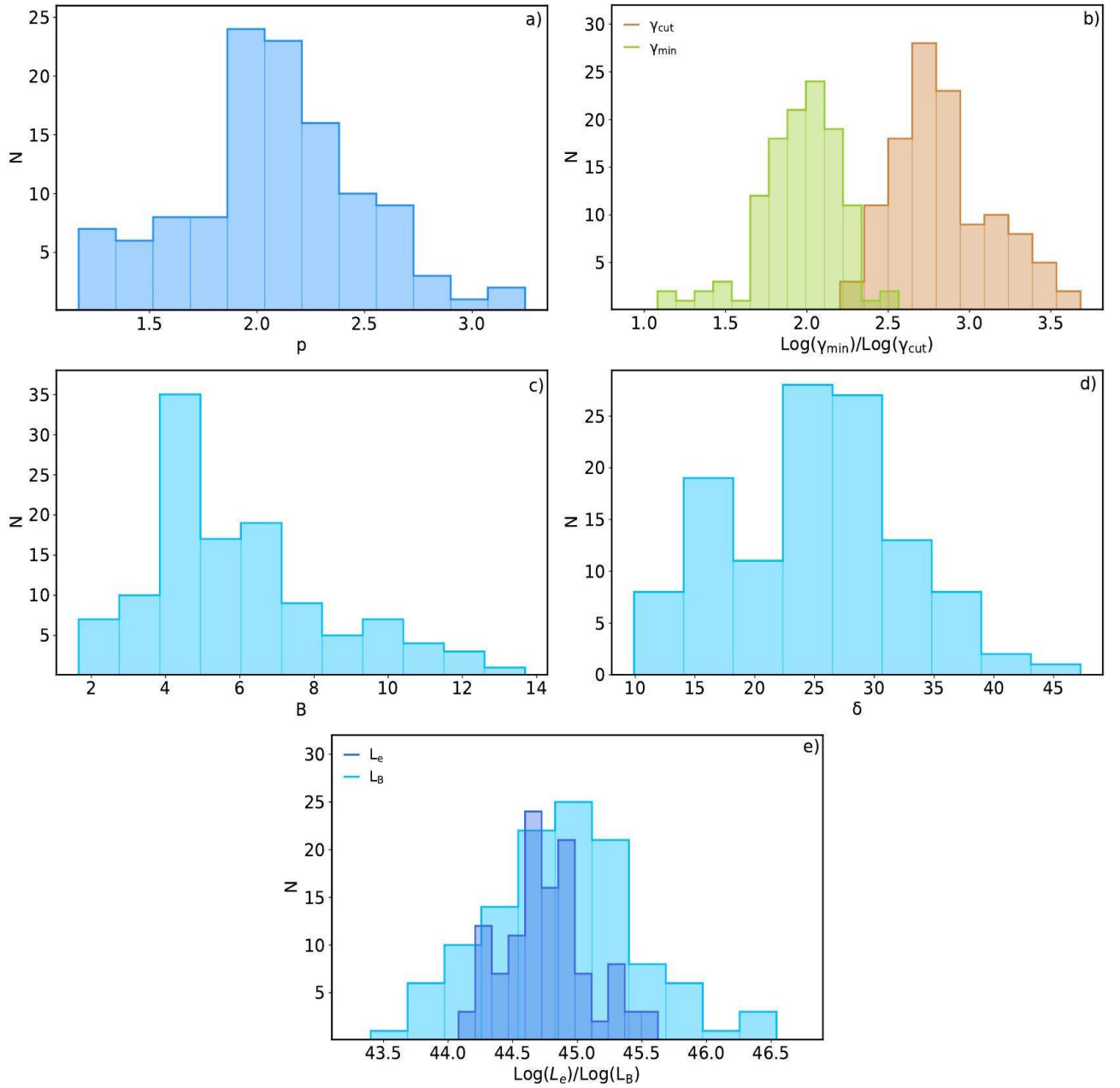


Figure 4.7: The distribution of the parameters obtained from the fitting of all data-sets composed with simultaneous data.

probably due to stability of  $v_{peak}$  but in general it depends also on  $p$ . The magnetic field estimated in different periods (Figure 4.7 panel c), varies from  $B = 1.66$  G to  $B = 13.69$  G with a mean of  $B_{mean} = 5.96$  G. This change in the magnetic field is defined by an almost two orders of magnitude variation of the synchrotron component (Figure 4.5).

The distribution of  $\delta$  in different periods is shown in Figure 4.7 panel d). The high values of  $\delta$  are mostly estimated during the flares in the  $\gamma$ -ray band, for example, the highest value of  $\delta = 47.2$  was observed on MJD 57743.2 when the source was in a  $\gamma$ -ray active state. When

$\delta$  increases, a lower electron density is required to produce the same level of synchrotron radiation, so the synchrotron photon density and the SSC component decrease but the external photon energy density in the jet frame becomes larger leading to the increase of the EIC component. For this reason, the enhancement in the  $\gamma$ -ray band results in higher  $\delta$ .

The parameters distribution presented in Figure 4.7 does not differ from that usually estimated for CTA 102 in different periods. For example, in [100] by considering different locations of the emission region it is found that SSC and EIC of BLR photons can explain the broadband SED in the low state when  $p = 2.51 \pm 0.11$ ,  $\gamma_{\text{cut}} = 1311.1 \pm 195$ ,  $B = 5.40 \pm 0.13$  and  $\delta = 10$ . Whereas in the active state, the data can be explained when these parameters are:  $p = 1.81 \pm 0.09$ ,  $\gamma_{\text{cut}} = 724.1 \pm 78$ ,  $B = 8.24 \pm 0.18$  and  $\delta = 30$  [5]. Or in Prince et al. [134] by assuming a log-parabolic electrons injection spectrum, it is shown that in a pre-flare state the SED of CTA 102 can be modelled when the injection index of the electrons is 1.9 and the curvature is 0.08 but in the flaring states the index becomes 1.7 with a curvature of 0.02. The magnetic field is estimated to be around 4 G. Moreover, it should be noted that there are other models which explain the flaring activity of CTA 102, e.g., those considering the ablation of a gas cloud penetrating the relativistic jet and computing the expected multiwavelength emission from the leptonic and hadronic interactions, see Zacharias et al. ([132]) and Zacharias et al. ([133]). Also, the parameters estimated within these models are not significantly different from those presented in Figure 4.7.

**FORMATION OF ELECTRON SPECTRUM:** The electron spectrum given in Eq. 5.1 is an ad-hoc assumption of the distribution of particle injected in the emitting region. This approach, however, ignores the formation of the particle spectrum which is governed by different cooling processes and gains through particle energization mechanisms. From the theoretical point of view, the mechanisms usually considered for the particle acceleration are shock acceleration (e.g., [162, 163, 164]) or magnetic reconnection (e.g., [165, 166, 167]). However, all the considered mechanisms to some degree face difficulties to explain all the constraints imposed from the multiwavelength SED modellings. Here we do not attempt to discuss the exact mechanisms that have led to the particle acceleration and injection in the emitting region but instead we investigate whether or not the distribution of the electron

spectrum necessary to model the broadband SEDs of CTA 102 can be formed under the physical conditions considered above. A more straightforward approach to gain much information on the particle acceleration and cooling mechanisms would be self-consistent consideration of particle spectrum from acceleration to cooling and comparing its radiative signature with the multiwavelength data.

Figure 4.8 upper panel shows the distributions of the electrons estimated from the modelling of selected SEDs. This clearly demonstrates different properties of the emitting particles and their evolution in time. In particular, the spectrum of the electrons sometimes is hard ( $p < 2.0$ ) and extends above  $\gamma_e > 10^3$  however steep and narrow distributions were also obtained. The power-law index of the electron distribution directly points to the acceleration mechanisms which is unknown while  $\gamma_{\text{cut}}$  is due to the interplay of acceleration and cooling processes. In order to calculate the temporal evolution of the electron spectrum, an integro-differential equation that takes into account the injection, cooling (considering all the radiative fields) and escape of the particles should be solved [168]. This is done using JetTimeEvol class of the JetSet. This class numerically solves the kinetic equation and allows to evolve the particle distribution under any cooling process. In the electron distribution the limiting factors constraining  $\gamma_{\text{cut}}$  are the efficiencies of the acceleration process (namely the acceleration/injection time  $t_{\text{inj}}$ ) and the physical size of the accelerator. In other words, the electrons will not be accelerated beyond the energies when the radiative cooling time ( $3/4c\sigma_T \frac{U_{\text{tot}}}{m_e c^2} \gamma^2$ , where  $U_{\text{tot}}$  is the sum of magnetic and photon fields) is shorter than the acceleration time. In the one-zone scenario considered here when the emission region is within the BLR, the electrons are cooled through interaction with the magnetic and photon fields, so  $U_{\text{tot}}$  is synchrotron plus photon energy density, i.e.  $U_{\text{tot}} = U_B + U_{\text{SSC}} + U_{\text{EIC}}$ . In order to discuss the evolution of the particle distribution in time, we assume that power-law distributed electrons with  $p = 1.25$  are injected into the emitting region where the magnetic field is 4.1 G and  $\delta = 24.2$ . These are chosen to be similar to the parameters estimated from the SED modelling observed during MJD 57715.6-57716.8 (see the SED modelling animation) when the source was in an active emission state. In this case, the synchrotron cooling time for the electrons with energy of  $\gamma_e = 10^4$  is  $t_{\text{syn,cool}} = 4 \times 10^3$  s.

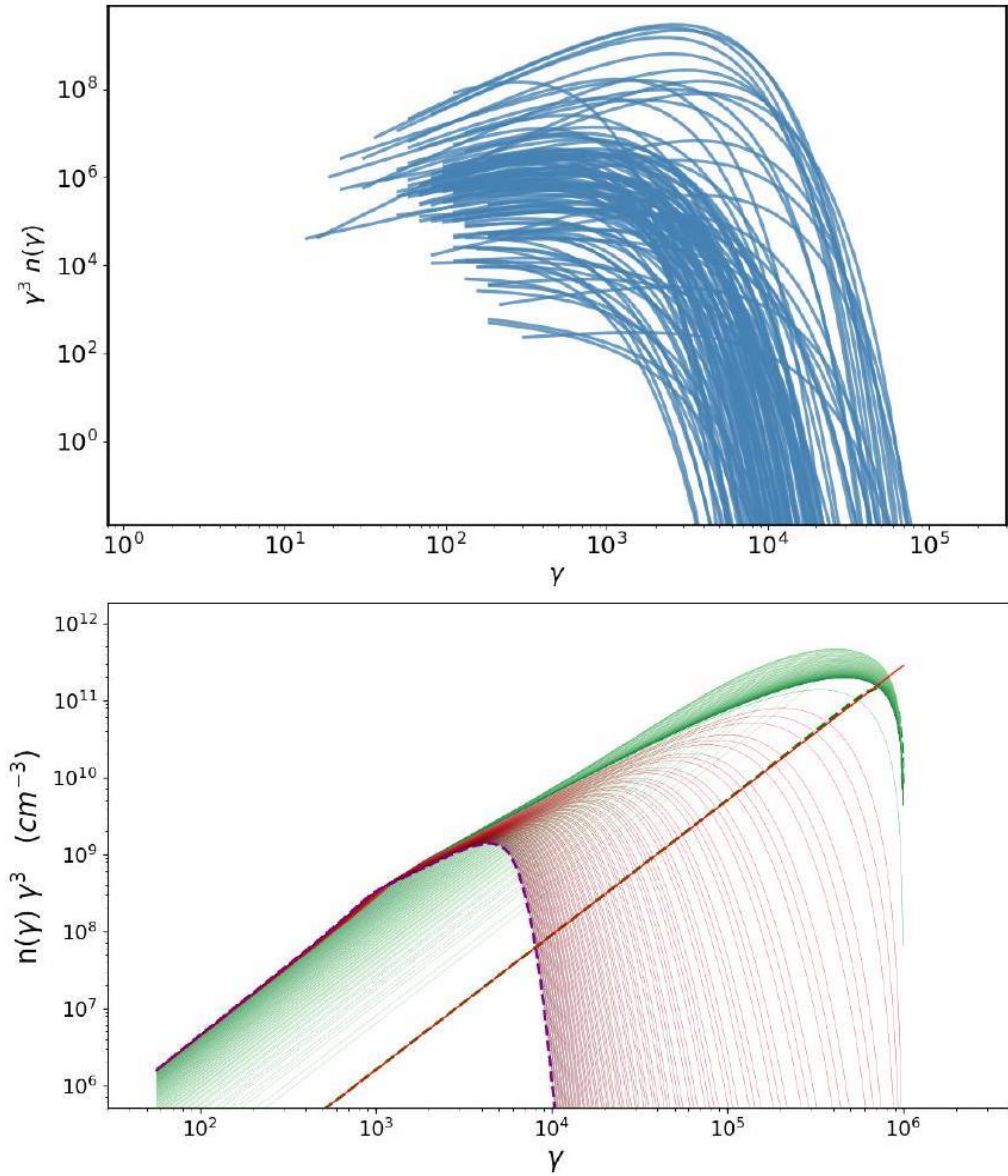


Figure 4.8: *Upper panel:* Electron energy distributions obtained from modeling of SEDs. *Lower panel:* The evolution of the energy spectrum of the electrons injected in the emitting region. The final spectrum is shown in purple.

The evolution of the energy spectrum of electrons with a luminosity of  $L_e = 1.74 \times 10^{45} \text{ erg s}^{-1}$  injected into the emitting region with a radius of  $2.38 \times 10^{15} \text{ cm}$  and without escape is shown in Figure 4.8 lower panel. The red dashed line corresponds to the initial injection spectrum of the electrons. As the cooling time is inverse proportional to the energy of the electrons, initially only the highest energy electrons are cooled down, forming a turnover (cut-off) in the spectrum. In time, this cut-off energy gradually moves to lower energies and when the injection time is  $\approx 2.6 \times 10^3 \text{ s}$  the cut-off energy will be around

$1.5 \times 10^3$  close to the value estimated from SED modeling. In time, however, this cut-off energy will move to lower ranges.

When the injected electrons start to cool, their radiative signature changes in time. The SEDs corresponding to electron spectra given in Figure 4.8 lower panel are shown in Figure 4.9. The SED of initially injected electrons (the sum of synchrotron, SSC and EIC components) is shown with green dashed line. This spectrum modifies in time when the injected electrons start to cool; the green solid lines show the evolution of the sum of all component in time which shows that the synchrotron and inverse Compton peaks move to lower frequencies. By cooling, the highest energy electrons are transferred to lower energies, so the number of low-energy (i.e., not cooled) electrons changes and their synchrotron emission increases at lower frequencies (e.g., around  $10^{12}$  Hz). Similarly, the SSC component increases in the X-ray band, while EIC dominates in the HE  $\gamma$ -ray band. The blue line in Figure 4.9 is the final SED produced from the electron population with a spectrum shown by a purple line in Figure 4.8 lower panel. It matches with that obtained from the modelling of SED observed on MJD 57715.6-57716.8 when using electron distribution given by Eq. 5.1. For later periods, the

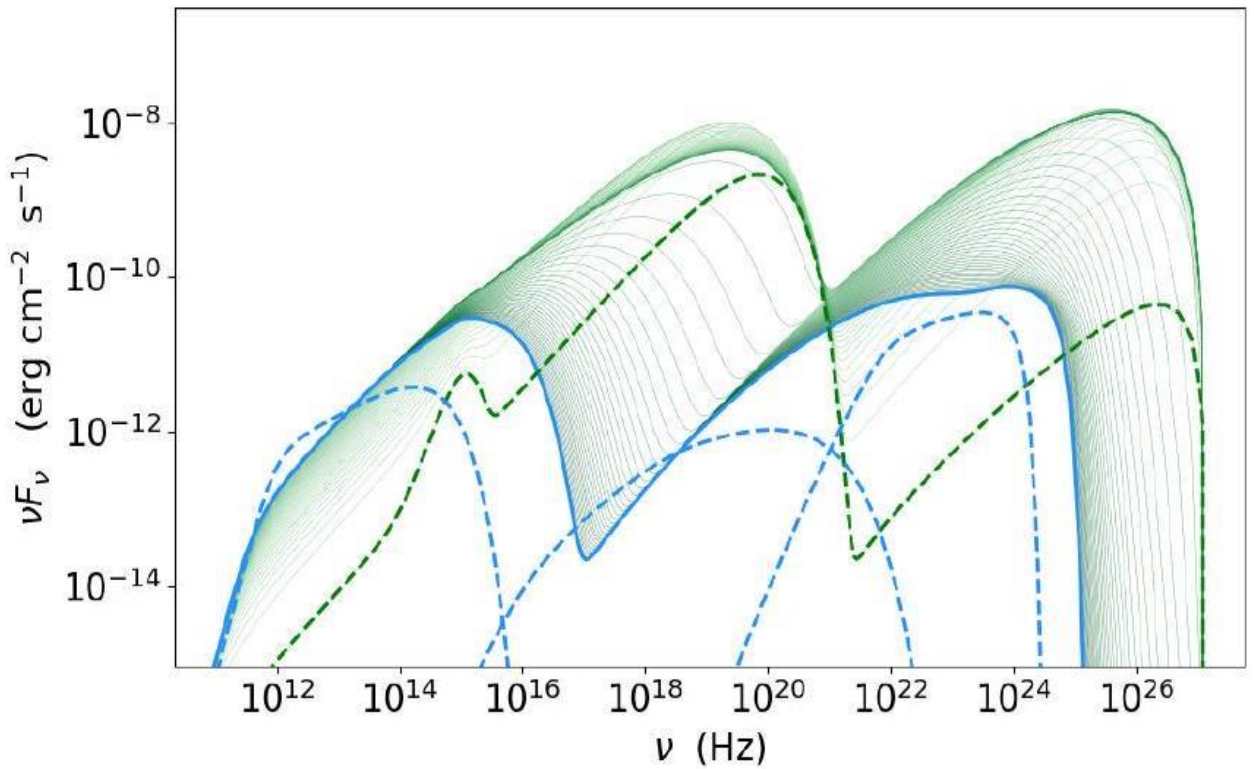


Figure 4.9: The SED evolution in time after the injection of the power-law electrons. The green dashed line shows the initial SEDs while the final one is in blue.

resulting spectrum decreases in intensity and moves to lower frequencies which is shown as a blue dashed line in Figure 4.9. The resulting spectrum is more characteristic to source emission when it is in quiescent state. Therefore, the electron spectra obtained from the fitting of SEDs can be naturally formed in time.

**JET POWER:** The modelling allows also to estimate the jet power carried by electrons ( $L_e$ ) and magnetic field ( $L_B$ ). The distribution of the luminosities computed as  $L_e = \pi c R_b^2 \Gamma^2 U_e$  and  $L_B = \pi c R_b^2 \Gamma^2 U_B$  is shown in Figure 4.7 panel e). The mean of  $L_e$  and  $L_B$  is at  $7.81 \times 10^{44} \text{ erg s}^{-1}$  and  $2.07 \times 10^{45} \text{ erg s}^{-1}$ , respectively. The distribution of  $L_B$  in the range  $2.51 \times 10^{43} - 3.48 \times 10^{46} \text{ erg s}^{-1}$  is broader than that of  $L_e$  between  $1.20 \times 10^{44} - 4.21 \times 10^{45} \text{ erg s}^{-1}$ . The large variations of  $L_B$  are mostly due to the high-amplitude changes of the synchrotron component in the SED of CTA 102. Instead, the high-amplitude increase of the  $\gamma$ -ray flux interpreted as EIC of BLR photons which would affect the electron content in the jet is compensated by increasing  $\delta$ . The distribution of  $L_e$  and  $L_B$  in Figure 4.7 panel e) shows that in some periods  $L_e/L_B < 1$ , i.e., the jet is magnetically dominated. Such a trend is observed when the synchrotron component (defined by optical/UV data) exceeds the SSC component (defined by X-ray data).

The estimated parameters allow also to assess the total kinetic energy of the jet, namely, assuming a proton-to-electron comoving number density ratio of  $N_p/N_e \simeq 0.1$ , the total kinetic luminosity defined as  $L_{\text{kin}} = L_e + L_B + L_{p,\text{cold}}$  varies from  $4.64 \times 10^{44} \text{ erg s}^{-1}$  to  $3.71 \times 10^{46} \text{ erg s}^{-1}$ . The central black hole mass in CTA 102 is estimated to be  $8.5 \times 10^8 M_\odot$  [118], so the Eddington luminosity is  $\simeq 1.1 \times 10^{47} \text{ erg s}^{-1}$ . Therefore, the kinetic power of the jet estimated in various periods is lower than the Eddington luminosity.

## 4.6 CONCLUSION

We have studied the physical processes taking place in the jet of CTA 102 using the results from long-term (fourteen-year-long) multiwavelength observations. We systematically studied the features of the source emission in optical/UV, X-ray and  $\gamma$ -ray bands as well as investigated the interband correlations. Generating the  $\gamma$ -ray light curve with the help of an adaptive binning method, the highamplitude, multiple flaring and complex variability of the source is investigated. The data accumulated during the unprecedented outburst in 2016-2017 allowed

to perform interband correlation studies which showed that the  $\gamma$ -ray variability is in correlation with the emission in the optical and X-ray bands.

The broadband emission from CTA 102 was investigated by modelling 117 high-quality SEDs assembled during the considered period. This new comprehensive approach allowed to compare and contrast jet and emitting particle properties in different states of the source emission as well as follow the dynamical changes of the physical processes governing in the jet. The one-zone model, when the low energy emission is due to synchrotron radiation of electrons while HE is due to inverse Compton scattering of both synchrotron and BLR reprocessed photons, adequately explains the source emissions in different periods, except the cases when the  $\gamma$ -ray spectrum is flat, extending to tens of GeV (2 out of 117 periods). It is found that during the flaring periods the spectrum of the emitting electrons has a harder distribution and they are effectively accelerated up to  $\gamma_{cut} = (1 - 4) \times 10^3$  as opposed to the other periods when the electrons have narrow energy distributions. By modeling also, the jet kinetic power was assessed showing that it always remained below the Eddington power.

# 5 A MULTIWAVELENGTH STUDY OF DISTANT BLAZAR PKS 0537-286

## 5.1 INTRODUCTION

The recent observations in the High Energy  $\gamma$ -ray band ( $HE > 100\text{MeV}$ ) show that the extragalactic  $\gamma$ -ray sky is dominated by the emission from Active Galactic Nuclei (AGN) of different types [53]. Interestingly, the  $\gamma$ -ray emission was observed not only from the most extreme subclass of AGNs (blazars) but also from radio galaxies [101, 102, 103, 169] and Seyfert [170]. This provides an exceptional chance to investigate the relativistic processes under different conditions.

Due to the small inclination angle and large bulk motion, the emission from blazars is significantly amplified by relativistic beaming because of which the blazars are observed even at very high redshifts. For example, in the fourth catalogue of AGNs detected by the Fermi Large Area Telescope (Fermi-LAT), the most distant blazar observed to date is GB 1508+5714 at  $z = 4.1$  [99]. At this distance, the source should be extremely powerful and extremely efficient to emit detectable electromagnetic flux. These objects typically host a black hole with a mass of  $> 10^9 M_{\odot}$ , so it is important to investigate them to understand the extreme environments around supermassive black holes. Also, for the high redshift blazars, the produced  $\gamma$ -rays during their propagation can be absorbed due to the interaction with the extragalactic background light (EBL) photons, so the observed flux could help measure the density of EBL. So, the distant blazars are ideal targets not only for studying the physical processes in the extreme conditions but also for understanding the structure and evolution of the Universe.

PKS 0537-286, at  $z = 3.104$ , is a luminous blazar included in the fourth catalog of AGNs detected by Fermi-LAT. It has been frequently observed in the X-ray band with various instruments (ASCA [171], ROSAT [172], XMM [173]) which showed that it is a very bright source with a luminosity of  $L_{x\text{-ray}} = 10^{47} \text{ erg s}^{-1}$  between 0.1-1 keV. Considering multiple observations of PKS 0537-286 with the Neil Gehrels Swift observatory carried out between 2005 and 2017 which provide data in both optical/UV and X-ray bands as well as more than ten years of data in the  $\gamma$ -ray band accumulated by Fermi-LAT, PKS 0537-286 has become

an ideal object for exploring the physics of distant blazars. This motivated us to look at the origin of the multiwavelength emission from PKS 0537-286 from a new standpoint.

## 5.2 MULTIWAVELENGTH OBSERVATIONS AND DATA ANALYSIS

The observation of blazars in the multiwavelength bands provides information not only on their emission properties in the single bands but also are crucial for understanding the physics of jets through the theoretical modelling of the observed data. The origin of the multiwavelength emission from PKS 0537-286 is studied by analysing Swift UVOT/XRT and Fermi-LAT data.

**SWIFT TELESCOPE OBSERVATIONS OF PKS 0537-286:** Swift [42] observed PKS 0537-286 16 times between 2005 and 2017. All UVOT and XRT data, except ObsID 00030816011 with an extremely short exposure (159.4sec), were extracted and analysed. The XRT exposures range from 0.11ks (ObsID 00030816011) to 14.87ks (ObsID 00035240002), and all the observations were made in the photon counting mode and no evidence of pile-up was found. The XRT data were first calibrated and cleaned with standard filtering criteria using the most recent calibration databases with the `xrtpipeline` software module distributed with the XRT Data Analysis Software (version v3.5.0). Events for the spectral analysis were selected within a 20-pixel (47") circle with the source at the centre, while the background region had an annulus with the same centre and inner and outer radii of 51 (120") and 85 pixels (200"), respectively. As the count rate in most of the observations was low, the Cash statistics [62] on ungrouped data was used. Spectral analysis was performed using XSPEC version 12.10.1. The spectra were fitted with an absorbed power-law model in the energy range from 0.3 keV to 10 keV with a neutral hydrogen column density fixed to its Galactic value of  $N_{\text{H}} = 2.22 \times 10^{20} \text{ cm}^{-2}$ . The results are given in Table 5.1: Fitting results of the data obtained by the XRT instrument on board SWIFT, where for each observation, the ObsID, date, exposure, photon index  $\Gamma$ , flux and C-stat/d.o.f. are provided. The X-ray flux (0.3-10 keV) varies in the narrow range of  $F = (3.01 - 4.58) \times 10^{-12} \text{ erg cm}^{-2} \text{ s}^{-1}$  being almost constant during the twelve years of observation of PKS 0537-286. Interestingly, the X-ray emission is characterized by a substantially hard photon index of  $< 1.3$  which implies that in  $\nu F_{\nu}$  representation the X-ray spectrum has an increasing shape. Considering only the observations

Table 5.1: Fitting results of the data obtained by the XRT instrument on board SWIFT

Obs. ID	Date	Exp. Time	$\Gamma^a$	Flux <sup>b</sup>	$C_{stat}(d. o. f.)$
<b>00030816001</b>	<i>Oct 27, 2006</i>	3040	$1.09 \pm 0.17$	$4.18 \pm 0.74$	1.07 (156)
<b>00030816003</b>	<i>Oct 30, 2006</i>	3894	$1.33 \pm 0.13$	$4.09 \pm 0.55$	1.12 (197)
<b>00030816004</b>	<i>Oct 31, 2006</i>	4425	$1.27 \pm 0.14$	$3.62 \pm 0.50$	0.97 (201)
<b>00030816005</b>	<i>Feb 10, 2008</i>	6708	$1.10 \pm 0.11$	$4.58 \pm 0.42$	1.23 (278)
<b>00030816006</b>	<i>Feb 12, 2008</i>	5274	$1.01 \pm 0.13$	$4.14 \pm 0.57$	1.11 (226)
<b>00030816007</b>	<i>Feb 14, 2008</i>	4822	$1.11 \pm 0.13$	$4.16 \pm 0.57$	1.14 (215)
<b>00030816008</b>	<i>Oct 07, 2008</i>	1593	$1.04 \pm 0.29$	$3.29 \pm 0.98$	0.68 (65)
<b>00030816009</b>	<i>Mar 12, 2010</i>	1076	$1.00 \pm 0.34$	$3.82 \pm 1.34$	0.91 (51)
<b>00030816010</b>	<i>Mar 12, 2010</i>	2018	$0.93 \pm 0.32$	$2.07 \pm 0.69$	1.28 (49)
<b>00030816012</b>	<i>Sep 06, 2011</i>	3931	$1.06 \pm 0.18$	$3.01 \pm 0.57$	0.86 (135)
<b>00035240001</b>	<i>Nov 23, 2005</i>	9038	$1.17 \pm 0.10$	$3.51 \pm 0.37$	0.87 (306)
<b>00035240002</b>	<i>Dec 8, 2005</i>	14750	$1.13 \pm 0.08$	$3.84 \pm 0.40$	1.08 (407)
<b>00036783001</b>	<i>May 17, 2007</i>	5414	$1.32 \pm 0.11$	$4.20 \pm 0.48$	1.12 (257)
<b>00036783002</b>	<i>May 10, 2017</i>	1933	$1.28 \pm 0.20$	$4.28 \pm 0.87$	1.09 (116)
<b>00036783003</b>	<i>May 12, 2017</i>	2238	$1.03 \pm 0.19$	$4.52 \pm 0.91$	0.98 (123)
<b>Swift UVOT</b>					
	U	W1	M2	B	V
<b>00030816008</b>	$20.8 \pm 1.2$	$21.5 \pm 1.8$	$21.9 \pm 4.4$	$19.7 \pm 0.4$	$19.3 \pm 0.6$
<b>00030816009</b>	$21.0 \pm 1.0$	$20.2 \pm 0.5$	$21.0 \pm 0.9$	$20.0 \pm 0.3$	$18.7 \pm 0.3$
<b>00035240002</b>	$20.8 \pm 0.1$	$22.0 \pm 2.1$	$21.3 \pm 1.1$	$19.5 \pm 0.3$	$18.8 \pm 0.3$

with counts  $> 100$ , which allow confidential estimation of the parameters, the hardest photon index is  $1.03 \pm 0.19$  observed on May 12, 2017.

The data from the Swift UVOT observations were used to estimate the fluxes of the source in the optical and UV bands. The UVOT observation takes data in six bands, UVW2 (188 nm), UVM2 (217 nm), UVW1 (251 nm), U (345 nm), B (439 nm) and V (544 nm). The source counts were extracted from an aperture of 5" radius around the source. The background counts were taken from the neighbouring circular region having a radius of 20" located close to the source region and not being contaminated with any signal from the nearby sources.

Uvotsource tool was used to convert the source counts into fluxes using the conversion factors provided in [93]. The data were corrected for dust contamination using the reddening coefficient  $E(B - V)$  from the infrared science archive<sup>23</sup>. Initially, all observations were processed and no variability in a single filter was found. For most of the observations, in several filters, the counts were not enough to measure the source magnitude and only for ObsIDs 00030816008, 00030816009 and 0003524002 five filters were available. The Swift UVOT observations of PKS 0537-286 in magnitudes for these ObsIDs are given below Table 5.1 (last lines).

**FERMI LAT OBSERVATIONS OF PKS 0537-286:** Fermi-LAT is a pair conversation telescope sensitive to the photons in the energy range from 100 MeV to 300 GeV [98]. Launched on June 11, 2008, it is always on survey mode since August 2008 and scans the entire sky every three hours, providing the deepest view of the HE  $\gamma$ -ray sky.

For this study, the publicly available Fermi-LAT data accumulated from 4th August 2008 to 4th August 2018 (ten years) were downloaded and analysed. The past 8 events in the energy range from 100 MeV to 500 GeV with the highest probability of being photons ("event class = 128 " and "evtype=3") were analysed with the Fermi Sciences Tools 1.2.1 software package. The photons from the  $12^\circ$  region centered on the  $\gamma$ -ray position of PKS 0537-286 (RA, Dec) = (84.99, -28.66) were downloaded and binned into a  $16.9^\circ \times 16.9^\circ$  square region of interest (ROI) with a stereographic projection into pixels of  $0.1^\circ \times 0.1^\circ$  and into 35 equal logarithmically-spaced energy bins using gtbin tool. The standard binned likelihood analysis was performed following the recommendation by Fermi-LAT collaboration, and the results were compared by performing the same analysis using Fermipy and Enrico python packages. The fitting model includes diffuse emission components and  $\gamma$ -ray sources within ROI (the model file is created based on the most recent 4FGL [53]). The Galactic and isotropic  $\gamma$ -ray backgrounds were modelled using the standard gll\_iem\_v06 and iso\_P8R2\_SOURCE\_V6\_v06 models. During the fit, the normalization of background models, as well as fluxes and spectral indices of the sources within ROI, are left as free parameters.

---

<sup>23</sup> <https://irsa.ipac.caltech.edu/applications/DUST/>

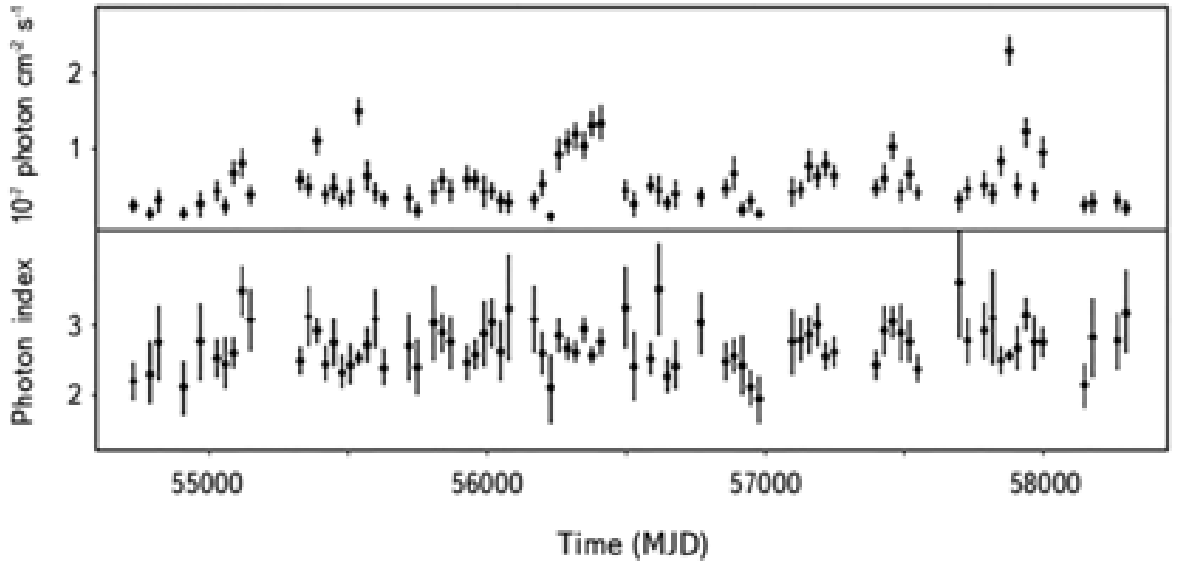


Figure 5.1: The  $\gamma$ -ray light curve and the photon index of PKS 0537-286. The light curves were calculated using 30 day bins. For clarity, the periods with the upper limits are not shown.

The time-averaged  $\gamma$ -ray spectrum of PKS 0537-286 was first modeled using a log-parabola [61] as in 4FGL then assuming a power-law shape. The latter will be used in the light-curve and the SED calculations. As when shorter periods or narrow energy intervals are used a power-law can be a good approximation of the spectrum. When log-parabola is considered, the spectrum of PKS 0537-286 is best described when  $\alpha = 2.70 \pm 0.03$  and  $\beta = 0.09 \pm 0.03$  with the corresponding integral flux of  $F_\gamma = (4.19 \pm 0.15) \cdot 10^{-8}$  photon  $\text{cm}^{-2} \text{s}^{-1}$ . The Test Statistics ( $TS$ ),  $TS = 2(\log L - \log L_0)$ , where  $L$  and  $L_0$  are the likelihoods with or without the source, is  $TS = 1824.5$  above 100 MeV, corresponding to a  $\approx 42.7\sigma$  detection significance. The  $\gamma$ -ray flux of PKS 0537-286 is impressive when considering its distance ( $z = 3.1$ ). The spectral parameters, when the power-law model is considered, are  $F_\gamma = (4.40 \pm 0.19) \times 10^{-8}$  photon  $\text{cm}^{-2} \text{s}^{-1}$  and  $\Gamma = 2.73 \pm 0.03$ . This power-law model was used to compute the spectrum of PKS 0537-286 by separately running gtlake for 6 energy bands (Figure 5.2).

The  $\gamma$ -ray flux and photon evolution in time were investigated by generating the light curves using the unbinned likelihood analysis method implemented in the gtlake tool. The flux and photon index were measured in each time interval, restricting the energy range to (0.1-300) GeV and assuming a power-law spectrum for PKS 0537-286. To reduce the uncertainties in the estimations, the photon indices of all background sources (except PKS 0537-286) are

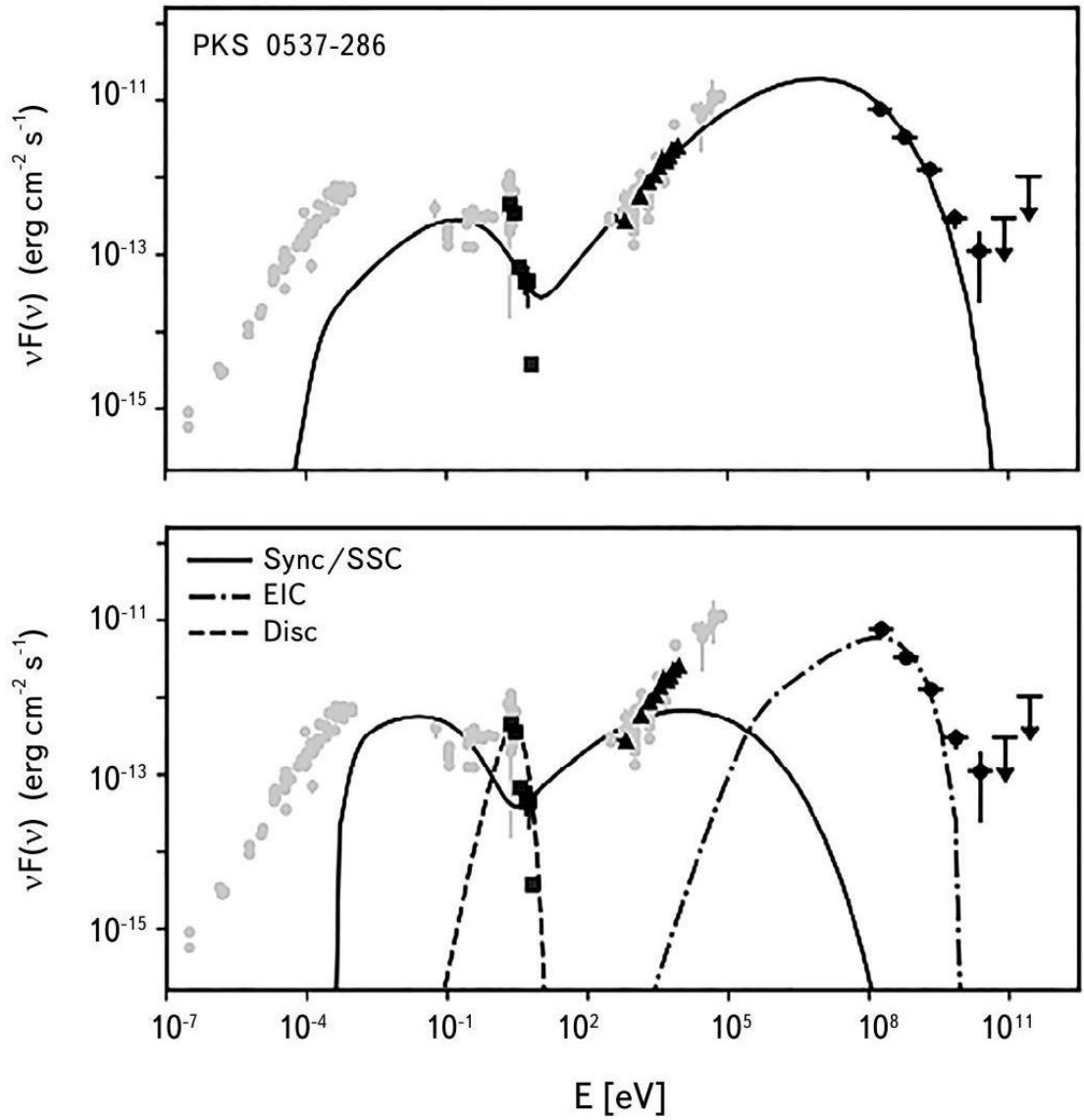


Figure 5.2: The broadband SED of PKS 0537-286. *Upper panel:* The modeling considering only the SSC model. *Lower panel:* The modeling considering both synchrotron (SSC) and external photons (EIC).

fixed to the best guess values obtained in the analysis of the entire 10 years of data. Since no variability is expected for the background diffuse emission, the normalization of both background components is also fixed to the values obtained for the whole period.

Initially, the light curves were generated using a 7-day time binning. There is clear evidence of flux variation in short time scales, although in many periods only upper limits  $TS < 16$  are derived. The highest flux measured in week scale is  $(6.23 \pm 0.56) \cdot 10^{-7}$  photon  $\text{cm}^{-2} \text{s}^{-1}$ , which nearly 15 times exceeds the average flux reported above. This flux was observed during the major flare that occurred around MJD 57874. However, the light curve contains a large number of periods with only upper limits, which prevents the detailed study of the variability

in short time scales. For a more quantitative investigation of the evolution of the  $\gamma$ -ray flux in time, the light curve is generated with a month time binning (Figure 5.1). Again, a clear indication of flux variability is evident with several times when the flux was above  $10^{-7}$  photon  $\text{cm}^{-2} \text{s}^{-1}$ . One of such periods starts from MJD 56272 and lasts for 30 days. The highest flux corresponds to  $(2.32 \pm 0.19) \cdot 10^{-7}$  photon  $\text{cm}^{-2} \text{s}^{-1}$  observed during the major flare mentioned above. The photon index does not show significant changes, most of the time it varying in the range of  $> 2.5$ . These analyses show that the  $\gamma$ -ray emission from PKS 0537-286 is variable in both short and long-time scales.

### 5.3 BROADBAND SEDs

The broadband observations of blazars are unique tools to explore their physics. The data ranging from radio to VHE  $\gamma$ -ray band can allow to probe the physical processes at large energy intervals and to estimate several important parameters of the jet. The multiwavelength archival data from the observation of PKS 0537-286 are shown in Figure 5.2 with grey color. As has been discussed in the previous section, there is no variability in the X-ray band and the data are not enough for searching variability in the optical/UV bands. To increase the statistics, all the Swift observations were merged and analysed which provides the fluxes in the mentioned bands. These data are shown in Figure 5.2 with squares and triangles respectively. Since there are no simultaneous multiwavelength data available for testing PKS 0537-286 jet physics in different periods, and as the main purpose of the current study is to estimate the main parameters of the jet of PKS 0537-286 in the average state, even if the  $\gamma$ -ray emission varies in some periods, the  $\gamma$ -ray flux averaged over 10 years of observations was used in the modelling (black circles in Figure 5.2).

**MODELING OF THE SED:** The SED shown in Figure 5.2 has a typical double peaked structure. The low-energy peak (from radio to optical/UV) is most likely due to the non-thermal synchrotron emission of relativistic electrons, while the second component can be produced from the Inverse Compton (IC) scattering of low energy synchrotron photons (Synchrotron Self Compton; SSC) [9, 8, 7] or scattering of photons external to the jet (External Compton (EIC)). The external photon field can be either the photons reflected by Broad Line Region (BLR) clouds [12] or by photons from a dusty torus [11, 10]. Domination

of one of the components mostly depends on the localization of the emitting region, which is unknown. Thus, in the modelling, both photons' fields are considered for modelling the HE component in the SED of PKS 0537-286.

In the modelling, it is assumed that the multiwavelength emission is produced in a single zone (one-zone scenarios). The emission region is a spherical blob moving relativistically along the jet with a bulk Lorentz factor of  $\Gamma_{jet}$ . The produced emission will be Doppler boosted with  $\delta = \Gamma_{jet}(1 - \beta \cos \theta)^{-1}$ , where  $\theta$  is the angle between the direction of observation and the axis of the jet. In this work, we assume  $\delta = 20$ , which is typical for the bright blazars. The blob has tangled magnetic field with the magnitude of  $B$  and it is filled with nonthermal electrons which have a power-law with exponential cut-off distribution given by

$$N_e(\gamma_e) = N_0(\gamma_e)^{-\alpha} \exp\left[-\frac{\gamma_e}{\gamma_{cut}}\right] \quad (6.1)$$

between  $\gamma_{min}$  and  $\gamma_{max}$ , and  $N_0$  defines the total energy of the electrons  $U_e$ . The electrons with the energy distribution given by Equation 6.1, under the magnetic field will produce synchrotron emission which can explain the observed low energy component.

The produced synchrotron photons can serve as the target photon field for the IC scattering. In addition to these photons, it is assumed, that the emission region is within the broad BLR and the disc photons reflected from the BLR clouds can also be IC up-scattered and explain the observed HE component. The density of the BLR photons,  $u_{BLR} = \tau L_{disc}/4\pi R_{BLR}^2$ , depends on the disc luminosity  $L_{disc}$ , on the fraction of the photons reflected from BLR ( $\tau = 0.1$ ) and on the radius of BLR ( $R_{BLR}$ ) for which a relation of  $R_{BLR} = 10^{17}(L_{disc}/10^{45})$  cm is assumed [38]. The disc luminosity is constrained by fitting a blackbody to the UV excess (Figure 5.2), which is likely caused by direct thermal emission from the accretion disc.

Using the observed data, additional constraints on the model parameters can be derived. For example, knowing the variability, the limit on the blob radius can be imposed from the relation  $R \leq \delta ct/(1+z) = 6.3 \cdot 10^{16}$  cm. Also, knowing the peak of the low and high energy components, additional constraints on the magnetic field and blob radius can be derived. All the parameters constrained from the observations are given as initial values for the parameter

search, and through “MINUIT” optimization parameters best describing the data are obtained<sup>24</sup>.

**MODELING RESULTS:** The SED modelling results are shown in Figure 5.2. The radio data are treated as upper limits during the modelling, as the emission in this band is produced from the low-energy electrons, which can propagate longer and are perhaps from more extended regions. Initially, the SED is modelled assuming that only synchrotron photons are inverse Compton up-scattered to higher energies, neglecting the external photons (solid line in Figure 5.2 upper panel). As the X-ray data are defining the low-energy tail of the SSC components, it allows to estimate  $\alpha = 1.48$ . For a softer power-law index of electrons, the rising shape of the X-ray data cannot be reproduced. The cut-off energy of electrons is  $\gamma_{cut} = 5138.4$  well defined by the peak of the HE component. The minimum energy of the electrons was estimated to be at  $\gamma_{min} = 7.34$ , and the magnetic field  $B = 44.8$  mG to have an energy density of  $U_B = 8.0 \cdot 10^{-5}$  erg cm<sup>-3</sup>. The modeling also allows to estimate the jet power in the form of the magnetic field and electron kinetic energy, calculated by  $L_B = \pi c R_b^2 \Gamma^2 U_B$  and  $L_e = \pi c R_b^2 \Gamma^2 U_e$ , respectively. The jet power in electrons is and that in the magnetic field is  $1.05 \cdot 10^{46}$  erg s<sup>-1</sup>. The jet is strongly particle dominated, required to explain the dominance of the HE component.

The results of the SED modelling when both internal and external photons are considered (SSC+EIC) is shown in Figure 5.2 (lower panel). The direct disc emission peaking at UV band (dashed line) is shown with a blackbody luminosity  $4.7 \cdot 10^{46}$  erg s<sup>-1</sup> found by data fitting. In this case, the IC scattering of the synchrotron photons explains the observed X-ray flux while the  $\gamma$ -ray data are due to IC up-scattering of BLR photons. Since the averaged energy of BLR reflected photons exceeds the synchrotron ones, this results in lower cut-off energy of the electrons  $\gamma_{cut} = 694.6$ . In this case, again the X-ray data (at least lower part) are modelled by SSC which defines the power-law index of the electrons  $\alpha = 1.95$ . We note that a harder power-law index will better explain the hard X-ray data but it will increase also the energy of electrons and the predicted emission in the  $\gamma$ -ray band will overshoot the observed  $\gamma$ -ray data. The estimated magnetic field  $B = 0.81$  G is higher than in the case of pure SSC modeling

---

<sup>24</sup> The fit is done using JetSet package (<https://jetset.readthedocs.io/en/latest/>).

yielding to  $U_e/U_B = 28$ , which makes the system closer to the equipartition condition ( $U_e/U_B = 1$ ). The jet energy carried by particles (electrons) and the magnetic field corresponds to  $1.55 \cdot 10^{45} \text{ erg s}^{-1}$  and  $5.51 \cdot 10^{43} \text{ erg s}^{-1}$ , respectively.

## 5.4 DISCUSSION AND CONCLUSION

We report on the results of the multiwavelength observations of PKS 0537-286. Being among the most distant blazars observed in the  $\gamma$ -ray band ( $z = 3.1$ ), PKS 0537-286 is an interesting target not only for investigating the physics of blazars in general but also it can provide information on the environment of supermassive black holes in the early Universe.

Swift XRT observations of PKS 0537-286 in different years show that its X-ray emission is nearly constant, changing in a narrow interval of  $F_{x\text{-ray}} = (3.01 - 4.58) \cdot 10^{-12} \text{ erg cm}^{-2} \text{ s}^{-1}$ . The X-ray emission is characterized by a remarkably hard photon index,  $\Gamma_{x\text{-ray}} \leq 1.3$  which indicates that the second component in the SED, although having a peak below the  $\gamma$ -ray band, energetically dominates. In the Swift UVOT observations, all filters are not always available which prevents detailed variability studies in the optical band. In the available filters, the flux was estimated to be of the order of  $\approx 10^{-12} \text{ erg cm}^{-2} \text{ s}^{-1}$  which is the same order as the reported archival flux of PKS 0537-286. Though its large distance (26.9 Gpc), PKS 0537-286 is a bright source in the  $\gamma$ -ray band. Its averaged  $\gamma$ -ray spectrum is best described with a log-parabolic model with  $\alpha = 2.70 \pm 0.0$ ,  $\beta = 0.09 \pm 0.03$  and  $F_\gamma = (4.19 \pm 0.15) \times 10^{-8} \text{ photon cm}^{-2} \text{ s}^{-1}$ . The temporal analyses of the  $\gamma$ -ray data show that the source is variable both in short and long-time scales. For example, during a week around MJD 57874, the source flux significantly increased up to  $(6.23 \pm 0.56) \cdot 10^{-7} \text{ photon cm}^{-2} \text{ s}^{-1}$  with a photon index of  $2.53 \pm 0.09$ . Using the distance of PKS 0537-286, the averaged flux corresponds to  $L_\gamma = 1.44 \cdot 10^{48} \text{ erg s}^{-1}$  which increases to  $L_\gamma = 2.46 \cdot 10^{49} \text{ erg s}^{-1}$  during the flare. Yet, considering  $\delta = 20$ , the total power emitted in the  $\gamma$ -ray band in the proper frame of the jet is  $L_{em,\gamma} = L_\gamma/2\delta^2 = 1.8 \cdot 10^{45} \text{ erg s}^{-1}$  during the quiescent state and  $L_{em,\gamma} = 3.1 \cdot 10^{46} \text{ erg s}^{-1}$  during the flare.

The multiwavelength SED of PKS 0537-286 was modelled within one-zone synchrotron/SSC and SSC+EIC scenarios. When only the synchrotron photons are considered for the IC scattering, the data can be reproduced when the energy distribution of the emitted

nonthermal electrons has a hard power-law index  $\alpha = 1.48$  which extends up to  $\gamma_{cut} = 5138.4$ . As the second peak energetically dominates, the emission region in the jet should be strongly particle dominated  $U_e/U_B = 2.4 \cdot 10^4$  and the total luminosity of the jet  $\approx 10^{46} \text{ erg s}^{-1}$  be carried by the particles. Alternatively, when the contribution from BLR reflected photons is considered, the required parameters are more relaxed. For example,  $\alpha = 1.95$ , and  $\gamma_{cut} = 694.6$  the system is not far from the equipartition condition  $U_e/U_B = 28$ . This modeling has an advantage considering the required total jet power (the total luminosity of the jet is  $\approx 1.60 \cdot 10^{45} \text{ erg s}^{-1}$ ) but it fails to well reproduce the observed hard X-ray data. We note, however, that the luminosity estimated in the previous case is well within the range of luminosities usually estimated for FSRQs.

The multiwavelength studies of distant blazar PKS 0537-286 show that it is a powerful emitter in the X-ray and  $\gamma$ -ray bands. The integrated luminosity of these components exceeds that of the low-energy component (from radio to optical bands). Through theoretical modelling of the SED several parameters were constrained which allowed a quantitative evaluation of the source parameters/properties. Considering the significant number ( $> 100$ ) of high redshift blazars ( $z > 2.0$ ) detected in the HE  $\gamma$ -ray band, their detailed multiwavelength study can shed light on the understanding of the objects in the distant Universe.

## CONCLUSION

The investigation of the processes taking place in the relativistic jets of blazars is among the most actively discussed topics of modern astrophysics, there are still several open questions in the understanding of the physics jets. Even if the morphology of jets can be studied in sensitive observations, the launching, collimation, and propagation of jets remain is still unclear. Moreover, once the jet is formed, the exact mechanism which accelerates the particles up to VHEs is also unclear.

In the present thesis, an attempt was made to understand the origin of blazar emission through extensive data analysis. In particular, for the frequently observed blazars all available Swift XRT and UVOT data was analysed, and detailed spectral and temporal analyses was performed. This allowed collection of an unprecedented amount of data necessary to study individual blazars, as well as compare and contrast the properties of different blazar types (LBLs, IBLs, and HBLs). For two representative blazars which were frequently observed in the X-ray and optical/UV band, the correlation of the emission in the different bands was investigated and used to put constraints on the different emission components. Using the multi-wavelength data from the observations of CTA 102, the dynamical changes of synchrotron and inverse Compton components were investigated, which is crucial for understanding the processes dominating in its jet. The emission from PKS 0537-286 jet was studied, to estimate the X-ray and optical UV properties of powerful blazars.

The results obtained in this thesis, can be used to study the population of blazars (X-ray and optical/UV database), study the correlation between blazar emission in different bands as well as test particle acceleration and emission processes in relativistic plasma.

## REFERENCES

- [1] U. C. Megan and P. Padovani, "Unified Schemes for Radio-Loud Active Galactic Nuclei," *Publications of the Astronomical Society of the Pacific*, vol. 107, p. 803, 1995.
- [2] M. Ackermann and e. al., "Multiwavelength Evidence for Quasi-periodic Modulation in the Gamma-Ray Blazar PG 1553+113," *The Astrophysical Journal*, vol. 813, p. L41, 2015.
- [3] H. X. Ren, M. Cerruti and N. Sahakyan, "Quasi-periodic oscillations in the  $\gamma$ -ray light curves of bright active galactic nuclei.," *arXiv e-prints*, p. arXiv:2204.13051, 2022.
- [4] N. Sahakyan and P. Giommi, "The strange case of the transient HBL blazar 4FGL J1544.3-0649," *Monthly Notices of the Royal Astronomical Society*, vol. 502, pp. 836-844, 2021.
- [5] N. Sahakyan, "Investigation of the  $\gamma$ -ray spectrum of CTA 102 during the exceptional flaring state in 2016-2017," *Astronomy and Astrophysics*, vol. 635, p. A25, 2020.
- [6] Y.-L. Chang and C. B. a. P. Giommi, "The Open Universe VOU-Blazars tool," *Astronomy and Computing*, vol. 30, no. 2213-1337, pp. 100-350, 2020.
- [7] G. Ghisellini, L. Maraschi and A. Treves, "Inhomogeneous synchrotron-self-compton models and the problem of relativistic beaming of BL Lac objects.," *Astronomy and Astrophysics*, vol. 146, pp. 204-212, 1985.
- [8] S. Bloom and A. Marscher, "An Analysis of the Synchrotron Self-Compton Model for the Multi-Wave Band Spectra of Blazars," *Astrophysical Journal*, vol. 461, p. 657, 1996.
- [9] L. Maraschi, G. Ghisellini and A. Celotti, "A Jet Model for the Gamma-Ray-emitting Blazar 3C 279," *Astrophysical Journal*, vol. 397, p. L5, 1992.
- [10] M. Blazejowski, M. Sikora, R. Moderski and G. Madejski, "Comptonization of Infrared Radiation from Hot Dust by Relativistic Jets in Quasars," *Astrophysical Journal*, vol. 545, pp. 107-116, 2000.

- [11] G. Ghisellini and F. Tavecchio, "Canonical high-power blazars," *Monthly Notices of the Royal Astronomical Society*, vol. 397, pp. 985-1002, 2009.
- [12] M. Sikora, M. Begelman and M. Rees, "Comptonization of Diffuse Ambient Radiation by a Relativistic Jet: The Source of Gamma Rays from Blazars?," *Astrophysical Journal*, vol. 421, p. 153, 1994.
- [13] A. Mücke and R. J. Protheroe, "A proton synchrotron blazar model for flaring in Markarian 501," *Astroparticle Physics*, vol. 15, p. 121, 2001.
- [14] K. Mannheim, "The proton blazar," *Astronomy and Astrophysics*, vol. 269, p. 67, 1993.
- [15] K. Mannheim and P. L. Biermann, "Photomeson production in active galactic nuclei.," *Astronomy and Astrophysics*, vol. 221, p. 211, 1989.
- [16] A. Mücke, R. J. Protheroe, R. Engel, J. P. Rachen and T. Stanev, "BL Lac objects in the synchrotron proton blazar model," *Astroparticle Physics*, vol. 18, p. 593, 2003.
- [17] M. Böttcher, A. Reimer, K. Sweeney and A. Prakash, "Leptonic and Hadronic Modeling of Fermi-detected Blazars," *The Astrophysical Journal*, vol. 768, p. 54, 2013.
- [18] M. Petropoulou and A. Mastichiadis, "Bethe-Heitler emission in BL Lacs: filling the gap between X-rays and  $\gamma$ -rays," *Monthly Notices of the Royal Astronomical Society*, vol. 447, p. 36, 2015.
- [19] S. Gasparyan, D. Bégué and N. Sahakyan, "Time-dependent lepto-hadronic modelling of the emission from blazar jets with SOPRANO: the case of TXS 0506 + 056, 3HSP J095507.9 + 355101, and 3C 279," *Monthly Notices of the Royal Astronomical Society*, vol. 509, p. 2102, 2022.
- [20] IceCube Collaboration, "Neutrino emission from the direction of the blazar TXS 0506+056 prior to the IceCube-170922A alert.," *Science*, vol. 361, p. 147, 2018.
- [21] IceCube Collaboration, "Multimessenger observations of a flaring blazar coincident with high-energy neutrino IceCube-170922A," *Science*, vol. 361, 2018.

- [22] P. Padovani and e. al., "Dissecting the region around IceCube-170922A: the blazar TXS 0506+056 as the first cosmic neutrino source," *Monthly Notices of the Royal Astronomical Society*, vol. 480, p. 192, 2018.
- [23] S. Ansoldi, "The Blazar TXS 0506+056 Associated with a High-energy Neutrino: Insights into Extragalactic Jets and Cosmic-Ray Acceleration," *The Astrophysical Journal*, vol. 863, p. L10, 2018.
- [24] A. Keivani, "A Multimessenger Picture of the Flaring Blazar TXS 0506+056: Implications for High-energy Neutrino Emission and Cosmic-Ray Acceleration," *The Astrophysical Journal*, vol. 864, p. 84, 2018.
- [25] K. Murase, F. Oikonomou and M. Petropoulou, "Blazar Flares as an Origin of High-energy Cosmic Neutrinos?," *The Astrophysical Journal*, vol. 865, p. 124, 2018.
- [26] N. Sahakyan, "Lepto-hadronic  $\gamma$ -Ray and Neutrino Emission from the Jet of TXS 0506+056.," *The Astrophysical Journal*, vol. 866, p. 109, 2018.
- [27] C. Righi, F. Tavecchio and L. Pacciani, "A multiwavelength view of BL Lac neutrino candidates.," *Monthly Notices of the Royal Astronomical Society*, vol. 484, p. 2067, 2019.
- [28] M. Cerruti, A. Zech, C. Boisson, G. Emery, S. Inoue and J. P. Lenain, "Leptohadronic single-zone models for the electromagnetic and neutrino emission of TXS 0506+056.," *Monthly Notices of the Royal Astronomical Society*, vol. 483, p. L12, 2019.
- [29] N. Sahakyan, "Origin of the multiwavelength emission of PKS 0502+049.," *Astronomy and Astrophysics*, vol. 622, p. A144, 2019.
- [30] S. Gao, A. Fedynitch, W. Winter and M. Pohl, "Modelling the coincident observation of a high-energy neutrino and a bright blazar flare," *Nature Astronomy*, vol. 3, p. 88, 2019.
- [31] N. Sahakyan and e. al., "A multi-messenger study of the blazar PKS 0735+178: a new major neutrino source candidate.," *arXiv e-prints*, p. arXiv:2204.05060, 2022.

- [32] P. Padovani and P. Giommi, "The Connection between X-Ray-- and Radio-selected BL Lacertae Objects.," *The Astrophysical Journal*, vol. 444, p. 567, 1995.
- [33] A. A. Abdo and e. al., "The Spectral Energy Distribution of Fermi Bright Blazars.," *The Astrophysical Journal*, vol. 716, p. 30, 2010.
- [34] P. Giommi and P. Padovani, "Astrophysical Neutrinos and Blazars.," *Universe*, vol. 7, p. 492, 2021.
- [35] S.v., "Collins Dictionary of Astronomy," [Online]. Available: <https://encyclopedia2.thefreedictionary.com/synchrotron+emission>. [Accessed 5 September 2022].
- [36] G. Blumenthal and R. Gould, "Bremsstrahlung, Synchrotron Radiation, and Compton Scattering of High-Energy Electrons Traversing Dilute Gases," *Reviews of Modern Physics*, vol. 42, pp. 237-271, 1970.
- [37] A. Bennun, "High Energy Dimensioning the Quantum Space-Time of the Electron," 2020.
- [38] C. Dermer and G. Menon, "High Energy Radiation from Black Holes: Gamma Rays, Cosmic Rays, and Neutrinos," 2009.
- [39] M. Sikora, L. Stawarz, R. Moderski, K. Nalewajko and G. Madejski, "Constraining Emission Models of Luminous Blazar Sources," *Astrophysical Journal*, vol. 704, pp. 38-50, 2009.
- [40] M. Hayashida, G. Madejski, K. Nalewajko, M. Sikora and e. al., "The Structure and Emission Model of the Relativistic Jet in the Quasar 3C 279 Inferred from Radio to High-energy  $\gamma$ -Ray Observations in 2008-2010," *Astrophysical Journal*, vol. 754, p. 114, 2012.
- [41] M. Nenkova, M. Sirocky, R. Nikutta, Ž. Ivezić and M. Elitzur, "AGN Dusty Tori. II. Observational Implications of Clumpiness," *Astrophysical Journal*, vol. 685, pp. 160-180, 2008.
- [42] N. Gehrels, G. Chincarini, P. Giommi and K. O. M. e. al., "Erratum: The swift Gamma-ray burst mission," *Astrophysical Journal*, vol. 621, p. 558, 2005.

- [43] S. Barthelmy, L. Barbier, J. Cummings, E. Fenimore and e. al., "The Burst Alert Telescope (BAT) on the SWIFT Midex Mission," *Space Science Reviews*, vol. 120, pp. 143-164, 2005.
- [44] N. D. Burrows, J. Hill, J. Nousek and e. al., "The Swift X-Ray Telescope," *Scientific Studies of Reading*, vol. 120, pp. 165-195, 2005.
- [45] C. Pagani, A. Beardmore, A. Abbey, C. Mountford and e. al., "Recovering Swift-XRT energy resolution through CCD charge trap mapping," *Astronomy & Astrophysics*, vol. 534, p. A20, 2011.
- [46] P. Roming, T. Kennedy, K. Mason, J. Nousek and e. al., "The Swift Ultra-Violet/Optical Telescope," *Space Science Reviews*, vol. 120, pp. 3-4, 2005.
- [47] A. Breeveld, P. Curran, E. Hoversten, S. Koch and e. al., "Further calibration of the Swift ultraviolet/optical telescope," *Monthly Notices of the Royal Astronomical Society*, vol. 406, pp. 1687-1700, 2010.
- [48] [Online].[https://fermi.gsfc.nasa.gov/ssc/data/analysis/documentation/Cicerone/Cicerone\\_Introduction/LAT\\_overview.html](https://fermi.gsfc.nasa.gov/ssc/data/analysis/documentation/Cicerone/Cicerone_Introduction/LAT_overview.html).
- [49] A. A. Abdo and e. al., "Fermi large area telescope observations of the cosmic-ray induced  $\gamma$ -ray emission of the Earth's atmosphere," *Physical Review D*, vol. 80, p. 122004, 2009.
- [50] A. A. Moiseev, J. F. Ormes, Hartman, J. R. C., M. J. W. T. E. and D. J. Thompson, "Observation and simulations of the backslash effects in high-energy  $\gamma$ -ray telescopes containing a massive calorimeter.," *Astroparticle Physics*, vol. 22, p. 275, 2004.
- [51] W. B. Atwood and e. al., "New Fermi-LAT Event Reconstruction Reveals More High-energy Gamma Rays from Gamma-Ray Bursts," *The Astrophysical Journal*, vol. 774, p. 76, 2013.
- [52] J. Mattox, D. Bertsch, J. Chiang, B. Dingus and e. al., "The Likelihood Analysis of EGRET Data," *Astrophysical Journal*, vol. 461, p. 396, 1996.

- [53] S. Abdollahi, F. Acero, M. Ackermann, M. Ajello and e. al., "Fermi Large Area Telescope Fourth Source Catalog," *Astrophysical Journal Supplement Series*, vol. 247, p. 33, 2020.
- [54] J. Ballet, T. Burnett, S. Digel and B. Lott, "Fermi Large Area Telescope Fourth Source Catalog Data Release 2," *arXiv e-prints*, p. arXiv:2005.11208, 2020.
- [55] T. C. Consortium, *Science with the Cherenkov Telescope Array*, World Scientific Publishing, 2019.
- [56] G. L. Mura, G. Chiaro, R. Conceição, A. De-Angelis and e. al., "Detection of very-high-energy gamma-ray transients with monitoring facilities," *Monthly Notices of the Royal Astronomical Society*, pp. 3142-3148, 2020.
- [57] E. Massaro, A. Maseli, C. Leto and e. al., "The 5th edition of the Roma-BZCAT.," *Astrophysics and Space Science*, vol. 357, p. 75, 2015.
- [58] Y. -L. Chang, B. Arsioli, P. Giommi, P. Padovani and C. ~. Brandt, "The 3HSP catalogue of extreme and high-synchrotron peaked blazars.," *American Academy of Pediatrics*, vol. 632, p. A77, 2019.
- [59] S. Vaughan, M. Goad, A. Beardmore, P. Osborne and e. al., "Swift Observations of the X-Ray-Bright GRB 050315," *Astrophysical Journal*, vol. 638, pp. 920-929, 2006.
- [60] K. Arnaud, "XSPEC: The First Ten Years," vol. 101, p. 17, 1996.
- [61] E. Massaro, A. Tramacere, M. Perri, P. Giommi and G. Tosti, "Log-parabolic spectra and particle acceleration in blazars. III. SSC emission in the TeV band from Mkn501," *Astronomy & Astrophysics*, vol. 448, pp. 861-871, 2006.
- [62] W. Cash, "Parameter estimation in astronomy through application of the likelihood ratio.," *Astrophysical Journal*, pp. 939-47, 1979.
- [63] P. J. Humpfrey, W. Liu and D. A. Buote, " $\chi^2$  and Poissonian Data: Biases Even in the High-Count Regime and How to Avoid Them," *Astrophysical Journal*, vol. 693, pp. 822-829, 2009.

- [64] P. Giommi, C. H. Brandt, U. B. d. Almeida, A. M. T. Pollock and e. al., "Open Universe for Blazars: a new generation of astronomical products based on 14 years of Swift-XRT data," *Astronomy & Astrophysics*, vol. 631, p. A116, 2019.
- [65] P. Giommi, Y. Chang, S. Turriziani, T. Glauch and e. al., "Open Universe survey of Swift-XRT GRB fields: Flux-limited sample of HBL blazars.," *Astronomy & Astrophysics*, vol. 642, p. A141, 2020.
- [66] B. Kapanadze, D. Dorner, S. Vercellone, P. Romano, S. Kapanadze and T. Mdzinarishvili, "A recent strong X-ray flaring activity of 1ES 1959+650 with possibly less efficient stochastic acceleration," *Monthly Notices of the Royal Astronomical Society*, vol. 461, no. 1, pp. L26-L31, 2016.
- [67] M. Morini, L. Chiappetti, D. Maccagni, L. Maraschi and e. al., "X-Ray Variability of the BL Lacertae Object PKS 2155-304 in the 0.1--6 keV Range," *Astrophysical Journal* , vol. 306, p. L71, 1986.
- [68] I. George, R. Warwick and G. Bromage, "X-ray and ultraviolet observations of Markarian 421.," *Monthly Notices of the Royal Astronomical Society*, vol. 232, pp. 793-88, 1998.
- [69] P. Giommi, P. Barr, B. Garilli, D. Maccagni and A. M. T. Pollock, "A Study of BL Lacertae--Type Objects with EXOSAT. I. Flux Correlations, Luminosity, Variability, and Spectral Variability," *Astrophysical Journal*, vol. 356, p. 432, 1990.
- [70] P. Grandi and G. G. C. Palumbo, "Jet and Accretion-Disk Emission Untangled in 3C 273," *Science*, vol. 306, pp. 998-1002, 2004.
- [71] B. Kapanadze, D. Dorner, S. Vercellone, P. Romano and e. al., "The second strong X-ray flare and multifrequency variability of 1ES 1959+650 in 2016 January-August," *Monthly Notices of the Royal Astronomical Society*, vol. 473, pp. 2542-2564, 2018.
- [72] B. Kapanadze, A. Guruchumelia, D. Dorner, S. Vercellone and e. al., "Swift Observations of Mrk 421 in Selected Epochs. III. Extreme X-Ray Timing/Spectral Properties and Multiwavelength Lognormality during 2015 December-2018 April," *Astrophysical Journal Supplement Series*, vol. 247, p. 27, 2020.

- [73] B. Kapanadze, D. Dorner, S. Vercellone, P. Romano and e. al., "X-Ray Flaring Activity of MRK 421 in the First Half of 2013," *Astrophysical Journal*, vol. 831, p. 102, 2019.
- [74] Y. Wang, Y. Xue, S. Zhu and J. Fan, "Systematic Investigation of X-Ray Spectral Variability of TeV Blazars during Flares in the RXTE Era," *Astrophysical Journal*, vol. 867, p. 68, 2018.
- [75] B. Kapanadze, S. Vercellone, P. Romano and P. Hughes, "Swift Observations of Mrk 421 in Selected Epochs. I. The Spectral and Flux Variability in 2005-2008," *Astrophysical Journal*, vol. 854, p. 66, 2018.
- [76] B. Kapanadze, D. Dorner, P. Romano, S. Vercellone and e. al., "Mrk 421 after the Giant X-Ray Outburst in 2013," *Astrophysical Journal*, vol. 848, p. 103, 2017.
- [77] B. Kapanadze, D. Dorner, S. Vercellone, P. Romano and e. al., "Strong X-Ray and Multiwavelength Flaring Activity for 1ES 1959+650, 2016 August-2017 November," *Astrophysical Journal*, vol. 238, p. 13, 2018.
- [78] P. Giommi, P. Padovani and E. Perlman, "Detection of exceptional X-ray spectral variability in the TeV BL Lac 1ES 2344+514," *Monthly Notices of the Royal Astronomical Society*, vol. 317, pp. 743-749, 2000.
- [79] E. Pian, G. Vacanti, G. Tagliaferri, G. Ghisellini and e. al., "BeppoSAX Observations of Unprecedented Synchrotron Activity in the BL Lacertae Object Markarian 501," *Astrophysical Journal Letters*, vol. 492, pp. L17-L20, 1998.
- [80] P. Giommi, S. Colafrancesco, S. Cutini, P. Marchegiani and e. al., "AGILE and Swift simultaneous observations of the blazar S50716+714 during the bright flare of October 2007," *Astronomy and Astrophysics*, vol. 487, pp. L49-L52, 2008.
- [81] D. Xiong, J. Bai, J. Fan, D. Yan and e. al., "Multicolor Optical Monitoring of the Blazar S5 0716+714 from 2017 to 201," *Astrophysical Journal Supplement Series*, vol. 247, p. 49, 2020.
- [82] T. Morokuma, Y. Utsumi, K. Ohta, M. Yamanaka and e. al., "Follow-up observations for IceCube-170922A: Detection of rapid near-infrared variability and intensive

- monitoring of TXS 0506+056," *Publications of the Astronomical Society of Japan*, vol. 73, pp. 25-43, 2021.
- [83] E. Bonning, C. M. Urry, C. Bailyn, M. Buxton and e. al., "SMARTS Optical and Infrared Monitoring of 12 Gamma-Ray Bright Blazars," *Astrophysical Journal*, vol. 756, p. 13, 2012.
- [84] W. Voges, B. Aschenbach, T. Boller, H. Brauning and e. al., "The ROSAT all-sky survey bright source catalogue," *Astronomy & Astrophysics*, vol. 349, pp. 389-405, 1999.
- [85] J. Biteau, E. Prandini, L. Costamante, M. Lemoine, P. Padovani, E. Pueschel, E. Resconi, F. Tavecchio, A. Taylor and A. Zech, "Progress in unveiling extreme particle acceleration in persistent astrophysical jets," *Nature Astronomy*, vol. 4, pp. 124-131, 2020.
- [86] S. Ciprini, C. Cheung, D. Kocevski, J. Chiang, F. L. Collaboration and S. ~. Shore, "Fermi LAT detection and Swift X-ray follow-up of a new gamma-ray/X-ray transient source Fermi J1544-0649 (Swift 154419.7-064915)," *The Astronomer's Telegram*, vol. 10482, p. 1, 2017.
- [87] A. Merloni, P. Predehl, W. Becker, H. Borhinger and e. al., "eROSITA Science Book: Mapping the Structure of the Energetic Universe," *arXiv e-prints*, p. arXiv:1209.3114, 2012.
- [88] A. Merloni, K. Nandra and P. Predehl, "eROSITA's X-ray eyes on the Universe," *Nature Astronomy*, vol. 4, pp. 634-636, 2020.
- [89] MAGIC Collaboration, "A fast, very-high-energy  $\gamma$ -ray flare from BL Lacertae during a period of multi-wavelength activity in June 2015," *Astronomy & Astrophysics*, vol. 623, p. A175, 2019.
- [90] M. Ackermann, R. Anantua, K. Asano, L. Baldini and e. al., "Minute-timescale  $>100$  MeV  $\gamma$ -Ray Variability during the Giant Outburst of Quasar 3C 279 Observed by Fermi-LAT in 2015 June," *Astrophysical Journal*, vol. 824, p. L20, 2016.

- [91] T. Hovatta, M. Tornikoski, M. Lainela, H. Lehto and e. al., "Statistical analyses of long-term variability of AGN at high radio frequencies," *Astronomy and Astrophysics*, vol. 469, pp. 899-912, 2007.
- [92] M. Villata, C. Raiteri, H. Aller, M. Aller and e. al., "The WEBT campaigns on BL Lacertae. Time and cross-correlation analysis of optical and radio light curves 1968-2003," *Astronomy and Astrophysics*, vol. 424, pp. 497-507, 2004.
- [93] T. Poole, A. Breeveld, M. Page, W. Landsman and e. al., "Photometric calibration of the Swift ultraviolet/optical telescope," *Monthly Notices of the Royal Astronomical Society*, vol. 383, pp. 627-645, 2008.
- [94] P. Giommi, M. Perri, M. Capalbi, V. D'Elia and e. al., "X-ray spectra, light curves and SEDs of blazars frequently observed by Swift," *Monthly Notices of the Royal Astronomical Society*, vol. 507, pp. 5690-5702, 2021.
- [95] HI4PI Collaboration, "HI4PI: A full-sky H I survey based on EBHIS and GASS," *Astronomy and Astrophysics*, vol. 594, p. A116, 2016.
- [96] P. Kalberla, W. Burton, D. Harman, E. Arnal and e. al., "The Leiden/Argentine/Bonn (LAB) Survey of Galactic HI. Final data release of the combined LDS and IAR surveys with improved stray-radiation corrections," *Astronomy and Astrophysics*, vol. 440, pp. 775-782, 2005.
- [97] J. Dickey and F. Lockman, "H I in the galaxy," *Annual Review of Astronomy and Astrophysics*, vol. 28, pp. 215-261, 1990.
- [98] W. Atwood, A. Abdo, M. Ackermann, W. Althouse and e. al., "The Large Area Telescope on the Fermi Gamma-Ray Space Telescope Mission," *Astrophysical Journal*, vol. 697, pp. 1071-1102, 2009.
- [99] M. Ajello, R. Angioni, M. Axelsson, J. Ballet and e. al., "The Fourth Catalog of Active Galactic Nuclei Detected by the Fermi Large Area Telescope," *Astrophysical Journal*, vol. 892, p. 105, 2020.

- [100] S. Gasparyan, N. Sahakyan, V. Baghmanyan and D. Zargaryan, "On the Multiwavelength Emission from CTA 102," *Astrophysical Journal*, vol. 863, p. 114, 2018.
- [101] N. Sahakyan, V. Baghmanyan and D. Zargaryan, "Fermi-LAT observation of nonblazar AGNs," *Astronomy & Astrophysics*, vol. 614, p. A6, 2018.
- [102] D. Zargaryan, S. Gasparyan, V. Baghmanyan and N. Sahakyan, "Comparing 3C 120 jet emission at small and large scales," *Astronomy & Astrophysics*, vol. 608, p. A37, 2017.
- [103] V. Baghmanyan, S. Gasparyan and N. Sahakyan, "Rapid Gamma-Ray Variability of NGC 1275," *Astrophysical Journal*, vol. 848, p. 111, 2017.
- [104] R. Britto, E. Bottacini, B. Lott, S. Razzaque and S. Buson, "Fermi-LAT Observations of the 2014 May-July Outburst from 3C 454.3," *Astrophysical Journal*, vol. 830, p. 162, 2016.
- [105] B. Rani, T. Krichbaum, L. Fuhrmann, M. Botthor and e. al., "Radio to gamma-ray variability study of blazar S5 0716+714," *Astronomy and Astrophysics*, vol. 552, p. A11, 2013.
- [106] A. Shimmins and J. Bolton, "The Parkes 2700 MHz Survey (Sixth Part): Catalogue for the Declination zone  $-30^{\circ}$  to  $-35^{\circ}$ ," *Australian Journal of Physics Astrophysical Supplement*, vol. 32, p. 1, 1974.
- [107] D. Schwartz, R. Doxsey, R. Griffiths, M. Johnston and J. Schwarz, "X-ray emitting BL Lacertae objects located by the scanning modulation collimator experiment on HEAO 1.," *Astrophysical Journal*, vol. 229, pp. L53-L57, 1979.
- [108] W. Vestrand, J. Stacy and P. Sreekumar, "High-Energy Gamma Rays from the BL Lacertae Object PKS 2155-304," *Astrophysical Journal*, vol. 454, p. L93, 1995.
- [109] O. Chadwick, L. Derry, P. Vitousek, B. Huebert and L. Hedin, "Changing sources of nutrients during four million years of ecosystem development," *Nature*, vol. 397, pp. 491-497, 1999.

- [110] K. Nilsson, T. Pursimo, A. Sillanpaa, L. Takalo and E. Lindfors, "Detection of the host galaxy of S5 0716+714," *Astronomy and Astrophysics*, vol. 487, pp. L29-L32, 2008.
- [111] V. Bychkova, A. Vol'vach, N. Kardashe, M. Larionov and e. al., "Long-term monitoring of the blazars AO 0235+164 and S5 0716+714 in the optical and radio ranges," *Astronomy Reports*, vol. 59, pp. 851-864, 2015.
- [112] MAGIC Collaboration, "Multi-wavelength characterization of the blazar S5 0716+714 during an unprecedented outburst phase," *Astronomy and Astrophysics*, vol. 619, p. A45, 2018.
- [113] J. Kirk, F. Rieger and A. Mastichiadis, "Particle acceleration and synchrotron emission in blazar jets," *Astronomy and Astrophysics*, vol. 333, pp. 452-458, 1998.
- [114] N. Sahakyan and P. Giommi, "A 13-yr-long broad-band view of BL Lac," *Monthly Notices of the Royal Astronomical Society*, vol. 513, pp. 4645-4656, 2022.
- [115] B. Kapanadze, S. Vercellone, P. Romano, P. Hughes and e. al., "Strong X-ray flaring activity of the BL Lacertae source OJ 287 in 2016 October-2017 April," *Monthly Notices of the Royal Astronomical Society*, vol. 480, pp. 407-430, 2018.
- [116] S. Komossa, D. Grupe, M. Parker, J. Gomer and e. al., "X-ray spectral components of the blazar and binary black hole candidate OJ 287 (2005-2020)," *Monthly Notices of the Royal Astronomical Society*, vol. 504, pp. 5575-5587, 2021.
- [117] M. Schmidt, "Large Redshifts of Five Quasi-Stellar Sources.," *Astrophysical Journal*, vol. 141, p. 1295, 1965.
- [118] M. Zamaninasab, E. Clausen-Brown, T. Savolainen and A. Tchekhovskoy, "Dynamically important magnetic fields near accreting supermassive black holes," *Nature*, vol. 510, pp. 126-128, 2014.
- [119] P. Nolan, D. Bertsch, C. Fichtel, R. Hartman and e. al., "Observation of High-Energy Gamma Rays from the Quasi-stellar Object CTA 102," *Astrophysical Journal*, vol. 414, p. 82, 1993.

- [120] C. Casadio, J. Gómez, S. Jorstad, A. Marscher and e. al., "A Multi-wavelength Polarimetric Study of the Blazar CTA 102 during a Gamma-Ray Flare in 2012," *Astrophysical Journal*, vol. 813, p. 51, 2015.
- [121] T. Balonek, S. Zhang, K. Chapman, R. Stahlin and e. al., "Blazar CTA 102 Reaches Historic Optical Maximum During Current Extended Period of Activity," *The Astronomer's Telegram*, vol. 9732, p. 1, 2016.
- [122] K. Chapman, A. Sabyr, R.W.Stahlin, S. Zhang and T. Balonek, "A Spectacular, Unprecedented Optical Flare in the Blazar CTA 102," *The Astronomer's Telegram*, vol. 9756, p. 1, 2016.
- [123] V. Popov and R. Bachev, "Intra-night optical activity of the blazar CTA 102 during its maximum state," *The Astronomer's Telegram*, vol. 9776, p. 1, 2016.
- [124] S. Ciprini, "Fermi LAT observation of renewed and strong GeV gamma-ray activity from blazar CTA 102," *The Astronomer's Telegram*, vol. 9869, p. 1, 2016.
- [125] A. Bulgarelli, F. Verrecchia, C. Pittori, G. Minervini and e. al., "AGILE detects renewed gamma-ray emission from the FSRQ CTA 102," *The Astronomer's Telegram*, vol. 9788, p. 1, 2016.
- [126] J. Becerra, B. Carpenter and S. Cutini, "Fermi-LAT detection of strong flaring activity from the FSRQ CTA 102," *The Astronomer's Telegram*, vol. 8722, p. 1, 2016.
- [127] G. Minervini, G. Piano, P. Munar-Adrover, A. Bulgarelli and e. al., "AGILE detection of enhanced gamma-ray emission from the FSRQ CTA 102," *The Astronomer's Telegram*, vol. 9743, p. 1, 2016.
- [128] L. Carrasco, J. Miramon, E. Recillas, A. Porras and e. al., "A NIR Flare of the QSO PKS0306+102," *The Astronomer's Telegram*, vol. 8574, p. 1, 2016.
- [129] A. Shukla, K. Mannheim, S. Patel, V. Chitnis and e. al., "Short-timescale  $\gamma$ -Ray Variability in CTA 102," *Astrophysical Journal*, vol. 854, p. L26, 2018.
- [130] C. Raiteri, M. Villata, J. Acosta-Pulido, I. Agudo and e. al., "Blazar spectral variability as explained by a twisted inhomogeneous jet," *Nature*, vol. 552, pp. 374-377, 2017.

- [131] C. Casadio, A. Marscher, S. Jorstad, A. Dmitry and e. al., "The magnetic field structure in CTA 102 from high-resolution mm-VLBI observations during the flaring state in 2016-2017," *Astronomy & Astrophysics*, vol. 622, p. A158, 219.
- [132] M. Zacharias, M. Böttcher, F. Jankowsky, J. Lenain and e. al., "Cloud Ablation by a Relativistic Jet and the Extended Flare in CTA 102 in 2016 and 2017," *Astrophysical Journal*, vol. 851, p. 72, 2017.
- [133] M. Zacharias, M. Böttcher, F. Jankowsky, J. Lenain and e. al., "The Extended Flare in CTA 102 in 2016 and 2017 within a Hadronic Model through Cloud Ablation by the Relativistic Jet," *Astrophysical Journal*, vol. 871, p. 19, 2019.
- [134] R. Prince, G. Raman, J. Hahn, N. Gupta and P. Majumdar, "Fermi-Large Area Telescope Observations of the Brightest Gamma-Ray Flare Ever Detected from CTA 102," *Astrophysical Journal*, vol. 866, p. 16, 2018.
- [135] X. Li, P. Mohan, T. An, X. Hong and e. al., "Imaging and Variability Studies of CTA 102 during the 2016 January  $\gamma$ -ray Flare," *Astrophysical Journal*, vol. 854, p. 17, 2018.
- [136] N. Kaur and K. Bailyan, "CTA 102 in exceptionally high state during 2016-2017," *Astronomy and Astrophysics*, vol. 617, p. A59, 208.
- [137] F. D'Ammando, C. Raiteri, M. Villata, J. Pulido and e. al., "Investigating the multiwavelength behaviour of the flat spectrum radio quasar CTA 102 during 2013-2017," *Monthly Notices of the Royal Astronomical Society*, vol. 490, pp. 5300-5316, 2019.
- [138] M. Meyer, J. Scargle and D. Roger', "Characterizing the Gamma-Ray Variability of the Brightest Flat Spectrum Radio Quasars Observed with the Fermi LAT," *Astrophysical Journal*, vol. 877, p. 39, 2019.
- [139] V. Chavushyan, V. Patiño-Álvarez, R. Amaya-Almazán and L. Carrasco, "Flare-like Variability of the Mg II  $\lambda$ 2798 Å Emission Line and UV Fe II Band in the Blazar CTA 102," *Astrophysical Journal*, vol. 891, p. 68, 2020.

- [140] A. Acharyya, P. Chadwick and A. Brown, "Locating the gamma-ray emission region in the brightest Fermi-LAT flat-spectrum radio quasars," *Monthly Notices of the Royal Astronomical Society*, vol. 500, pp. 5297-5321, 2021.
- [141] A. Roy, S. Patel, A. Sarkar, A. Chatterjee and V. Chitnis, "Multiwavelength study of the quiescent states of six brightest flat-spectrum radio quasars detected by Fermi-LAT," *Monthly Notices of the Royal Astronomical Society*, vol. 504, pp. 1103-1114, 2021.
- [142] S. H. Kim, S. S. Lee, J. W. Lee, J. A. Hodges and e. al., "Magnetic field strengths of the synchrotron self-absorption region in the jet of CTA 102 during radio flares," *Monthly Notices of the Royal Astronomical Society*, vol. 510, pp. 815-833, 2022.
- [143] X. Geng, N. Ding, G. Cao, Y. Liu and e. al., "Exploring  $\gamma$ -Ray Flares in the Long-term Light Curves of CTA 102 at GeV Energies," *Astrophysical Journal Supplement Series*, vol. 260, p. 48, 2022.
- [144] N. Sahakyan, "Modelling the broad-band emission of 3C 454.3," *Monthly Notices of the Royal Astronomical Society*, vol. 504, pp. 5074-5086, 2021.
- [145] S. Abdollahi, F. Acero, L. Baldini, J. Ballet and e. al., "Incremental Fermi Large Area Telescope Fourth Source Catalog," *Astrophysical Journal Supplement Series*, vol. 260, p. 53, 2022.
- [146] B. Lott, L. Escande, S. Larsson and J. Ballet, "An adaptive-binning method for generating constant-uncertainty/constant-significance light curves with Fermi-LAT data," *Astronomy and Astrophysics*, vol. 544, p. A6, 2012.
- [147] N. Sahakyan and S. Gasparian, "High energy gamma-ray emission from PKS 1441+25," *Monthly Notices of the Royal Astronomical Society*, vol. 470, pp. 2861-2869, 2017.
- [148] J. Scargle, J. Norris, B. Jackson and J. Chiang, "Studies in Astronomical Time Series Analysis. VI. Bayesian Block Representations," *Astrophysical Journal*, vol. 764, p. 167, 2013.

- [149] F. Harrison, W. Craig, F. Christensen, C. Hailey and e. al., "The Nuclear Spectroscopic Telescope Array (NuSTAR) High-energy X-Ray Mission," *Astrophysical Journal*, vol. 770, p. 103, 2013.
- [150] R. Middei, P. Giommi, M. Perri, S. Turriziani and e. al., "The first hard X-ray spectral catalogue of Blazars observed by NuSTAR," *Monthly Notices of the Royal Astronomical Society*, vol. 514, pp. 3179-3190, 2022.
- [151] P. Smith, E. Montiel, S. Rightley, J. Turner and e. al., "Coordinated Fermi/Optical Monitoring of Blazars and the Great 2009 September Gamma-ray Flare of 3C 454.3," *arXiv e-prints*, p. arXiv:0912.3621, 2009.
- [152] C. Kochanek, B. Shappee, K. Stanek, T.-S. Holm and e. al., "The All-Sky Automated Survey for Supernovae (ASAS-SN) Light Curve Server v1.0," *Publications of the Astronomical Society of the Pacific*, vol. 129, p. 104502, 2017.
- [153] A. Drake, S. Djogovski, A. Mahabal, E. Beshore and e. al., "First Results from the Catalina Real-Time Transient Survey," *Astrophysical Journal*, vol. 696, pp. 870-884, 2009.
- [154] C. Dermer and R. Schlickeiser, "Model for the High-Energy Emission from Blazars," *Astrophysical Journal*, vol. 416, p. 458, 1993.
- [155] C. Dermer, R. Schlickeiser and A. Mastichiadis, "High-energy gamma radiation from extragalactic radio sources.," *Astronomy and Astrophysics*, vol. 256, pp. L27-L30, 1992.
- [156] E. Pian, R. Falomo and A. Treves, "Hubble Space Telescope ultraviolet spectroscopy of blazars: emission-line properties and black hole masses," *Monthly Notices of the Royal Astronomical Society*, vol. 361, pp. 919-926, 2005.
- [157] A. Tramacere, P. Giommi, M. Perri, F. Verrecchia and G. Tosti, "Swift observations of the very intense flaring activity of Mrk 421 during 2006. I. Phenomenological picture of electron acceleration and predictions for MeV/GeV emission," *Astronomy & Astrophysics*, vol. 501, pp. 879-898, 2009.

- [158] A. Tramacere, E. Massaro and A. Taylor, "Swift observations of the very intense flaring activity of Mrk 421 during 2006. I. Phenomenological picture of electron acceleration and predictions for MeV/GeV emission," *Astrophysical Journal*, vol. 739, p. 66, 2011.
- [159] A. Tramacere, "JetSeT: Numerical modeling and SED fitting tool for relativistic jets," *Astrophysics Source Code Library*, p. ascl:2009.001, 2020.
- [160] D. Giannios, D. Uzdensky and M. Begelman, "Fast TeV variability in blazars: jets in a jet," *Monthly Notices of the Royal Astronomical Society*, vol. 395, pp. L29-L33, 2009.
- [161] D. Giannios, D. Uzdensky and M. Begelman, "Fast TeV variability from misaligned minijets in the jet of M87," *Monthly Notices of the Royal Astronomical Society*, vol. 402, pp. 1649-1656, 2010.
- [162] A. Spitkovsky, "Particle Acceleration in Relativistic Collisionless Shocks: Fermi Process at Last?," *Astrophysical Journal*, vol. 682, p. L5, 2008.
- [163] E. Summerlin and M. Baring, "Diffusive Acceleration of Particles at Oblique, Relativistic, Magnetohydrodynamic Shocks," *Astrophysical Journal*, vol. 745, p. 63, 2012.
- [164] M. Baring, M. Böttcher and E. Summerlin, "Probing acceleration and turbulence at relativistic shocks in blazar jets," *Monthly Notices of the Royal Astronomical Society*, vol. 464, pp. 4875-4894, 2017.
- [165] S. Zenitani and M. Hoshino, "The Generation of Nonthermal Particles in the Relativistic Magnetic Reconnection of Pair Plasmas," *Astrophysical Journal*, vol. 562, pp. L63-L66, 2001.
- [166] L. Sironi and A. Spitkovsky, "Relativistic Reconnection: An Efficient Source of Non-thermal Particles," *Astrophysical Journal*, vol. 783, p. L21, 2014.
- [167] F. Guo, Y.-H. Liu, W. Daughton and H. Li, "Particle Acceleration and Plasma Dynamics during Magnetic Reconnection in the Magnetically Dominated Regime," *Astrophysical Journal*, vol. 806, p. 167, 2015.
- [168] N. Kardashev, "Nonstationarity of Spectra of Young Sources of Nonthermal Radio Emission," *Soviet Astronomy*, vol. 6, p. 317, 1962.

- [169] N. Sahakyan, D. Zargaryan and V. Baghmanyany, "On the gamma-ray emission from 3C 120," *Astronomy and Astrophysics*, vol. 574, p. A88, 2015.
- [170] V. Baghmanyany and N. Sahakyan, "X-ray and  $\gamma$ -ray emissions from NLSy1 galaxies," *International Journal of Modern Physics D*, vol. 27, 2018.
- [171] M. Cappi, M. Matsuoka, A. Comastri, W. Brinkmann and e. al., "ASCA and ROSAT X-Ray Spectra of High-Redshift Radio-loud Quasars," *Astrophysical Journal*, vol. 478, pp. 492-510, 1997.
- [172] F. Fiore, M. Elvis, P. Giommi and P. Padovani, "X-Ray Spectral Survey of WGACAT Quasars. I. Spectral Evolution and Low-Energy Cutoffs," *Astrophysical Journal*, vol. 492, pp. 79-90, 198.
- [173] J. Reeves, M. Turner, P. Bennie, K. Pounds and e. al., "The first XMM-Newton spectrum of a high redshift quasar - PKS 0537-28," *Astronomy and Astrophysics*, vol. 365, pp. L116-L121, 2001.
- [174] [Online] <https://fermi.gsfc.nasa.gov/science/eteu/agn/>.
- [175] [Online] <https://journals.aps.org/prd/abstract/10.1103/PhysRevD.80.122004>.